Novel designs for micro-scale broadband NMR detectors

Zur Erlangung des akademischen Grades eines

DOKTORS DER INGENIEURWISSENSCHAFTEN (Dr.-Ing.)

von der KIT-Fakultät für Maschinenbau des
Karlsruher Instituts für Technologie (KIT)
angenommene

DISSERTATION

von

M. Sc. Jianyi Liang

Tag der mündlichen Prüfung:	07.07.2026
Hauptreferent:	Prof. Dr. Jan G. Korvink
Korreferent:	Prof. Dr. Ahmet Cagri Ulusoy

KIT – Die Forschungsuniversität in der Helmholtz-Gemeinschaft www.kit.edu

Karlsruher Institut für Technologie
Institut für Mikrostrukturtechnik
Hermann-von-Helmholtz Platz 1
76344 Eggenstein-Leopoldshafen

Selbstständigkeitserklärung

Ich versichere wahrheitsgemäß, die Arbeit selbstständig verfasst, alle benutzten Hilfsmittel vollständig und genau angegeben und alles kenntlich gemacht zu haben, was aus Arbeiten anderer unverändert oder mit Abänderungen entnommen wurde sowie die Satzung des KIT zur Sicherung guter wissenschaftlicher Praxis in der jeweils gültigen Fassung beachtet zu haben.

Eggenstein-Leopoldshafen, 07.07.2026 Jianyi Liang

Abstract

Nuclear magnetic resonance (NMR) is a non-invasive and non-destructive analytical technique that provides atomic-level insights into molecular structures and dynamics through radio-frequency (RF) excitation. However, NMR inherently suffers from low sensitivity, often requiring large sample volumes or expensive high-field magnets to obtain measurable signals. Micro coils have therefore attracted considerable attention, as they significantly improve mass sensitivity and enable the analysis of volume-limited samples. In general, mass sensitivity is inversely related to the coil dimension. At the same time, the available sample quantity is often limited, for example, biological tissues, either because of high preparation costs or limited availability. In such situations, micro coils offer a high filling factor, and consequently a higher signal-to-noise ratio (SNR). Despite these advances, there is an increasing demand for versatile detectors capable of broadband, multinuclear operation without complex and time-consuming hardware adjustments. This thesis introduces and investigates two novel approaches to broadband micro-scale NMR detection.

The first part of the work reviews two common broadband micro NMR coil geometries, namely the stripline and the Lenz lens coil, and proposes a combined structure termed the stripline Lenz lens (S3L). This design integrates the main advantages of both geometries: the high local RF field strength of the stripline and the magnetic flux concentration provided by the Lenz lens. As a non-resonant, inductively coupled interposer, the device produces a relatively uniform RF field and achieves an 11-fold signal enhancement when coupled to a 10 mm commercial coil. Miniaturization, however, also introduces the challenges such as susceptibility mismatches between different materials and increased sensitivity to dimensional deviations that can degrade the magnetic field. To address these issues, extensive simulation studies were performed to optimize key NMR performance metrics. Building on previous work on glass-based micro NMR coils, a complete microfabrication process was developed for a sandwiched NMR chip incorporating a microfluidic channel. Nevertheless, this passive interposer still requires a resonant excitation coil, and conventional substrates such as glass remain mechanically fragile and difficult to process for complex coil structures and integrated microfluidics.

The second approach introduces a less explored technology in NMR applications, low-temperature cofired ceramic (LTCC), to address these limitations. In this work, a planar spiral geometry, a well-known candidate for broadband micro NMR detection, was implemented on an LTCC substrate. A robust dual-channel micro coil was developed using a split-spiral configuration, optimizing sensitivity for both high-γ nuclei (^1H) and low-γ nuclei (e.g., ^{13}C) in a completely untuned and unmatched configuration. Similar to the first design, this detector supports broadband operation over a frequency range of approximately 100 MHz to 500 MHz.

In summary, this thesis presents a comprehensive framework for the design and fabrication of cost-effective, high-performance broadband micro NMR detectors. By moving away from conventional resonant hardware toward passive, high-gain interposers and mechanically robust ceramic substrates, this work simplifies the NMR experimental workflow and provides a versatile tool for multinuclear studies.

Zusammenfassung

Die Kernspinresonanz (Nuclear Magnetic Resonance, NMR) ist eine nichtinvasive und zerstörungsfreie analytische Methode, die durch Anregung mit Radiofrequenz-(RF-)Feldern Einblicke in Molekülstrukturen und -dynamiken auf atomarer Ebene ermöglicht. Allerdings leidet die NMR grundsätzlich unter einer geringen Empfindlichkeit, sodass häufig große Probenvolumina oder teure Hochfeldmagnete erforderlich sind, um messbare Signale zu erhalten. Mikrospulen haben daher große Aufmerksamkeit erlangt, da sie die Massensensitivität deutlich verbessern und die Analyse von volumenbegrenzten Proben ermöglichen. Im Allgemeinen ist die Massensensitivität umgekehrt proportional zur Spulendimension. Gleichzeitig ist die verfügbare Probenmenge häufig begrenzt, beispielsweise bei biologischem Gewebe, entweder aufgrund hoher Präparationskosten oder eingeschränkter Verfügbarkeit. In solchen Fällen bieten Mikrospulen einen hohen Füllfaktor und damit ein höheres Signal-zu-Rausch-Verhältnis (Signal-to-Noise Ratio, SNR). Trotz dieser Fortschritte besteht ein wachsender Bedarf an vielseitigen Detektoren, die einen breitbandigen, multinuklearen Betrieb ohne komplexe und zeitaufwändige Hardwareanpassungen ermöglichen. Diese Dissertation stellt zwei neuartige Ansätze zur breitbandigen mikro-skaligen NMR-Detektion vor und untersucht diese.

Im ersten Teil der Arbeit werden zwei verbreitete Geometrien breitbandiger Mikro-NMR-Spulen betrachtet, nämlich die Stripline und die Lenzlinsenspule, und eine kombinierte Struktur vorgeschlagen, die als Stripline-Lenzlinse (S3L) bezeichnet wird. Dieses Design vereint die wesentlichen Vorteile beider Geometrien: die hohe lokale RF-Feldstärke der Stripline und die magnetische Flusskonzentration der Lenzlinse. Als nichtresonanter, induktiv gekoppelter Interposer erzeugt die Struktur ein relativ homogenes RF-Feld und erreicht eine elffache Signalverstärkung bei Kopplung mit einer kommerziellen 10 mm-Spule. Die Miniaturisierung bringt jedoch auch Herausforderungen mit sich, etwa Suszeptibilitätsunterschiede zwischen verschiedenen Materialien sowie eine erhöhte Empfindlichkeit gegenüber Maßabweichungen, die das Magnetfeld verschlechtern können. Zur Bewältigung dieser Probleme wurden umfangreiche Simulationsstudien durchgeführt, um zentrale NMR-Leistungsparameter zu optimieren. Aufbauend auf früheren Arbeiten zu glasbasierten Mikro-NMR-Spulen wurde ein vollständiger Mikrostrukturierungsprozess für einen sandwichartigen NMR-Chip mit integriertem Mikrofluidikkanal entwickelt. Dennoch erfordert dieser passive Interposer weiterhin eine resonante Anregungsspule, und konventionelle Substrate wie Glas bleiben mechanisch fragil und schwierig zu verarbeiten, insbesondere für komplexe Spulenstrukturen und integrierte Mikrofluidik.

Der zweite Ansatz führt eine bislang wenig genutzte Technologie in NMR-Anwendungen ein, Low-Temperature Cofired Ceramic (LTCC), um diese Einschränkungen zu überwinden. In dieser Arbeit wurde eine planare Spiralgeometrie, ein bekannter Kandidat für breitbandige Mikro-NMR-

Detektion, auf einem LTCC-Substrat realisiert. Es wurde eine robuste zweikanalige Mikrospule mit einer Split-Spiral-Konfiguration entwickelt, die die Empfindlichkeit sowohl für Kerne mit hohem gyromagnetischen Verhältnis (hohes γ, z. B. ^1H) als auch für Kerne mit niedrigem γ (z. B. ^{13}C) in einer vollständig ungetunten und nicht angepassten Konfiguration optimiert. Ähnlich wie beim ersten Design unterstützt dieser Detektor einen breitbandigen Betrieb im Frequenzbereich von etwa 100 MHz bis 500 MHz.

Zusammenfassend präsentiert diese Dissertation ein umfassendes Konzept für das Design und die Herstellung kosteneffizienter, leistungsfähiger breitbandiger Mikro-NMR-Detektoren. Durch die Abkehr von konventioneller resonanter Hardware hin zu passiven Interposern mit hoher Verstärkung sowie mechanisch robusten keramischen Substraten vereinfacht diese Arbeit den experimentellen NMR-Arbeitsablauf und stellt eine vielseitige Plattform für multinukleare Untersuchungen bereit.

Acknowledgement

I wish to extend my gratitude to all those involved directly and indirectly in the realization of this dissertation.

I would like to express my deepest appreciation to Prof. Jan G. Korvink for giving me the opportunity to conduct research on such a fascinating topic within this excellent group. Over the past few years, I have gained a wealth of knowledge under his guidance. Beyond the technical skills required to finish this PhD project, I am grateful for the life wisdom he shared, which I will carry with me long after I leave.

My sincere thanks go to Dr. Vlad Badilita, my group leader. Vlad is the person with whom I shared the most ups and downs of this research journey. Even after working together all this time, there is always something new and valuable to learn from him.

I want to thank Dr. Hossein Davoodi for his support, reaching back to my Master's studies and through the beginning of my PhD. His help through many working days was invaluable. My thanks also go to Dr. Sagar Wadhwa and Khai for their collaboration and the fruitful discussions that pushed my work forward. I would like to acknowledge Dr. Neil MacKinnon and Dr. Mazin Juda, who generously shared their advice regarding both my project and various lab tasks.

I am grateful to my group members, Albina, Ajeya, Dr. Mustafa, and Shishir, for their valuable ideas and input during our weekly and monthly meetings. To my office mates, Mengjia, Dr. Jing Yang and Dr. Yentse Cheung: thank you for the extensive discussions, and scientific insights. My work would not have been possible without the technical assistance and support of many colleagues at IMT.

On a personal note, I want to thank my family for their endless love and patience. A special thank you goes to Keren, who has been a wonderful companion through the hard and the sweet years in Germany.

Finally, I will truly miss my time at Campus North. The beauty of the changing seasons here are unforgettable.

Nomenclature

Abbreviations

Abbreviation	Definition
1D	One-dimensional
2D	Two-dimensional
3D	Three-dimensional
AC	Alternating Current
ADC	Analog- to-digital converter
ADS	Advanced Design System
CMOS	Complementary Metal-Oxide Semiconductor
DC	Direct Current
FEM	Finite Element Method
FID	Free Induction Decay
FOV	Field Of View
FOV	Field of View
FWHM	Full Width at Half Magnitude
LNA	Low Noise Amplifier
LOD	Limit Of Detection
LTCC	Low Temperature Co-fired Ceramic
MACS	Magic Angle Coil Spinning
MAS	Magic Angle Spinning
MEMS	Micro Electro-Mechanical System
MRI	Magnetic Resonance Imaging
nLOD	Normalised Limit Of Detection
NMR	Nuclear Magnetic Resonance
PA	Power Amplifier
PCB	Printed Circuit Board
PMMA	Polymethylmethacrylate
ppb	Parts per billion
ppm	Parts per million
PVD	Physical Vapour Deposition
Q	Quality factor
RF	Radio Frequency
RX	Receiver network

S3L	Stripline Lenz Lens, a nonresonant electric add-on for NMR signal detection
SNR	Signal-to-Noise Ratio
TX	Transmitter network
VSI	Vertical Scanning Interferometry

Symbols

Symbol	Definition
δ	Skin depth
ε_r	Relative permittivity
γ	Gyromagnetic ratio
λ	Wavelength
$\vec{\mu}$	Magnetic moment
μ_r	Relative permeability
$\nu_{1/2}$	Full Width at Half Magnitude
ω_0	Larmor Frequency
ω	Frequency
ρ	Specific electrical resistance
σ	Chemical shift
$\tau_{\pi/2}$	90° pulse length
ξ	Induced signal voltage
B_0	Static magnetic field
B_1	RF magnetic field
D_1	Delay time NMR measurement
E	Energy level
I	Nuclear spin
m	Magnetic quantum number
M	Magnetization in a sample
Q	Quality factor
S_{ij}	S-parameter between ports i and j
$\vec{S}$	Spin angular momentum
T	Temperature
T_1	Longitudinal (spin-lattice) relaxation time constant
T_2	Spin-spin relaxation time constant
Electronics	
I, i	Current
V	Voltage
Z	Impedance
R	Resistor or its resistance

C	Capacitor or its capacitance
L	Inductor or its inductance
M	Mutual inductance
N_c	Thermal noise of the coil
W	Electrical energy

Constants

Symbol	**Definition**
ε_0	Vacuum permittivity
μ_0	Vacuum permeability
h	Planck constant
$\hbar$	Reduced Planck constant
k_B	Boltzmann constant

Contents

Chapter 1

Introduction

1.1 Motivation

This research centers on the concept of micro broadband NMR detectors.

Nuclear magnetic resonance (NMR), as one of the most powerful characterization methods, acquires detailed material information with the specific nuclei spin. The interaction with the nucleus (or isotopes) only happens when the 'probing' radio-frequency (RF) signal has a same frequency as the self-resonance frequency of the nucleus of interest. With that being said, conventional NMR is a narrowband detection solution. Considering the complexity of a component within a natural sample rather than an in-lab prepared sample, a full information read-out requires measuring different isotopes for analyzing molecular structures, studying chemical interactions, and identifying unknown compounds, e.g., in a protein-ligand complex or a drop of fresh apple juice. A typical approach to address this issue is multi-resonance probes, which leads to a high time cost with iterative measurements and a high expense of spending ca. 10 k euro for each additional commercial coil for NMR users. Broadband, as a general concept across different research contexts, refers to the utilization of signals over a wide frequency range or across multiple simultaneous frequencies. In general, broadband detection is well suited for extracting as much relevant information as possible from a given subject within a limited time interval. Meanwhile, broadband detection is specifically required for studying dynamic processes where multiple nuclei must be monitored near-simultaneously. Under such circumstances, scientists have applied broadband detection to NMR, prompting the invention of various broadband NMR detectors for high-resolution multinuclear NMR signals. While it is often argued that non-tuned broadband systems suffer from lower SNR compared to their tuned counterparts, this work addresses this trade-off through advanced micro-engineering. As the first objective of this work, broadband NMR detectors are designed in order to ease the measurement operation while offering good sensitivity and spectral resolution.

In parallel, micro-NMR has become an important research topic, particularly in situations where the available sample volume is limited, either due to restricted access to the material (e.g., human tissues) or the high cost of non-reusable consumable samples. In such contexts,

broadband detectors are indispensable to allow researchers to switch between nuclei instantaneously. Furthermore, this flexibility is crucial for specialized applications, such as in-situ measurements, where the integration of bulky electronics is physically impossible, due to extreme spatial constraints and the need for rapid data acquisition during transient reaction events. Potential broadband detector solutions should therefore evaluate the currently available micro electro-mechanical system (MEMS) technologies and select materials and fabrication methods that primarily optimize NMR performance while also considering cost efficiency.

With this overall objective in mind, this research contributes to evaluating existing NMR coil geometries and developing novel broadband micro coils that address key challenges in NMR studies, including intrinsically low sensitivity, long measurement times, and complex hardware handling in multinuclear detection. The devices introduced in this work are expected to support a wide range of NMR applications in multidisciplinary fields, such as the analysis of biological samples and energy storage materials.

1.2 Thesis outline

This thesis focuses on the development of genuine broadband NMR detectors. While the first (current) chapter introduces the thesis, **Chapter** 2 presents the general concepts of NMR with a more detailed discussion on the coil geometries and miniaturization techniques.

The following chapters, **Chapter** 3 and **Chapter** 4, present the project work on different NMR detectors. Each chapter starts with a brief introduction a a review of the relevant fundamentals, followed by theoretical and simulation studies as well as experimental characterization of the devices. **Chapter** 3 reports on the first work of this thesis, the stripline Lenz lens, which is a broadband add-on device compatible with common saddle coils and designed to enhance the measurement sensitivity for samples at the sub-microliter volume scale. **Chapter** 4 studies a double-port spiral detector fabricated using low-temperature cofired ceramics (LTCC), which enables multinuclear detection in both 1D and 2D NMR experiments.

The thesis concludes with **Chapter** 5, which discusses the main achievements of this work and provides an outlook on potential future developments.

1.3 Main Results

The research conducted within this PhD project are concluded in two scientific publications with a contribution as first author or shared first authorship.

- **Broadband stripline Lenz lens achieves** 11 × **NMR signal enhancement** [J1]
  Published in Scientific Reports, 2024.
  Authorship: Lead author *Content*: This paper presents a new type of stripline detector combined with Lenz lens design as an add-on device for standard NMR saddle coils. The device holds micro-samples and is able to flip the RF field by 90° in the sample region. A series of multinuclear NMR measurements shows an SNR enhancement of 11 times

and its applicability to 2D NMR studies. *Contributions*: Designed, constructed, and optimized the experimental configuration. Performed system characterization, executed parallel NMR experiments, and conducted data analysis. Led the manuscript writing and figure preparation.

- **Split spiral broadband double channel NMR detector facilitated by LTCC technology** [J2]
  Published in Scientific Reports, 2025.
  Authorship: Lead author
  Content: This paper introduces a variant of planar spiral coil, which has two detection channels based on a split-spiral geometry. The study characterizes the typical spiral coil and optimizes the split-spiral design using computational simulation tools. The device was fabricated in LTCC, a promising technology for NMR hardware. Its performance was experimentally validated at four frequencies with 1D and 2D NMR spectroscopy. *Contributions*: Designed, constructed, and fine-tuned the experimental configuration. Carried out system characterization, executed parallel NMR experiments, and analyzed the resulting data. Led the manuscript writing and figure preparation.

Chapter 2

Background Information

2.1 Overview

Nuclear magnetic resonance (NMR) has proven to be a powerful and versatile technique since Isidor Isaac Rabi first discovered the magnetic moment of the deuteron in 1938, an achievement for which he was awarded the Nobel Prize in 1944 [1]. In the late 1940s, Felix Bloch and Edward M. Purcell demonstrated NMR experiments using simple electromagnets and radio-frequency coils [2, 3], paving the way for rapid theoretical developments and experimental applications. In 1966, Richard R. Ernst developed Fourier transform NMR, enabling the simultaneous excitation and acquisition of signals over a broad frequency range. This led to the establishment of multinuclear NMR and two-dimensional (2D) NMR spectroscopy, which are essential for analyzing complex molecules such as proteins. By the 2000s, solid-state NMR had seen significant advances, particularly through magic angle spinning (MAS) techniques that average out anisotropic interactions.

In parallel with the theoretical development of NMR, detection hardware has evolved continuously since the 1950s to improve sensitivity and spectral resolution. The development of stronger magnet systems has enabled significantly higher magnetic field strengths, which remain a primary "brute-force" method for enhancing both sensitivity and resolution. Meanwhile, advances in electronics have improved frequency stability, improved noise reduction, and enabled more sophisticated signal processing, e.g., through the use of lock-in amplifiers. Since 2000, MAS probes have enabled high-resolution measurements of solid materials, and rotor design has become a key focus in MAS NMR to achieve higher spinning speeds. In addition, advances in system miniaturization have also played an important role in improving NMR performance, expanding application areas, and reducing hardware costs.

In the following chapter, the necessary background for this research is provided, moving from basic theory to advanced detector design. The discussion begins with the fundamental NMR principles and the figures of merit used to evaluate performance, such as field homogeneity and sensitivity. Then, an introduction to NMR hardware is presented, focusing on the design of probes and coils. The chapter then moves to a detailed analysis of probe miniaturization, which

explores how NMR systems and coils can be scaled down and optimized for both liquid and solid-state applications. This section also introduces the micro-scale fabrication techniques required to build such micro-probes. Finally, the chapter discusses broadband NMR, comparing traditional multi-resonance circuits with the non-tuned approach that forms the focus of this thesis.

2.2 NMR principles

As the basic particle of the chemical elements, an atom consists of a nucleus of protons and generally neutrons, surrounded by an electromagnetically bound electron cloud. Different isotopes present distinctive properties, e.g., charge, spin angular momentum ($\vec{S}$) and magnetic moment ($\vec{\mu}$). The relationship between the magnetic moment ($\vec{\mu}$) and spin angular momentum ($\vec{S}$) of the nuclei is expressed as:

$$\vec{\mu} = \gamma \vec{S}, \tag{2.1}$$

in which γ is the gyromagnetic ratio, an intrinsic property of the isotope, determining the strength of the magnetic moment by a given angular momentum. In nuclear physics, γ can be affected by the nucleon spins, the orbital angular momenta and the couplings, and is thus difficult to calculate. However, the gyromagnetic ratios have been measured with high precision for most nuclei. For the sub-atomic particles, i.e., electron, proton, and neutron, the spin quantum number I is $1/2$. The nuclear spin I is a fixed property of the nucleus based on the combination of protons and neutrons. This value can be either an integer or a half-integer, representing the total angular momentum of the nucleus in its ground state. Consequently, each nuclear spin state has $2 \times I + 1$ substates. The relationship between the magnitude of $\vec{S}$ and I of a certain nucleus can be quantized as

$$\|\vec{S}\| = \hbar\sqrt{I(I+1)}, \tag{2.2}$$

where $\hbar$ is the reduced Planck's constant.

When no external magnetic field is applied, the spin angular momentum is randomly oriented, and the overall magnetization of the sample is canceled out to be zero as illustrated in Fig. 2.1 (a) [4]. But when a static field B_0 is present in the sample space, which is defined to be along the Z-axis of the space by convention for the benefit of researchers, the spin states split into discrete energy levels. This phenomenon is known as nuclear Zeeman effect. The energy difference between two consecutive substates ΔE and energy E are calculated as:

$$\begin{aligned} \Delta E &= -\vec{\mu}\vec{B_0} = \gamma\hbar B_0, \\ E &= -\gamma\hbar m B_0. \end{aligned} \tag{2.3}$$

m is the magnetic quantum number ($m = -I, -(I-1), ..., (I-1), I$). This interaction of the nuclear magnetic moment with the B_0 field gives rise to the so-called Larmor precession of the relatively isolated magnetic dipoles (spin vectors) around the Z-axis, as shown in Fig. 2.1 (b). The angular precession frequency, i.e., Larmor frequency, is dependent on the static field strength and the gyromagnetic ratio of the specific nucleus:

$$\omega_0 = \gamma B_0, while \quad \vec{\tau} = \vec{\mu} \times \vec{B_0}, \tag{2.4}$$

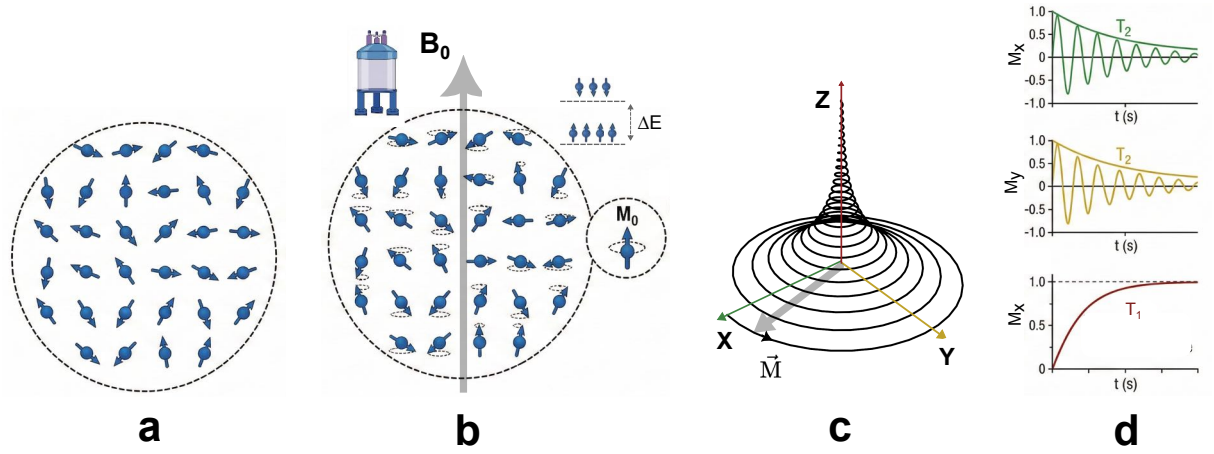

Figure 2.1: *(a) Illustration of random distribution of spin vectors in a sample when no external magnetic field is applied. (b) In the presence of a static magnetic field B_0, the spins precess about the field direction and partially align with it. Two energy substates are formed, resulting in a net magnetization M_0 in the sample. (c) After a 90° flipping induced by an RF pulse, the magnetization precesses around the B_0 field direction (Z-axis) and returns to its equilibrium state. (d) The change of magnetization components during the process shown in (c) characterized by the relaxation time constants T_1 and T_2.*

in which $\vec{\tau}$ is the torque created by the external field and $\times$ is the cross product. It should be noted that the Larmor frequency is independent of the spatial orientation of the spins with respect to the direction of the applied magnetic field, making it a key parameter in NMR. And it also plays an vital role in sample excitation by RF pulses, as discussed later in this section. Only nuclei with nonzero spin can interact with magnetic fields; for instance, ^{12}C and ^{16}O are inactive nuclei for NMR measurements. The spin substates are either parallel to the $\vec{B_0}$ (the low energy state) or anti-parallel to the field (the high energy state), as shown in Fig. 2.1 (b). The populations of these two substates are very similar, with a ratio of $1 - \frac{\Delta E}{k_B T}$ according to the Boltzmann distribution, where ΔE is about four orders of magnitude smaller than the thermal energy $k_B T$. Still, the precessing nuclei contribute to a net magnetization of the sample (M):

$$\begin{aligned} M_0 &= \frac{N\gamma^2\hbar^2 B_0 I(I+1)}{3k_B T}, \\ M_z(t) &= M_0(1 - e^{-\frac{1}{T_1}}), \end{aligned} \tag{2.5}$$

where k_B is the Boltzmann constant, T is the temperature of the sample and N is the number of nulcei contributing to the magnetization. M_0 is the macroscopic magnetization of the sample at the thermal equilibrium and M_z is the changing net magnetization over time when B_0 is applied at $t = 0$. T_1 is denoted as the longitudinal (spin-lattice) relaxation time constant.

In order to detect the weak net magnetization of the sample, it is first flipped from the Z-direction to the transverse plane (XY-plane according to the previously defined coordinate system). This is achieved by applying an oscillating magnetic field, denoted as B_1, in the transverse plane with a frequency equal to the Larmor frequency of the target nuclei. When an excitation pulse (RF pulse) $\vec{B_1} = B_x\vec{x} + B_y\vec{y}\,(+B_z\vec{z})$ is applied, the evolution of the magnetization

can be described by the Bloch equations [2]:

$$\frac{d}{dt}\begin{pmatrix} M_x \\ M_y \\ M_z \end{pmatrix} = \begin{pmatrix} -\frac{1}{T_2} & \gamma B_z & -\gamma B_y \\ -\gamma B_z & -\frac{1}{T_2} & \gamma B_x \\ \gamma B_y & -\gamma B_x & -\frac{1}{T_1} \end{pmatrix} \begin{pmatrix} M_x \\ M_y \\ M_z \end{pmatrix} + \begin{pmatrix} 0 \\ 0 \\ \frac{M_0}{T_1} \end{pmatrix}, \tag{2.6}$$

where T_1 and T_2 are respectively the spin-lattice and spin-spin relaxation time constants. A complete process is illustrated in Fig. 2.1 (c) and (d).

The tilt angle of the spins from the Z-axis depends on the irradiation energy delivered by the RF field B_1. A pulse that rotates the spins exactly to the XY-plane is defined as a 90° pulse, as displayed in Fig. 2.1 (c). It is an important concept in both detector design and experiment operation, and the 90° pulse length is given by:

$$\tau_{\pi/2} = \frac{\pi/2}{\gamma B_1}, \tag{2.7}$$

which is ideally much shorter than the relaxation times. The energy absorbed by the spins starts to dissipate once the RF pulse is removed, and the nuclei relax back to their thermal equilibrium state while continuing to precess. The electromagnetic radiation emitted during this relaxation process can be detected by an NMR coil based on Faraday's law of induction. This induced signal represents the NMR signal prior to further transmission and processing. The sample excitation and signal detection can be performed either by a single coil or two separate coils. According to the principle of reciprocity, the sensitivity of an NMR detector at any point in space is directly proportional to the magnetic field B_1 produced at that point by a unit current flowing through the coil. In an ideal, lossless system, this implies that the excitation efficiency and the reception sensitivity at this point are identical.

The induced signal collected by the coil can be calculated as:

$$\xi = \int \frac{\partial(\vec{B_{1u}} \cdot \vec{M})}{\partial t}\, dV_\mathrm{s}, \tag{2.8}$$

where $\vec{B_{1u}}$ is the RF field strength generated by a unit current in the coil and V_s is the sample volume. The equation shows that the signal magnitude is mainly affected by the static field strength, RF field strength and sample volume. The first two factors are key objects of sensitivity enhancement, while the limited sample volume is often a practical constraint in NMR studies. The sinusoidal signal is observed in the time domain as the free induction decay (FID). In certain cases where only a limited number of frequency components are present, the FID can be analyzed directly to determine physical properties quantitatively (time-domain NMR), for example, the hydrogen content in aviation fuel [5]. In most cases, however, the FID data is digitized and Fourier transformed into a the frequency domain, producing the NMR spectrum. It provides detailed information about a complex of chemical environment, molecular structure, and dynamics of the sample.

An NMR spectrum typically consists of multiple peaks distributed along the frequency axis. Assuming a stable B_0 field and a homogeneous B_1 field by a sufficiently sensitive coil, the signal peak of a given nucleus is influenced by several fine interactions with the surrounding molecular

structure and environment. The structural information of the sample can be inversely identified from the the acquired spectra.

Chemical shift: The molecular structure and the local electron density surrounding the observed spin give rise to a slight distortion of the local static field, leading to a shift of the signal frequency from the reference value. This shift is typically on the order of parts per million, ppm. The position and the number of these shifts are among the primary observables in NMR experiments for identifying the functional groups. The chemical shift can also be manipulated with special pulse sequences to improve spectral resolution, particularly in low-field.

Dipole-dipole coupling: It refers to the direct interaction between two spins, i.e., magnetic dipoles. The magnitude of this coupling effect is inversely proportional to the cube of inter-molecular distance. In certain liquids such as water, dipolar coupling is averaged to zero due to the rapid and random molecular motion. In contrast, in anisotropic liquids or solid-state samples, this interaction remains non-zero and can be exploited in various applications, such as NMR crystallography with amorphous materials. However, dipolar interactions also broaden resonance peaks and makes the elucidation of structures in solid samples more difficult. The magic-angle spinning (MAS) NMR technique was developed to address this issue.

J-coupling (spin-spin coupling or indirect dipole-dipole coupling): It originates from the hyperfine interaction between nuclear spin and the surrounding electrons, e.g., the $^1\mathrm{H} -^1 \mathrm{H}$ coupling in a $^1\mathrm{H} - \mathrm{C} -^1 \mathrm{H}$ group. It reflects the chemical bonding environment and appears as the multiplicity of split resonance peaks in the spectrum, such as doublets or triplets. Unlike chemical shift, J-coupling is independent of the external field strength and is therefore stated as a frequency offset in Hz.

2.3 NMR figures of merit

When evaluating an NMR spectrometer, the performance is defined by the interplay between sample-specific properties and the technical specifications of the hardware. While intrinsic factors set the theoretical signal limit, such as the gyromagnetic ratio and spin density discussed in last section, the spectral quality depends on the precision of the instrument engineering. To evaluate and optimize the NMR devices developed, four critical figures of merit are introduced and explained in this section: (1) B_0 field homogeneity across the sample volume, which dictates spectral resolution; (2) B_1 field homogeneity, which ensures uniform tip angles through consistent excitation; (3) excitation efficiency of the RF coil; and (4) signal-to-noise ratio (SNR) and limit of detection (LOD) as the ultimate metrics of sensitivity.

2.3.1 B_0 field homogeneity

Despite the magnitude of the B_0 field strength on different systems, ranging from around 1 T to around 30 T, B_0 field distortion is a common and major concern for NMR users since the field fluctuations affect the Larmor frequency directly [6].

Even in high-quality superconducting magnets, there can be slight imperfections in the coil windings or manufacturing tolerances, resulting in residual inhomogeneities. In the lab, the local field inside the magnet may suffer from: (1) thermal-induced distortions due to the non-uniform cooling of the magnet; (2) field shift due to persistent current decay; (3) mechanical vibrations caused by cooling systems, pumps, or nearby machinery; (4) variations in Earth's magnetic field strength and gradient in the laboratory environment, e.g., adjacent ferromagnetic materials. Local B_0 around the sample is also affected by the susceptibility mismatch between different materials in the sample coil.

By design, the field drifts should be compensated through proper lab maintenance, and more importantly, through the installed shimming system. The shimming coils are arranged around the gradient coils and the probe. Adjustable currents flow through these coils to actively control and correct the overall magnetic field according to the superposition principle [7, 8]. B_0 correction is achieved through various shim coil components corresponding to spherical harmonic terms, including Z1, Z2 and Z3 along the Z-axis, as well as X, Y, XY terms in the transverse plane (XY-plane), depending on the complexity of the system. In some instruments, passive shimming is also employed. This method uses pieces of steel or ferromagnetic pellets with suitable magnetic properties, which are positioned at specific locations inside the magnet bore to further improve field homogeneity.

Furthermore, when a new probe head is designed and fabricated, susceptibility matching between the detector and the sample container should be considered. In addition, interfaces between different construction materials should be placed away from the detection zone in order to reduce local magnetic field distortions.

There are several ways to characterize the homogeneity of the magnetic field at the center of an MR spectrometer. The spectral linewidth, also referred to as spectral resolution, is one of the most common quantification metrics. The linewidth can be calculated in several ways. One common definition is the full width at half maximum (FWHM) of the signal peak, which is easy to determine and allows straightforward comparison across different spectra. The peak width can also be measured at the baseline level or at a defined noise threshold (BBM), $\Delta v_{1/2}$, which is useful for broad peaks or poorly resolved spectra. Other approaches include estimating the linewidth by analyzing the autocorrelation function of the spectral line, which is suitable for rapid evaluation of broad peaks or solid-state NMR spectra, and fitting the peak to a mathematical function (e.g., Lorentzian, Gaussian, or a hybrid Voigt profile) for unresolved peaks or detailed line-shape analysis.

The linewidth can be broadened by unwanted field distortions, as calculated below:

$$\Delta\nu_{1/2} = \frac{1}{\pi \cdot T_2} + \Delta\nu. \tag{2.9}$$

Here, $\Delta\nu$ accounts for unwanted field distortions and experimental imperfections. T_2, the spin–spin relaxation time, determines the intrinsic linewidth of a nucleus in the spectrum, and is independent of static magnetic field imperfections [8]. In practice, however, the apparent transverse relaxation time T_2^* is observed. This parameter describes the decay of the FID signal

under real experimental conditions, incorporating both the intrinsic T_2 relaxation processes and additional dephasing caused by static magnetic field inhomogeneities. Therefore, T_2^* should be considered in theoretical predictions and experimental analyses rather than T_2 alone. A shorter T_2^* leads to a broader linewidth. In the equation above, the linewidth difference between T_2^* and T_2 is represented by the term $\Delta\nu$. The relationship between T_2^* and T_2 can be expressed as $\frac{1}{T_2^*} = \frac{1}{T_2} + \gamma\Delta B_0$, in which γ is the gyromagnetic ratio and ΔB_0 represents the local variations in the static magnetic field.

2.3.2 B_1 field homogeneity and excitation efficiency

While the B_0 field determines the spectral resolution, the RF field $\vec{B_1}$ governs the nuclear magnetization within the sample, as described in Eq. 2.6 and 2.8. Two primary parameters define the performance of this field: homogeneity and excitation efficiency. The non-uniformity of the B_1 field can reduce the maximum overall signal amplitude detected from each unit volume of the sample.

Assuming a uniform material distribution within the sample space, the magnetization of a randomly selected sample voxel $\vec{M}$ at a time τ can be expressed as:

$$\begin{aligned}\vec{M} =& M\sin(\omega_0\tau)\sin(\gamma B_{1u}I_{coil}\tau)\,\hat{x} + M\cos(\omega_0\tau)\sin(\gamma B_{1u}I_{coil}\tau)\,\hat{y} \\ &+ M\cos(\gamma B_{1u}I_{coil}\tau)\,\hat{z},\end{aligned} \tag{2.10}$$

where the coil is excited by a rectangular excitation pulse with a power of $P = r_{\text{coil}} \times I_{\text{coil}}^2$ and a pulse length that is much shorter than both T_1 and T_2 [4]. In an ideal experiment, every nucleus in the sample would experience the same flip angle (e.g., exactly 90° or 180°). In practice, however, the B_1 field strength varies spatially due to the specific coil geometry and the presence of conductive or lossy samples.

Following Eq. 2.8, the signal amplitude collected in the receive mode can be calculated as

$$\xi(t) = \overline{B_{1u} \times \sin(\gamma B_{1u} I_{\text{coil}}\,\tau)} \times M\omega_0 \times V_{\text{sample}} \times \cos(\omega_0 t)\,. \tag{2.11}$$

The maximum signal value is achieved at $\tau = {}^{\pi}/_{2\times\gamma B_{1u}I_{\text{coil}}}$, which corresponds to the 90° pulse width $\tau_{\pi/2}$, assuming a homogeneous B_1 field. The uniformity of B_1 is projected upon the term $\overline{B_{1u} \times \sin(\gamma B_{1u} I_{\text{coil}}\tau)}$ as the average effective field strength over the sample volume. Poor homogeneity leads to incomplete excitation in different regions. Meanwhile, dephasing may occur during complex pulse sequences, which can significantly reduce the signal intensity in multidimensional NMR experiments [9]. As a result, the measured signal intensity no longer accurately reflects the actual number of nuclei present in the sample.

There are several sources of non-uniformity in the B_1 field. First, it strongly depends on the RF coil design and the materials used. Each coil geometry produces a characteristic field distribution, and achieving an ideally homogeneous field is difficult. Identifying coil geometries that provide sufficiently homogeneous field while remaining compatible with the sample geometry is therefore an important topic, which will be discussed in Sec. 2.4.2. Metallic components in the

NMR setup can also distort the B_1 field through two main mechanisms: (1) eddy currents induced in metals by RF fields, which lead to spatially and temporally varying changes in the B_1 field strength, and (2) the skin effect, which alters the B_1 field distribution around metallic electrodes or conductors [10]. In addition, the electromagnetic properties of materials surrounding the coil and the sample itself, such as permittivity and conductivity, can influence the field distribution. As magnetic field strengths increase, e.g., in ultra-high field MRI, B_1 inhomogeneity becomes more pronounced due to the shorter RF wavelength and unwanted dielectric resonances within the sample [11]. Techniques such as RF shimming are therefore explored to compensate for distortions in both the amplitude and phase of the B_1 field, particularly in MRI applications [12, 13].

The nutation signal is a practical tool to evaluate the RF field inhomogeneity. It is defined as the NMR signal (ξ) collected over a sweeping time duration τ. Assuming a uniform B_1 field in the sample region and neglecting spin relaxation time, the signal evolves in a sinusoidal form with respect to τ and its amplitude depends on τ. However, B_1 inhomogeneity leads to an envelope to the sinusoidal signal, which decays over time. In experimental practice, the ratio of the signal amplitudes at pulse durations of 450° (or 810°) and 90° is calculated to quantitatively assess the B_1 field homogeneity, which is smaller than 1.

Excitation efficiency, often referred to as unit sensitivity, measures the coil's ability to convert input RF power into magnetic field strength. It is mathematically defined by the ratio B_1/i, where i is the current flowing through the coil. Efficient coils require less amplification from the power amplifier (PA) to reach the desired flip angle, which means a shorter pulse length. According to the principle of reciprocity, a coil that is an efficient transmitter is also a sensitive receiver. Therefore, optimizing the excitation efficiency is critical in the coil engineering. The excitation efficiency is usually evaluated as $\pi/(2\times\tau_{\pi/2})$ for 1 W excitation power to make a comparison between different coil designs.

2.3.3 Signal-to-noise ratio and limit of detection

Signal-to-noise ratio (SNR) is the primary metric for evaluating the quality of an NMR spectrum and the performance of the detection hardware. The signal formation is explained in detail in Sec. 2.2, in which the noise is also included. While the signal magnitude ξ is determined by nuclear magnetization and coil sensitivity, the experimental SNR is ultimately limited by noise. The noise mainly originates from the thermal noise of the coil (Johnson–Nyquist noise) and the sample. When working with limited sample volumes, the coil resistance becomes the primary noise contributor, as the skin depth effect and proximity effect lead to a high resistance. As derived from the principle of reciprocity, SNR can be characterized as follows:

$$SNR = \frac{V_{signal}}{V_{noise}} = \frac{|\xi|}{\sqrt{N_c}} = \frac{\overline{B_{1u} \times \sin\left(\gamma B_{1u} I_c \tau_{\pi/2}\right)} \times M\omega_0 \times V_{\text{sample}}}{\sqrt{4kTR_c}}, \tag{2.12}$$

in which ξ is the outcome of Eq. 2.11, N_c is the thermal noise produced by the coil, T corresponds to the coil temperature and R_c is the coil resistance, and ω_0 is the resonance frequency.

Assuming a unit sample volume being excited at a fixed Larmor frequency with a constant coil temperature, the SNR can be further simplified as:

$$SNR = \frac{|\xi|}{\sqrt{N_c}} = \frac{\overline{B_{1u} \times \sin\left(\gamma B_{1u} I_c \tau_{\pi/2}\right)}}{\sqrt{R_c}} \propto \frac{\overline{B_{1u}}}{\sqrt{R_c}} = \frac{\overline{B_1}}{i \times \sqrt{R_c}}. \tag{2.13}$$

$i \times \sqrt{R_c}$ is equivalent to $\sqrt{P_c}$. This proportional relationship is very useful for NMR hardware engineers. This relationship highlights that high sensitivity is achieved by maximizing the B_1 field produced per unit current (excitation efficiency) while minimizing the resistive losses in the coil. A higher SNR indicates a clearer and more reliable spectrum, enabling better interpretation of molecular structures and interactions. It is crucial in experiments involving low-concentration or low-volume samples, where weak signals may be obscured by noise.

Another common concept similar to SNR is sensitivity, which is already mentioned in the previous section. While SNR describes the data quality, sensitivity refers to the system's ability to detect weak signals from low-concentration analytes. A higher SNR generally correlates with increased sensitivity. However, sensitivity can also be affected by factors like sample preparation and experimental design. When SNR is calculated from experimental data, which is affected by the factors mentioned, sensitivity and SNR provide the same information and can be used alike. A critical variant for micro NMR hardware is mass sensitivity, which scales the SNR by the measured sample mass. It emphasizes the ability of an NMR system to detect signals from small amounts of sample material.

The limit of detection (LOD) or normalized LOD (nLOD) is a parameter derived to measure the NMR sensitivity [14]. Principally, it is the inverse of the sensitivity, i.e. the minimum sample amount or spins required to obtain a baseline SNR (SNR = 3). The nLOD enables direct and fair comparison across different NMR setups, as it is independent of acquisition parameters such as bandwidth, number of data points, or signal averaging. The Mass LOD is defined as:

$$nLOD_m = \frac{3 n_s \sqrt{t}}{\mathrm{SNR}}, \tag{2.14}$$

in which n_s is the measured sample amount in mol, t is the measurement time, and SNR is the acquired signal-to-noise ratio. t can be estimated as a multiplication of the scan number and acquisition time per scan. For a fair comparison among different researches, SNR obtained from an arbitrary spectrometer with a system frequency ω_s could be corrected with a ratio of $(600/\omega_s)^{\frac{4}{3}}$, as used in this work on a 500 MHz spectrometer.

2.4 NMR hardware

The performance of an NMR experiment is fundamentally constrained by the hardware's ability to excite, control, and detect nuclear magnetization. A conventional NMR system is built as a modular platform, as shown in Fig. 2.2. First of all, it consists of a high-field superconducting magnet, such as the 11.7 T vertical-bore magnet employed in this work. Commercial systems now can reach magnetic field strengths of up to 30.55 T (corresponding to 1.3 GHz for ^{1}H). Shimming and gradient coils remains indispensable around the bore to ensure sufficient field

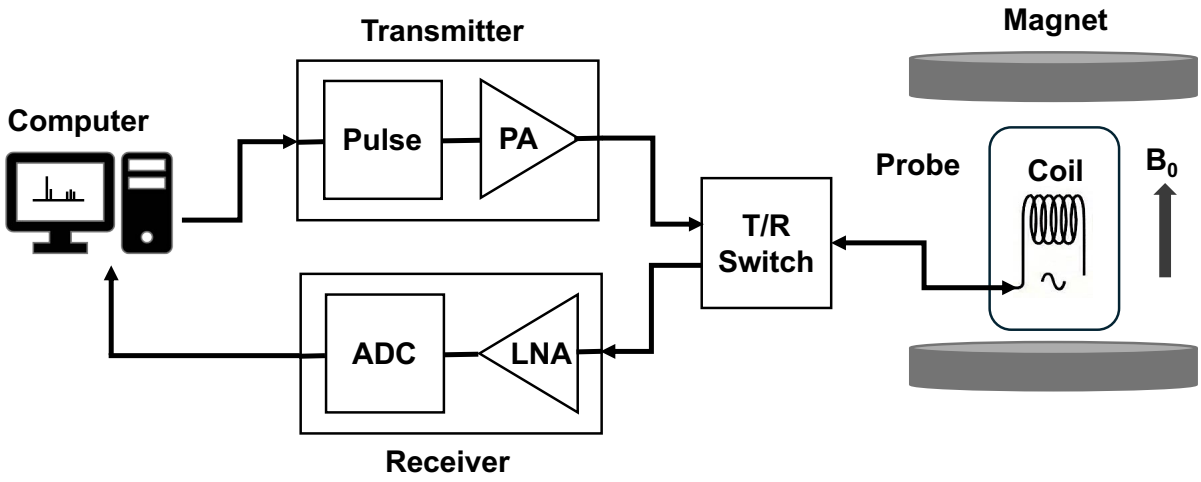

Figure 2.2: *Schematic diagram of the NMR spectrometer hardware and signal flow. The host computer controls the transmitter, which consists of a pulse programmer and a power amplifier to generate the RF excitation pulse. The T/R switch acts as the central duplexer, routing these pulses to the RF coil within the NMR probe, which is centered inside the static magnetic field B0 of the magnet. During the detection phase, the T/R switch directs the weak nuclear signal from the coil to the receiver. The receiver mainly consists of a low-noise amplifier (LNA) and an analog-to-digital converter (ADC) for subsequent data processing on the computer.*

homogeneity and to enable spatially resolved experiments. The electronic heart of the system is the NMR console, which houses the transmitter and receiver. The RF pulse generator and power amplifier make up the transmitter network (TX). The pulse is amplified to a power level of 10 W to 1000 W [15]. The receiver network (RX) has a low-noise amplifier (LNA) and analog-to-digital converter (ADC), which prepares the FID signal for spectrum processing. The LNA is essential because the raw NMR signal is usually very weak and requires enhancement for precise processing. The ADC digitizes the analog FID signal so it can be Fourier transformed by the host computer. A high-speed T/R switch directs the transmit pulse to the probe and the NMR signal to the receiver. It also protects the sensitive receiver from the high-power transmit pulse. While traditional high-field systems offer maximum sensitivity, benchtop NMR systems have gained prominence for their portability and relatively low cost with highly integrated electronics, albeit at the trade-off of lower spectral resolution, which will be discussed in following sections.

The most critical interface in this signal chain is the NMR probe. This removable module is inserted into the magnet bore and serves as the housing for the NMR RF coil and electronics. While probes are broadly categorized into liquid-state and solid-state (MAS) configurations, their underlying efficiency is governed by the same electromagnetic principles. To ensure maximum spectral resolution and sensitivity, the coil must be precisely positioned within the homogeneous B_0 region of the magnet. Furthermore, the sample should be correctly positioned within the RF magnetic field by the coil, which is vital for achieving uniform excitation of the sample and optimal detection of the NMR signal. The tuning and matching network is placed near the coil to minimize signal losses and ensure maximum power transfer efficiency.

To optimize the NMR devices developed in this research, the following sections provide a detailed engineering analysis of the three core hardware components: NMR probe, NMR coil geometry and tuning and matching network.

2.4.1 NMR probe

NMR probes consist of several critical components, including a part of the transceiver circuit, tuning and matching circuit, fluidic channels for cooling, a gradient sleeve, one or multiple NMR coils and the sample container. The probe head assemblies are refined to hold samples precisely within the magnet's homogeneous center as well as homogeneous RF field region, ensuring consistent experimental results. While the primary B_0 shimming and gradient coils are typically integrated into the magnet bore, the probe environment must be carefully engineered to minimize interference with these fields.

The probe materials and shielding must be designed to mitigate eddy currents. When magnetic field gradients are pulsed for spatial encoding or coherence selection, they can induce currents in nearby conductive materials, leading to signal artifacts and field distortions [16]. Furthermore, the probe must be constructed from materials with matched magnetic susceptibilities to avoid introducing local inhomogeneities into the high-resolution B_0 sweet spot. Additionally, the components around the coil must be non-magnetic and resistant to RF interference to ensure uncompromised performance.

Prior to measurement, the sample is inserted into the RF coil via a customized sample holder or NMR tube. Depending on the system, loading is achieved through a pneumatic automatic lifting system or manual insertion. The holder ensures that the sample is precisely and reproducibly centered relative to the RF coil. While borosilicate glass tubes are the standard for liquid-state NMR, polymers or ceramic compounds are utilized for specialized applications, such as the rotors in Magic Angle Spinning (MAS) probes. These tubes must be machined with high precision to allow for easy insertion while maintaining a high fill factor, which is critical for sensitivity.

To maintain experimental stability, a temperature control system is typically integrated throughout the probe body, regulated by an external fluidic or gas-flow unit. Precise regulation of the thermal condition around the RF coil and sample is essential for reducing thermal noise, maintaining the stability of biological samples, and performing variable-temperature studies. In specialized solid-state NMR configurations, the probe also incorporates a pneumatic bearing and drive system that enables the rotor to spin at high frequencies at the magic angle relative to the B_0 field direction.

In summary, the NMR probe is a sophisticated electromechanical assembly designed to maintain the sample in a controlled environment while enabling high-fidelity signal detection. The structural integrity of the probe body is important to achieve high-resolution spectra without distorting the static field. Having established the role of the probe as the primary interface between the console and the sample, the following section evaluates the geometry of the NMR coil, which determines the system's sensitivity and the spatial distribution of the RF field.

2.4.2 NMR coil geometry

The NMR coil, positioned at the isotropic center of the B_0 field, plays a critical role in determining the performance of the probe. A few coil geometries have been selected from the coil family and utilized for NMR detection. This section outlines the fundamental principles of NMR coil design. The typical NMR coil geometries are reviewed, and the practical considerations for optimizing their figures of merit metrics are discussed.

Coils can be modeled as an inductor L in series with a small resistance R, $L+R$. For an ideal inductor, the inductance is defined by its geometry and material properties, and the inductance is given by $L = \frac{\phi_M}{I}$, where ϕ_M is the magnetic flux, i.e., the product of the magnetic field B_1 and the enclosed area A. The energy stored in the inductor is expressed as $W_L = \frac{1}{2}LI^2$. The impedance of a series resonance circuit is calculated as:

$$Z = j\omega L + R - \frac{-1}{j\omega C}, \tag{2.15}$$

where C is the total capacitance applied in the circuit. This series resonance circuit provides a narrow frequency band centered around the resonance frequency, which corresponds to the Larmor frequency of the detected nucleus. The quality factor (Q) is defined as the ratio of the energy stored in the inductor and the thermal energy dissipated in the circuit per current cycle:

$$Q \equiv \frac{W_L}{W_R} = \frac{\omega L}{R} = \frac{1}{R}\sqrt{\frac{L}{C}}, \tag{2.16}$$

in which W_R is the thermal dissipation on the resistor [17]. A high Q indicates high power efficiency in the coil. According to another commonly used, nearly equivalent definition, the quality factor is given by the ratio of the resonance frequency to the bandwidth ($\Delta\omega = \omega_0/Q$). Consequently, a higher Q also implies greater frequency selectivity. In general, a high Q factor is desirable for maximizing the voltage step-up and filtering out-of-band noise, thereby significantly enhancing the SNR. From the equation above, it follows that a larger inductance leads to a higher Q. In practice, however, the inductance cannot be increased arbitrarily, since enlarging the inductor typically also increases its resistance, which ultimately limits the achievable Q.

There is a wide variety of NMR coil geometries, which can generally be categorized into two groups, i.e., 3D (volume) coils and 2D (planar) coils, as shown in Fig. 2.3. In the diagram, the different coils are arranged with the same B_0 field direction, and the effective sample region for each coil is displayed in blue. The selection of a specific coil geometry is primarily determined by the sample's volume, geometry, and required orientation relative to the static magnetic field B_0.

Volume coils are designed to surround the sample, providing a highly uniform RF field throughout a three-dimensional space. Typical volume coils are:

- **Solenoid coil** as one of the most widely used coil geometries, consists of a wire wound in a helical shape around a cylindrical form. It creates a uniform magnetic field inside along the central axis of the cylinder and is able to provide a strong magnetic field and a high SNR due to its low resistance and efficient energy storage. Solenoid coils are particularly

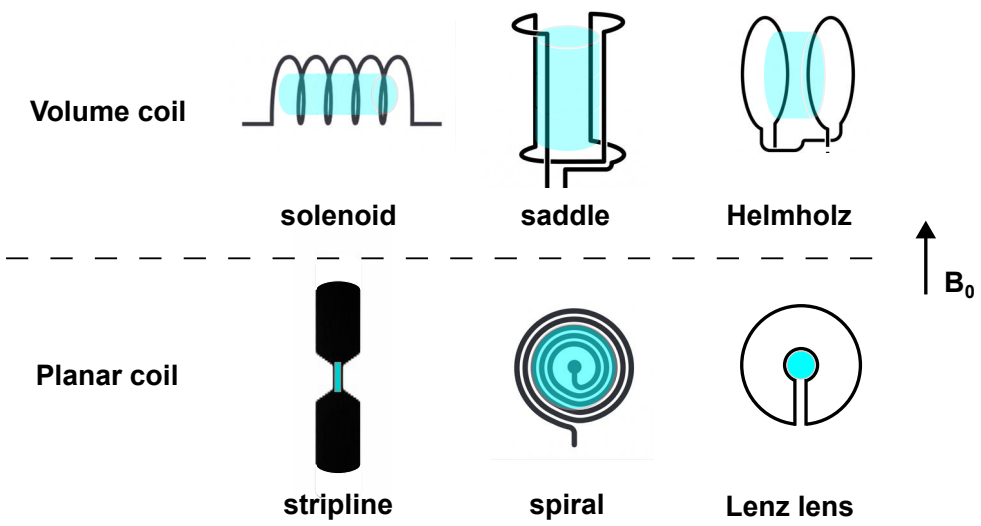

Figure 2.3: *Overview of common NMR coil geometries. The top row illustrates volume (3D) coils, including the solenoid, saddle, and Helmholtz coils. The bottom row displays planar (2D) coils, such as the spiral, stripline, and Lenz lens designs. The coils are oriented as in the working configuration for the given B_0 field direction. The blue shaded regions represent the active sample volume for the respective coils.*

well-suited for the cylindrical sample tubes typically used in liquid-state NMR, which maximize the filling factor and thus have efficient coupling with the sample. The facts that the uniform magnetic field is limited to the center space and that the coil needs to be placed orthogonally to B_0 field limit its versatility in application. It is a popular choice in micro NMR and MAS applications.

- **Saddle coil** consists of a single wire that is shaped like two saddles facing each other. This configuration is particularly beneficial for achieving better homogeneity in the magnetic field over a larger area compared to traditional solenoid coils [18]. It couples less strongly to surrounding conductive materials, like sample holders, than tightly wound solenoids, reducing unwanted loading effects in certain cases. However, the geometry and construction of saddle coils can lead to higher resistive losses compared to an optimized solenoid, potentially lowering the Q factor. The open structure of a saddle coil provides easy access for various sample sizes and types, making it suitable for different experimental setups. They allow the sample tube to be inserted along the B_0 direction while generating the necessary transverse B_1 field. The construction of saddle coils can be more complex than other simpler coil geometries, potentially increasing manufacturing costs. On the other hand, saddle coils can be arranged in multi-element arrays. In such setups, each element covers a specific region, which is advantageous in parallel imaging or in experiments requiring spatial localization.
- **Helmholtz coil** is made up of two parallel coaxial coils, providing a uniform magnetic field at their geometrical center. It is a simpler alternative for volume excitation and allows for easy sample insertion/removal and integration into customized probe head components. The mathematical description of the magnetic field produced by a Helmholtz configura-

tion is well known, which can simplify the design and calibration process for experiments needing precise field control. The Helmholtz pair offers a better field uniformity over a larger volume than single solenoid coils but a lower sensitivity than solenoid coils due to a lower magnetic field strength at the center and a lower coupling efficiency with its less compact structure. To achieve the desired field uniformity, Helmholtz coils are often larger than other coil geometries, making them less practical when space is at a premium or when working at very high frequencies. In the construction, it requires careful alignment and calibration of the rings to ensure optimal performance.

In contrast to volume coils, planar (2D) coils are characterized by a flat structure, and are designed to provide localized sensitivity. The B_1 field strength is maximum in the region adjacent to the conductor surface. While planar coils lack the specific axial homogeneity of 3D coils, they offer advantages in sufficient SNR for thin-film samples and microfluidic interfaces where the filling factor can still be maximized through extreme proximity. Typical planar coils are as follows:

- **Stripline coil** is composed of flat conductors arranged in a parallel configuration, typically sandwiched between dielectric materials. This design is often used in high-frequency applications due to its compact size and ease of integration into RF circuits. Stripline coils provide good sensitivity and magnetic field homogeneity, making them particularly effective for small-volume samples, such as microfluidic or lab-on-a-chip applications [19]. The flat geometry allows for a smaller footprint, making stripline coils ideal for miniaturized NMR systems or portable devices. Striplines are scalable and can be adapted for different sample sizes. Additionally, stripline coils are well suited for integration with microfluidic systems, enabling real-time monitoring of chemical reactions or biological processes with low sample heating. Stripline coils can operate effectively over a wider range of frequencies, which is advantageous for applications requiring multiple nuclei detection [20]. Achieving uniform magnetic fields on a stripline coil requires precise and complex manufacturing techniques [21].
- **Spiral coil** is designed in a flat spiral shape, often used in miniaturized applications or microfluidic systems. It has a compact structure and is ideal for small samples or microfluidic applications where space is limited. Planar spiral coils can be fabricated using standard microfabrication techniques, enabling mass production and integration with other microelectronic components. Spiral coils at a micro scale can perform broadband detection, capable of detecting multiple nuclei simultaneously. However, the planar spiral has a low magnetic field homogeneity, since it suffers from a rapid B_1 field drop-off as distance from the coil increases. It typically provides a lower SNR compared to larger solenoid or Helmholtz coils due to a smaller effective volume and additional noise, due to interconnections between circuit elements and the coil [22]. At high frequencies, the AC resistance of planar spiral coils can increase significantly due to skin and proximity effects, increasing thermal noise greatly.
- **Lenz lens coil** utilizes inductive elements arranged to enhance the magnetic field at the sample location [23, 24]. Lenz lenses can focus the magnetic field of a larger RF coil into a

smaller spatial region, thereby increasing the local flux density and improving SNR. Unlike LC resonators, Lenz lenses are non-tuned and can operate over a wide frequency range, making them suitable for broadband applications [25]. Lenz lenses can be easily tailored to specific applications and are straightforward to fabricate using simple conductive materials like wire or copper foil. When it is driven by an outer coil, the inserted Lenz lens does not significantly affect the tuning condition, simplifying their integration into existing NMR setups. However, it shows limited effectiveness for extremely large detection coils and evitable reduces the total sensitive volume.

A minor subgroup of coil geometries is the 2.5D coil, which has some three-dimensional aspects but is not fully 3D [26, 27, 28]. This term typically refers to planar coils with increased thickness, stacked planar coils with interconnects, or coils with partial vertical components in some studies. So far, there is no strict boundary between 2.5D and 2D coils. Since the coil structures are still essentially planar, this work discusses them together.

2.4.3 Impedance tuning and matching

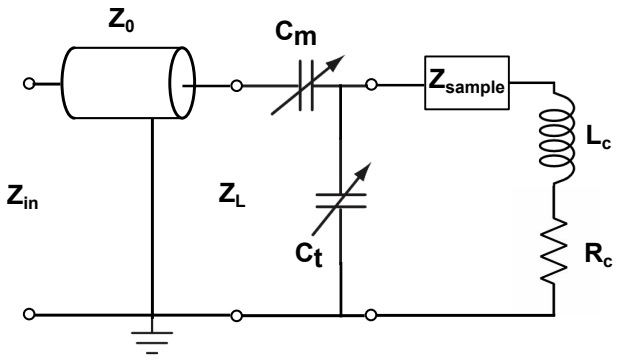

Figure 2.4: *Equivalent circuit model of the NMR tuning and matching network. The network comprises a basic tuning and matching network with two capacitors in order to transform the complex impedance of the NMR coil and sample-induced spins to the characteristic impedance of the transmission line. The resulting input impedance is calculated at the preamplifier interface.*

To achieve maximum sensitivity and power efficiency, the NMR coil is integrated into a network that performs two distinct functions: tuning and matching. The purpose of the tuning and matching network is to tune the resonant frequency to the nucleus' Larmor frequency, and to match the coil impedance to the transmission line, thereby ensuring efficient signal transmission and reception and maximizing the SNR. In its most fundamental form, tuning is achieved with a parallel variable capacitor connected to the coil, and matching is realized with a series variable capacitor. To quantify the performance of an NMR probe, it is necessary to model the RF coil within a lumped-element framework. Fig. 2.4 illustrates the standard resonant matching topology, where the coil is represented by its inductance and series resistance, coupled with the impedance contribution from the nuclear spins Z_{sample} [29]. The secondary matching and tuning capacitors transform this complex load into the network impedance Z_{L}, which can be calculated as [17]:

$$Z_{\mathrm{L}} = \frac{1}{iC_{\mathrm{t}}\omega + \frac{1}{R_{\mathrm{c}}+iL_{\mathrm{c}}\omega+Z_{\mathrm{sample}}}} - i\frac{1}{C_{\mathrm{m}}\omega}. \tag{2.17}$$

It is noted that Z_{s} is affected by the frequency offset from the Larmor frequency $\Delta\omega$. When the coil is matched, a maximum power transfer between the connected transmission line (usually a coaxial cable) and the NMR coil is realized. Depending on the specific requirements of the resonance circuit on the coil, C_{t} and C_{m} shown in Fig. 2.4 can be replaced by circuit units consisting of multiple capacitors and/or inductors. In some cases, a combination of several components is necessary to achieve higher tuning and matching accuracy than that provided by a single fixed-value capacitor or inductor. On the other hand, more complex tuning and matching units, such as trap and tank circuits, can enable single-input, multi-tuned NMR detectors, which will be discussed further in Sec. 2.6.1.

In practice, due to the loading effects of different samples and the interaction between tuning and matching, the tuning and matching process is often iterative and time-consuming. Automated tuning and matching systems with computer control have therefore been introduced [30, 31, 32]. In these systems, manual capacitor adjustment is replaced by motorized capacitors or electronic tuning elements. Automatic tuning and matching is particularly useful in in-situ NMR measurements for tracking intermediate reaction products.

When the tuning and matching circuit is connected to a preamplifier via a transmission line, based on Eq. 2.17, the input impedance seen at the preamplifier can be expressed as:

$$Z_{\mathrm{in}} = Z_0 \frac{Z_{\mathrm{L}} + Z_0 \tanh(x)}{Z_0 + Z_{\mathrm{L}} \tanh(x)}, \tag{2.18}$$

where Z_0 is the characteristic impedance of the transmission line, which is typically $50\,\Omega$ [33]. x is the electrical length of the cable. According to Eq. 2.18, transmission lines can also be used to adjust tuning and matching properties of the coil, and to provide good signal isolation between different channels [34, 35]. The use of transmission lines in multi-resonance probes will also be discussed in Sec. 2.6.1.

NMR sensitivity is not only determined by the coil efficiency, but also by the noise management within the transceiver chain. When the coil is tuned and matched, spin noise and absorbed circuit noise are affected by the tuning condition. For instance, the spin noise, due to residual magnetic fluctuations, is actually enhanced by the tuned circuit. The circuit noise, together with the spin noise without the preamplifier network, can be calculated as follows:

$$N_{\mathrm{in}}^2 = 4kT\,\mathrm{Re}\left[Z_{\mathrm{in}}\right], \tag{2.19}$$

which is a more complete expression of N_{c} in Eq. 2.12, demonstrating the noise power spectral density, or more precisely, the squared noise voltage spectral density with the resistance term being considered. At the preamplifier input, the noise voltage level can be calculated as:

$${V_{\mathrm{Noise}}^*}^2 = \left(N_{\mathrm{in}}^2(\Delta\omega) + |I_{\mathrm{N}}|^2 \cdot Z_{\mathrm{in}}^2 + |V_{\mathrm{N}}|^2\right) \left|\frac{Z_{\mathrm{p}}}{Z_{\mathrm{in}} + Z_{\mathrm{p}}}\right|^2, \tag{2.20}$$

in which Z_{P} is the input impedance of the preamplifier, I_{N} and V_{N} are respectively the current and voltage noise sources introduced by the preamplifier [29].

By accounting for the noise sources described above, the optimal Signal-to-Noise Ratio ($\mathrm{SNR_{opt}}$) can be derived. When Z_{in} is a pure resistive value and equal to $^{V_N}/_{I_N}$ [29, 36], the optimal SNR is achieved as follows:

$$\mathrm{SNR_{opt}} = \frac{\xi}{\sqrt{R_c}\sqrt{4kT + 2I_N V_N}}, \tag{2.21}$$

ξ is the nuclear magnetization, as explained previously in Sec. 2.2. Unlike Eq. 2.13, this expression provides an alternative perspective for evaluating SNR by taking the tuning and matching circuit and the transceiver signal path into account.

2.5 Miniaturization in NMR

Miniaturization in NMR refers to the development of compact, portable systems that retain the analytical capabilities of conventional benchtop or large-scale NMR spectrometers. The growing demand for miniaturized NMR lies in its potential to enable applications in on-site diagnostics, environmental monitoring, and in general, micro-scale sample measurement traditionally inaccessible to bulkier systems [37, 38]. It is also critical to achieve a resolution and sensitivity comparable to, or even better than those of bulky NMR systems. To provide a comprehensive overview of this field, this section reviews the architectural and methodological developments across four key aspects: micro NMR systems, micro coil designs, optimization using simulation tools and advanced microfabrication techniques.

2.5.1 Miniaturized NMR systems

A complete traditional NMR system explained before is bulky and costly, with a standing electronic magnet, nitrogen cooling chamber, cabinets housing signal processing and amplification, and an arm-long delicate probe.

A benchtop NMR system primarily includes a permanent magnet, compact NMR electronics, and a micro RF coil. The pursuit of miniaturized NMR systems began in the late 20th century, driven by the advances in microfabrication, CMOS front-end electronics and compact magnet. Early milestones include the development of palm-size permanent magnets in the 1990s and the integration of micro coils in the 2000s to enhance mass sensitivity [39, 40, 41]. For a center-field permanent magnet, the magnet material, magnet assembly design, and the shimming strategy determine the field quality for NMR measurement, which was reviewed by Blümich [42]. The NMR electronics are mainly comprised of three modules: a pulse sequencer, an RF transmitter, and a low-noise receiver [43, 44]. Smaller systems consume less power and require fewer consumables. By reducing size and cost, these systems become more widely available and can be deployed in more settings, e.g., on-site diagnostics. Miniaturized components also facilitate seamless integration with microfluidics and lab-on-a-chip platforms, enabling automated, high-throughput analysis [45, 46]. While miniaturization offers transformative potential, it introduces technical hurdles. In compact magnets, sensitivity losses due to reduced sample volumes and magnetic field inhomogeneity remain critical challenges [47, 48]. Noises from the signal process-

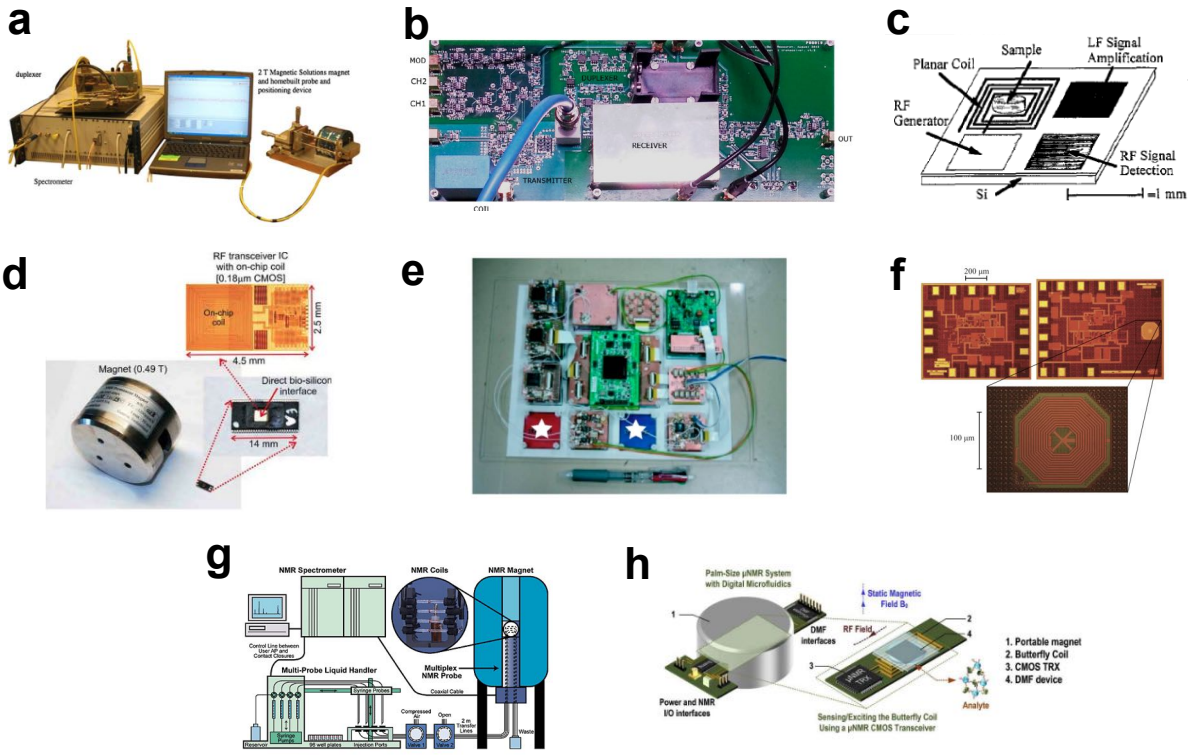

Figure 2.5: *Different miniaturized NMR probes/systems. (a) Table-top micro coil NMR setup (Reproduced from Ref. [49] with permission from Elsevier). (b) Reproduced from Ref. [50] with permission from Elsevier. (c) An integrated NMR magnetometer (Reproduced from Ref. [39] with permission from Elsevier). (d) 1-chip NMR system (Reproduced from Ref. [48] with permission from IEEE). (e) Assembly of the compact NMR spectrometer (Reproduced from Ref. [51] with permission from AIP Publishing). (f) Single-chip transceivers for two coils (Reproduced from Ref. [52] with permission from AIP Publishing). (g) Automation system with a multiprobe liquid handler (Reproduced from Ref. [53] with permission from American Chemical Society). (h) Portable electronic-automated µNMR system (Reproduced from Ref. [54] with permission from IEEE).*

ing electronics also harm the detection sensitivity. Additionally, thermal management in densely packed systems and signal-to-noise trade-offs demand innovative engineering solutions.

To address these limitations, the advances in magnet designs are of critical importance. The control of magnet homogeneity was the main limiting factor for the miniaturization of the magnets while maintaining the magnitude of the field strength. A promising direction is the design of compact magnet assemblies with permanent magnets, which decreases the magnet size by up to 2 orders of magnitude and is energy efficient [55]. Improved new permanent magnetic materials and magnet assembly geometries provide the chance to scale the size of the magnet down to the limit of millimeter-sized structures. One important promising magnet design is the Halbach array, which organizes a group of magnet elements with respective polarization directions in order to create a homogeneous field within the ring [56]. The field strength can be around 1 T to 2 T. As shown in Fig. 2.5 (a), Demas *et al.* presented a benchtop NMR setup with a small purchased

2 kg Halbach magnet, which provided a 2 T magnetic field [49]. Another breakthrough is smaller superconducting magnets with novel magnet materials. A miniature high-temperature superconductor (HTS) magnet system was reported for a magnetic field of around 3 T at a weight of about 2 kg with a rotary microcooler [57]. The cylindrical magnet body was 20 mm in diameter and 20 mm in length.

Another good opportunity of NMR system miniaturization lies in a higher integration level of electronics. The advances in microelectronics on customized PCB boards or CMOS chips with NMR performance enhancement have been presented in details by several reviews [44, 45]. Most of the modules of a modern NMR spectrometer can be realized by the integrated circuits, and in the end assembled onto single customized chip [58]. Fig. 2.5 (b) presented an NMR front-end electronics with transmission and reception networks by Mandal *et al.* [50]. The setup worked broadband without resonant circuits in low-field NMR, as the RF frequency was switched and calibrated quickly by the electronics and the loading effect of the sample was mitigated.

At the same time, due to a higher level of hardware integration and processing performance, CMOS technology has delivered plenty of promising miniature NMR systems. Fig. 2.5 (c) showed the diagram of a partially integrated magnetometer based on continuous-wave (CW) proton NMR by Boero *et al.* back in 1998 [39]. In this design, a planar coil was electrodeposited on a glass substrate with a diameter down to 2 mm and was bonded to a CMOS board. Sun *et al.* further reduced the size of 1-chip NMR system in Fig. 2.5 (d) [48]. The system weighted 0.1 kg, in which a CMOS RF transceiver was able to work with different micro coils at ca. 20 MHz. The fabricated on-chip planar coil held 5 µL sample despite a very low Q of 1.9 due to the direct current (DC) resistance. Takeda **et al.** proposed a high-field micro NMR system at around 400 MHz [51, 59]. The spectrometer assembly was built with a commercial FPGA chip connecting a series of modules, as shown in Fig. 2.5 (e). Another single-board design of a miniaturized spectrometer was at a size of 50 mm by 250 mm, and was able to conduct NMR relaxometry with a fluidic sample below 20 µL [60]. An 1 mm^2 CMOS broadband transceiver chip is presented in Fig. 2.5 (f) by the team of Boero [52, 61]. It could work from 1 MHz to 1 GHz. The integrated coil had an outer diameter down to 150 µm.

Compact, and robust NMR systems facilitates NMR probe coupled with micro fluidic systems for flow control and chemical reaction monitoring. Fig. 2.5 (g) presents a four-coil probe for simultaneous detection of four sample flows designed by Macnaughtan *et al.* [53]. The micro solenoid coils were stacked along the static field direction within one probe and each was 1.7 mm in outer diameter. A mricromachined fluid mixer was reported as being connected to a micro NMR probe to study the continuous protein-solvent interactions at different time points [62]. The mixer and the coil were connected by flexible fused-silica capillaries. A more compact design is a single-chip solution, where the fluidic channel was coupled with the RF coil directly. A miniaturized diagnostic magnetic resonance was presented, which consisted of a board with electroplated micro coil array and microfluidic networks for sample mixing and processing [46]. Each micro spiral coil was placed above a flow patch. Planar stripline coil was also frequently combined in coupling with the microfluidic structures [63, 64]. Lei *et al.* proposed a digital

microfluidic device, which automated the sample operation, increased the efficiency of multiple sample measurements, as shown in Fig. 2.5 (h) [54]. Automatic sample management system was an important feature on a modern NMR system and this work showed the prospect of realizing it on a micro NMR system [65].

NMR system miniaturization has also been boosted by the advances in hyperpolarization techniques, machine learning-assisted data processing. The overall exploration on compact, and even on-a-chip NMR systems shows the prominent potential for emerging applications in portable metabolomics, battery diagnostics, and nanomaterials characterization.

2.5.2 Miniaturized coils

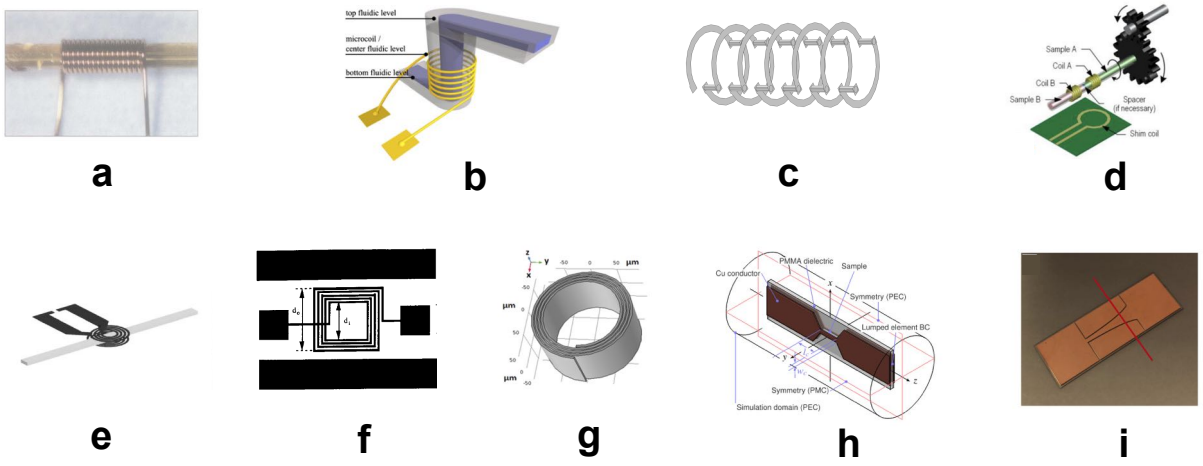

Figure 2.6: *Different designs of miniaturized NMR coils for NMR applications. (a) Micro coil and polyimide-coated, fused-silica capillary (Reproduced from Ref. [66] with permission from American Association for the Advancement of Science). (b) Solenoidal micro coil by wire-bonding (Reproduced from Ref. [67] with permission from IOP Publishing). (c) Quasi-solenoidal micro coil (Reproduced from Ref. [68] with permission from IEEE). (d) Configuration with 2 samples occupying 2 separate NMR coils (Reproduced from Ref. [69] with permission from American Chemical Society). (e) Helmholtz coil (Reproduced from Ref. [70] with permission from Royal Society of Chemistry). (f) Multiturn planar micro coil (Reproduced from Ref. [71] with permission from IEEE). (g) Scroll micro coil (Reproduced from Ref. [72] with permission from MDPI). (h) Stripline coil model (Reproduced from Ref. [73] with permission from Elsevier). (i) Tapered stripline coil (from Ref. [74] with permission from Elsevier).*

Dating back to the 1960s, micro coils in the shape of a solenoid with a diameter of several millimeters were successfully employed, and line spectra from a biological sample were presented [75]. Since the 1990s, there has been a great thrust to utilize various micro coils on traditional NMR systems, which is further a cornerstone of miniaturized NMR systems shown in the last section [71, 76]. Based on the detailed arguments in Sec. 2.2 and 2.3, the signal amplitude per unit sample volume depends on the B_1 field strength from the unit applied current. Thus, a more compact coil winding is crucial for higher sensitivity. This requirement leads to an increase in the coil resistance due to the proximity effect occurring inside the thin wires and a higher total

length of the conductor. In parallel, the coil has a lower self-resonance frequency because of a longer conductor length and a higher inter-turn capacitance. However, these side effects can be mitigated by miniaturizing the coil as a whole. The combination of a micro coil and a detected sample with decreased sample volume brings a series of benefits, including less noise introduced by solvent impurities, lower amount of deuterated solvents required for signal separations, and a lower loading effect from electrically conductive samples [41]. The development of miniaturized coils capitalizes on emerging applications that demand high measurement sensitivity, high spectral resolution, and easy integration of multiple NMR coils into one probe head. Several reports elaborated on the miniaturization of NMR coils with different geometries [37, 38, 41, 77, 78].

As mentioned before, the solenoid coil, as one of the most widely used coil geometries, was scaled down first by winding thin wires around capillary tubes, which was a straightforward yet robust solution for micro RF detectors [76, 79]. With this approach, Olson *et al.* described a nanoliter-scale NMR detection unit using a fused silica capillary, as shown in Fig. 2.6 (a) [66]. It enabled NMR measurement of capillary electrophoresis separations with a sensitivity enhancement of up to 130 fold compared to the result obtained with a standard 5 mm tube on a 300 MHz magnet. Due to less loaded sample and a higher excitation efficiency of the micro solenoid, the data acquisition time was reduced by a factor of around 16000. It is noted that using susceptibility-matching medium between the coil and the sample has been a common practice, e.g., FC-43 susceptibility matching liquid (3M Corporation, St. Paul, MN).

In 2019, Tang *et al.* presented a functional detector unit under extreme conditions (150 °C °, 900 bar) consisting of a micro solenoid coil wound around a sealed sample tube [60]. A novel method to fabricate solenoid coils was wire-bonding. As shown in Fig. 2.6 (b), Meier *et al.* utilized a 25 µm thick gold wire and made a 7-turn coil with a diameter of 200 µm by wire-bonding [67]. This method could further easily manufacture a phased array of solenoid coils. In one project, seven micro coils were arranged hexagonally and embedded in SU-8 with better stability [22]. Fig. 2.6 (e) showed an innovative arrangement of a multi-coil probe head [69]. Four separate micro solenoid coils were controlled by a gear system to perform sequential scans for multidimensional NMR and high throughput.

One significant advantage of the solenoid coil is its regular shape, producing an even magnetic field well contained inside the coil and a high electromagnetic conversion efficiency [78]. Apart from the standard solenoid geometry, there have also been other variations of micro solenoids. One quasi solenoid NMR coil was reported, which connected a series of printed circular conductor strips with through-layer vias based on LTCC techniques, providing extremely high mechanical and chemical stability, as shown in Fig. 2.6 (c) [68]. The axial length of the 6-turn micro coil was 1.5 mm fabricated from 12 layers. By using a bar-shaped wire, Le *et al.* presented deformed micro solenoid coils with a square cross section, which were directly compatible with CMOS electronics [28].

Miniaturization in Helmholtz coils was also explored. In one work by Popovic *et al.* as shown in Fig. 2.6 (e), microfabricated Helmholtz coils presented a much narrower line width than the solenoid coils fabricated using the same method at the cost of a slightly lower sensitivity

[70]. The wire bonder facilitated micro Helmholtz device as well. Spengler *et al.* fabricated a micro Helmholtz coil with a diameter of 1.2 mm [80]. The 0.55 mm spacing between two coil loops accommodated an exchangeable sample chip, showing a sub-Hz spectral resolution in heteronulcear NMR.

Taking advantage of various micro electro-mechanical system (MEMS) techniques, planar coils of different geometries have been readily scaled down and present great potential in NMR spectroscopy. As early as 1994, micro planar spiral coils were fabricated with gold using microlithography on a gallium arsenide substrate, and the coil was used on a 7 T magnet for proton NMR [71], as shown in Fig. 2.6 (f). More strictly speaking, it was a planar square coil [81, 82, 83]. Glass wafers have been a common substrate material for micro planar spirals [39, 84]. Micro planar spirals can be designed and manufactured together with microreactors, being assembled as microfluidic chips [19]. Usually, electrical and fluidic connections should be adjusted away from the detection area. However, this integrative design method avoids abrupt material changes surrounding the RF resonator and lowers the field distortion around the detection region. Fratila *et al.* proposed a microfluidic chip design with two 32-turn micro planar spiral coils [85]. Each micro coil had a width and spacing of 20 µm, and an inner diameter of 250 µm. In the microfluidic channel beneath the coil, ca. 25 nL sample was measured by the coil. Recently, Christensen *et al.* presented a 30-coil receiver array that enabled simultaneous detection of 30 metabolic samples [86]. 10 PCB units were constructed, and each unit had 3 micro planar octagonal coils. This modular design is adaptable for applications such as drug-screening and metabolic disease modeling. A quasi volume micro spiral coil was introduced by Khelifa *et al.* as the scroll micro coil, as shown in Fig. 2.6 (g) [72]. It was reported to have an easier fabrication process and better B_1 field homogeneity than micro solenoids.

Stripline coil is a perfect candidate for miniaturization considering its simple structural adjustment and corresponding electromagnetic performance change. For a given length and area, a flat strip has less inductance than a round wire. This is important in high-frequency applications where stray inductances in the leads connecting different parts of the circuit must be minimized [17]. Micro striplines show low susceptibility broadening and high power handling capability. Van Bentum *et al.* provided a detailed performance comparison among micro stripline, solenoid and spiral coils, and constructed a micro stripline coil with a length of 1 mm and a cross section of $100 \times 10\ \mu m^2$ [87]. Q factors for the coil was between 80 and 100. The typical stripline geometry was further adjusted with tapered pads around the central strip to enhance the excitation efficiency and better confine the magnetic field along the stripline [88, 89, 90]. Considering the integration with microfluidic systems, the stripline geometry is naturally suitable for straight fluid channels or tubes and provides a high filling factor [63, 64, 91]. One successful device was a micro stripline chip proposed by Finch *et al.*, as shown in Fig. 2.6 (h) [73]. The micro stripline was connected to conductor pads symmetrically and covered by proper shielding planes for a higher magnitude of field concentration and better homogeneity at the stripline segment. The exchangeable microfluidic chip was sandwiched between two identical stripline boards. Micro stripline coils were suitable for application of in-situ NMR measurements of flow systems [64], and for monitoring real-time electrochemical reactions in batteries [92]. Tijssen *et al.* presented

an alternative stripline device with a varying stripline thickness. This tapered stripline coil was able to generate B_1 field gradients for spatially resolved spectroscopy based on the correlation between the conductor width and the field strength [74], as shown in Fig. 2.6 (i).

2.5.3 Micro coils in solid-state NMR

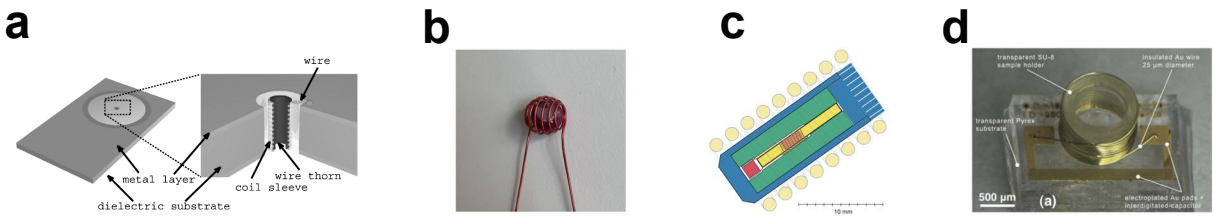

Figure 2.7: *Different micro coil designs for MAS NMR. (a) Micro solenoid MAS coil fabricated on a substrate (Reproduced from Ref. [93] with permission from Elsevier). (b) Spherical MAS coil (Reproduced from Ref. [94] with permission from Elsevier). (c) First magic-angle coil spinning (MACS) insert (Reproduced from Ref. [95] with permission from Springer Nature). (d) MACS insert with a wire-bonded solenoid (Reproduced from Ref. [96] with permission from PLOS).*

While the micro-coil designs discussed in the previous section were widely used for solution NMR spectroscopy to enhance the sensitivity, their application to solid-state NMR faces a few distinctive technical issues. To achieve high-resolution spectra with solid samples, the implementation of Magic-Angle Spinning (MAS) is an indispensable prerequisite. Along with the trend of rotor miniaturization, the RF coils are also down-scaled to realize high RF fields and sufficient filling factors [97]. Transitioning from static NMR probes to MAS-compatible systems requires the miniaturized coil to not only accommodate high-speed rotor assemblies but also to withstand mechanical vibrations during the detection. In addition, rotors are made of high-strength materials to withstand extreme centrifugal forces. Usually, the rotors are also sample holders and introduce permeability mismatching. Consequently, the following section focuses on the specialized development of micro coils for MAS NMR. There are two main categories: micro coils fixed on the stator, and micro coils embedded in the spinning rotor.

Yamauchi *et al.* reported a fixed micro coil measuring approximately 1 mm in length and 200 µm in diameter [93]. The coil was fixed onto a cylindrical holder with a Kel-F sleeve that provided good mechanical stability, as shown in Fig. 2.7 (a). Considering the construction space inside the MAS probe head, a plate capacitor made of gold-coated quartz was fabricated to tune the coil. The design was later verified on a MAS probe in 2006 [98, 99]. A micro sample holder fitting the coil was fabricated from Vespel and fixed on the back of a regular commercial 4 mm rotor. The micro solenoid coil was precisely aligned to the rotation axis. The generation of intense rf fields is critical for MAS NMR because the signals from solid samples are very broad lines. High rf efficiency in micro coils enables an even excitation in a wide band to capture the full structural information of the sample [100].

Chen *et al.* devised a spherical MAS rotor [94, 101]. Therefore, a spherical solenoid coil was manufactured to best accommodate the unique rotor shape. According to their study, this setup

showed better B_1 field homogeneity along the coil axis than the case of a cylindrical sample and a standard solenoid coil. The coil shown in Fig. 2.7 (b) has a macro size with a diameter of about 10 mm, but it shows that the coils in MAS NMR are partially determined by the rotor geometries. With further scaling-down of the sphere, micro spherical coils will naturally be employed.

Magic Angle Coil Spinning (MACS) was proposed by Sakellariou *et al.*, as shown in Fig. 2.7 (c) [95]. As its name indicates, the coil spins simultaneously with the rotor and transfers signals via inductive coupling to a second static coil. In the schematic diagram, the sample-containing cylinder (yellow) holds ca. 365 mg sample and is closely wound by a micro solenoid coil (bronze). The assembly was then inserted into a commercial 7 mm rotor (blue). Compared to the case with only a static coil, a higher filling factor was realized and signal sensitivity was magnified. What's more, fewer artifacts from the housing materials were introduced, and line-broadening was decreased.

Badilita *et al.* devised another MACS device by wire bonding and photolithography methods [96, 102, 103]. As displayed in Fig. 2.7 (d), a sample tube was manufactured through SU-8 lithography on a Pyrec substrate. A 13-turn solenoid was tightly wire-bonded to the tube. The coil had a diameter of 1 mm and a height of 650 µm. Furthermore, interdigitated capacitors were integrated on the chip substrate through gold deposition and realized coil tuning.

Besides the micro coil study, some researchers are working towards reliable and robust micro MAS probes as a complete solution to MAS NMR [104, 105]. The wire used to construct the coil was made from copper and aluminum to compensate for the magnetic susceptibility mismatch.

2.5.4 Simulation tool and design optimization

Throughout the development of various micro NMR coils, simulation tools are widely used for proper geometry design towards optimized figures of merits. Sometimes it is difficult to calculate analytically which parameters yield the maximum SNR considering the interaction of different dimension changes and the non-linear change of RF property changes due to the frequency-dependent skin effect and proximity effect [19]. Meanwhile, micro coils with compact samples usually demand a detailed evaluation of the material selections and interface changes, in order to avoid strong B_0 distortions and low spectral resolutions. In this section, several typical simulation tools or software are briefly summarized.

Advanced Design System (ADS) (Keysight Technologies Inc., CA, US) is one of the Electronic Design Automation (EDA) software, which specialize in designing, simulating, and verifying electronic systems. In the context of NMR coil design, it is usually employed for radio-frequency (RF) circuit simulation and impedance matching optimization. It generates electronic schematics for the equivalent model of the NMR coil. and further provides frequency-domain and time-domain circuit simulation. It is helpful in impedance matching optimization with tuning/matching adjustments in real time. It also allows for the simulation of physical electromagnetic layouts. By utilizing S-parameter analysis, the software enables precise extraction of the self resonance frequency and quality factor with defined coil dimensions and materials.

Finite Element Method (FEM) is a powerful numerical method to solve various problems in the analysis of mechanical stress, heat transfer, electromagnetic potential, and etc. COMSOL Multiphysics (COMSOL Inc., Cambridge, UK) is a popular FEM platform. With the RF module, COMSOL Multiphysics can be used to characterize 3D electromagnetic environment of an NMR detector. It enables full definition of materials properties and structural dimensions. The high-frequency RF field distribution (B_1) within a defined probe space can be visualized and quantified. In the simplest application, the software guides the optimization of single or multiple geometric parameters with respect to relevant figures of merit. More advanced applications are also accessible in COMSOL, including topology optimization [106]. MATLAB (MathWorks, Natick, MA, USA) can be used to control the software externally and post process the simulation results, e,g., excitation homogeneity and signal sensitivity. Additionally, coupled phenomena like RF-induced heating and static field distribution can be studied in parallel. FEM simulations with a high accuracy or coupled multiphysics can be demanding for computing power and simulation time. Therefore, highly efficiency modeling is helpful to accelerate the process, e.g., model order reduction [107].

Apart from the conventional optimization tools above, a Genetic Algorithm was developed by Tritrakarn *et al.* for optimizing NMR RF coil geometry towards a maximum signal intensity [108]. In the simulation model, the wire elements carrying current of a planar coil were represented by vectors, and a cylindrical sample was placed above the coil plane. The design was later fabricated and verified by FR-4 PCB. The detected signal intensity was increased by ca. 10% with the optimized geometry. The maximum error between simulation and experiment was reported as below 5%. This simulation method was proven to be fast convergent, reliable and versatile for different coils.

When more than one of these tools are used together, they form a robust design pipeline for researchers that ensures the structural integrity and electromagnetic performance of the microprobes prior to the fabrication phase. For instance, Terawatsakul *et al.* proposed a flowchart to evaluate the process of optimizing a micro NMR coil design with multiple tools, which was expected to fulfill multiple qualifications [109].

2.5.5 Microfabrication techniques for micro probes

For the various micro probe and coil geometries discussed above, a critical attribution to the miniaturization progress and the extended coil category is the advancement in high-precision fabrication techniques. The performance of the probe head is inherently limited by the capabilities of the fabrication process. Consequently, understanding the strengths and limitations of current micro-manufacturing technologies is essential. The following section provides an overview of the primary fabrication routes used to produce NMR micro coils and probes, evaluating how different techniques address the unique requirements of miniaturized NMR systems [110, 111].

Micro coil fabrication relies on accurate manipulation of the metal materials [78]. For solenoid and Helmholtz coils, manual operation of coil winding is widely utilized [93]. Therefore, a reliable

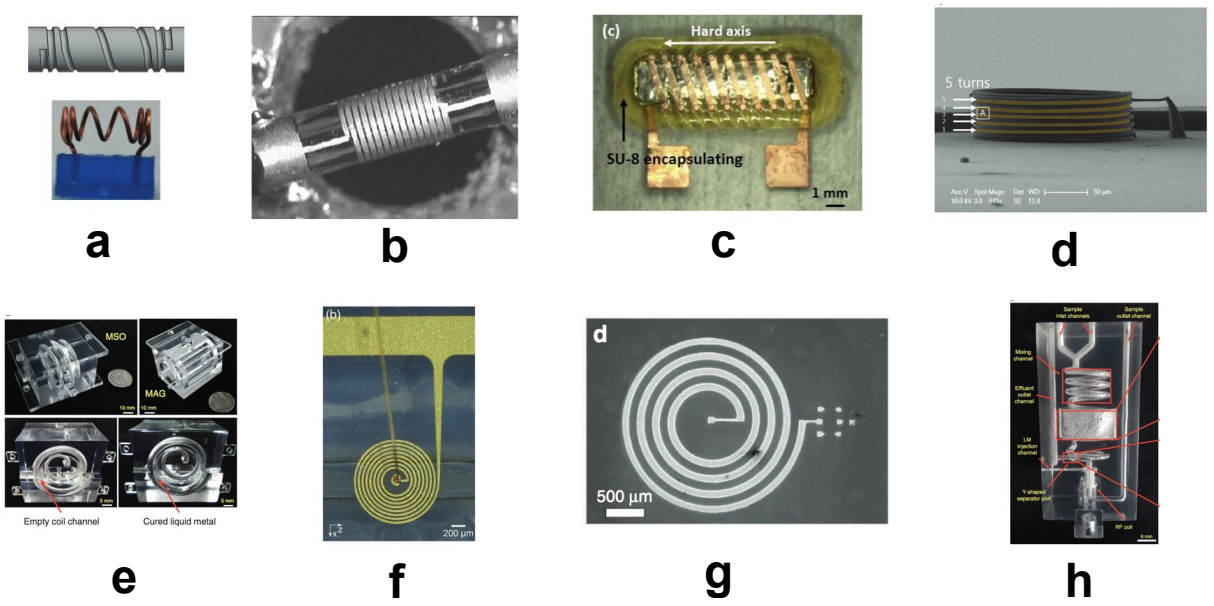

Figure 2.8: *Different fabrication methods of miniaturized NMR coils and probe components. (a) Solenoid coil fabricated by dissolvable form (Reproduced from Ref. [112] with permission from Elsevier). (b) Micro coil by laser-lathe lithography (Reproduced from Ref. [113] with permission from Springer Nature). (c) Solenoid micro inductor with nanolaminated core (Reproduced from Ref. [114] with permission from IOP). (d) Micro coil with the hybrid microstructure (Reproduced from Ref. [115] with permission from SAGE Publications). (e) and (h) Solenoid coil made from cured liquid metal, and 3D-printed continuous-flow flow separation probe head (Reproduced from Ref. [116] with permission from Springer Nature). (f) Electroplated spiral coil with a wire bonder (Reproduced from Ref. [84] with permission from Springer Nature). (g) Micro spiral coil on Si substrate (Reproduced from Ref. [117] with permission from Springer Nature).*

supporter or template is important to determine axial alignment and the pitch precisely. Some tricks were applied to wind solenoid coils easily and reproducibly. Kelz *et al.* devised dissolvable 3D-printed templates for highly reproducible coil winding [112]. As shown in Fig. 2.8 (a), a copper wire was wrapped in the notch printed on an ABS pillar and the pillar was later dissolved in acetone. It is noted that variable-pitch becomes possible with this method. As explained in Sec. 2.5.2, wire bonding has been verified to be effective in making extremely compact solenoid coils automatically [22, 67, 102]. This process is simple and precise with a low manufacturing cost. The substrate of the coil is usually compatible with other MEMS processes for circuits and micro fluidic structures.

Metal electroplating can generate ultra-thin metal layers, which can be micromachined in various ways for micro coils. The conductor for NMR coils should ideally be non-magnetic, and has a high excitation efficiency. Fig. 2.8 (b) presents a 3D direct-write lithographic technique to pattern typical volume coils on glass tubes, including solenoids and saddle coils [113]. On a tube with a Ti/Cu seed layer, a photoresist layer was applied conformly with a certain thickness depending on the required conductor thickness. The photoresist was then patterned by laser while the tube was rotated by a spindle. Copper was electroplated to form the coil around the tube with the assistance of the pattern. This method has high fabrication accuracy but low

efficiency. It was later employed to fabricate a group of RF, gradient, and shimming coils by Demas *et al.* [49]. Recently, Alaboz *et al.* proposed another method to fabricate 3D coils on glass tubes, [118]. The glass tube was evenly coated with copper layer. When it was rotated, laser cut out micro coils directly from the copper film.

3D surface micromachining typically involves photoresist-mold patterning, electroplating and sacrificial layer removal to construct one or multiple levels of conductors off a plane [28]. Its compatibility with batch fabrication provides a high throughput, but the coil geometry is limited to rectangular windings. A typical example is shown in Fig. 2.8 (c) by Kim *et al.*: a solenoid coil was segmented into vertical pillars and horizontal tracks, that were connected together [114]. Ha *et al.* proposed a detailed protocol for fabricating polymer/metal hybrid structures through two-photon stereolithography (TPS) with a dual-stage scanning [115]. The final product is shown in Fig. 2.8 (d). Polymer was micromachined on an SU-8 cylinder as an insulation layer. In the next step, silver was plated between the spacing pattern as the coil conductor.

LTCC technique can also be seen as 3D micromachining. Individual green tapes with different thicknesses can be patterned before the lamination and firing (around 900 °C °), which simplifies the design procedure and provides a great compatibility with cavity structures and most electronic elements [68]. Its high mechanical strength and resistance to high temperature high pressure makes LTCC technique ideal for manufacturing probe heads under extreme conditions.

Through-substrate-via (TSV) fabrication technique, as one of the advanced CMOS processes, was first developed as a packaging solution for the integration of multiple chips vertically and was adapted for micro spiral and solenoid coil fabrications in the mid 2000s [117]. It has developed an extensive toolbox with hole etching, dielectric insulator deposition, conductor deposition, substrate planarization and routing conductor patterning techniques.

Liquid metals with a low melting point were an alternative to solid coil wires [116]. 3D-printed probe heads were embedded with empty coil channels, which were filled with liquid metals, as shown in Fig. 2.8 (e). The liquid metal was connected to copper strips and sealed with silver to function as an RF coil. 3D printing promises the potential for constructing various complicated coil geometries with micrometer precision. This approach depends on the manufacturability of 3D-printing and the selection of liquid metals.

Vanduffel *et al.* proposed a metallic 3D-printing solution to make NMR coils, where the laser beam selectively melted and consolidated copper powder in a bed [119]. The coil was built layer-by-layer, and the dimensional precision was greatly affected by the powder size [120].

Micro planar NMR coils benefit greatly from 2D surface machining in MEMS field since the early 1990s [39, 78]. It provides a wide selection of building materials and good compatibility with integrated circuits and fluidic systems. Fig. 2.8 (f) shows a typical electroplated spiral on a glass substrate with the help of SU-8 photolithography process [84]. Mechanical features like cavities were cut by laser on the glass layer. Fig. 2.8 (g) shows another spiral coil device with ultra-high resolution [117]. The planar coils can also be suspended above the substrate. With the assistance of sacrificial layers or under-etching, Xi *et al.* showed the coil windings to be

isolated from the glass substrate so that parasitic capacitance is decreased [121]. Additionally, A series of studies focusing on micro planar coil fabrication using CMOS technology have been reported in the last two decades [48, 69, 122, 123].

Self-assembly technique is a unique tool to fabricate coils in a 2D manner and to further arrange them into 3D functional devices. Oppositely strained SiN_x bilayers were used as the driving force for a controlled self-rolling-up of the conducting metal strips [124]. Compared to the 2D or 3D micromaching methods, it is advantageous for fabricating complex coil structures without the need for excessive multilayer processing.

Apart from the micro coils, other probe components involve advanced fabrication methods as well, especially integrated microfluidic systems and mechanical probe structures [125, 126, 127]. High-precision 3D printing at µm resolution plays an important role in making microfluidic systems. It is cost effective and time efficient for lab use, considering the affordable prices of filament or resin 3D printers and the related consumables. A wide variety of polymer materials can be employed for 3D printing, which gives rise to novel applications. In the project by Boero *et al.* [126], to work with the micro coil produced by the 130 nm CMOS process, the microfluidic structures were fabricated using the two-photon polymerization 3D printing. Fig. 2.8 (h) presents a complete probe head with a complicated continuous-flow sample processing system fabricated by fused deposition modeling and stereolithography [116].

2.6 Multi-resonance and broadband NMR

As the scope of NMR applications continues to extend, there is an increasing demand for an NMR probe capable of multi-nuclear detection across a wide spectral range. Transitioning from single-nucleus probes to multi-nuclear probes offers significant advantages. In the first place, it enhances experimental throughput by minimizing the need for frequent hardware reconfigurations. It also cuts down the expense over redundant probe hardware. More importantly, it enables 2D NMR experiments, especially heteronuclear correlations. The 2D NMR techniques provide indispensable insights into molecular structures and reaction dynamics that are inaccessible through 1D measurements.

To achieve multi-nuclear capabilities, two primary hardware strategies have emerged. The first relies on multi-resonance circuits, which employ intricate tuning and matching networks to operate at a few discrete frequencies. In contrast, the second approach utilizes non-tuned NMR detectors, which facilitate data acquisition across a broad frequency band. While the former prioritizes sensitivity at specific resonances, the latter emphasizes bandwidth and operational flexibility. The following sections present the theoretical foundations and implementation challenges of these two distinct design approaches.

2.6.1 Multi-resonance circuit

As discussed in the preceding Sec. 2.4.3, an NMR probe conventionally employs a tuned resonance circuit with impedance matching for optimal signal transmission and reception. Traditionally, multi-nuclear detection in NMR probes is achieved through tuned multi-resonance circuits. The fundamental architecture relies on the integration of frequency-selective networks, such as LC traps. The design has progressed from standard double-resonance (normally $^1\mathrm{H} - \mathrm{X}$) configurations to sophisticated triple-resonance (normally $^1\mathrm{H} - \mathrm{X} - \mathrm{Y}$), and even broadband-tunable designs [128].

Lumped-element circuit

A big category of multi-resonance circuit designs utilize only lumped elements, i.e., capacitors and inductors [79, 129, 130]. Two major network topologies are applied in such circuit design, trap circuit and tank circuit, which are simulated and reviewed in detail in a recent work [128].

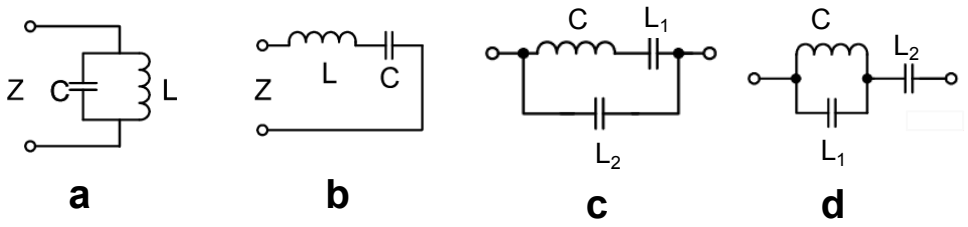

Figure 2.9: *Basics of trap and tank circuits. (a) A parallel LC trap. (b) A series LC trap. (c) and (d) tank circuits (Reproduced from Ref. [128] with permission from Elsevier).*

RF traps can guide or suppress signals for different frequencies within the circuit. Based on its frequency-dependent electrical properties, a trap circuit can act as an open circuit due to a high impedance at one frequency but a short circuit due to a low impedance at a second frequency. When the trap circuit design is fixed, the placement of this trap also determines how it performs in the whole circuit, e.g., between two signal nodes or between a signal node and ground. Two types of LC trap circuits are commonly used, parallel LC traps and series LC traps.

A parallel LC trap is illustrated in Fig. 2.9 (a). Its port impedance $Z = L(RC)^{-1}$ is very high at its resonance frequency $f_r = 1/\left(2\pi(LC)^{1/2}\right)$, neglecting the parasitic resistance from the inductor. When such a trap shunts a node to ground, it behaves as a band-stop filter, strongly suppressing signals at f_r. Conversely, when a parallel LC trap is inserted in series between two ports, it functions as a band-pass filter, allowing signals near f_r to pass through. Figure 2.9 (b) shows a series LC trap, which exhibits a low purely resistive impedance at the resonance frequency f_r. Owing to this complementary behavior, a series LC resonator acts as a band-pass filter when placed between two nodes, while it functions as a band-stop filter when used to shunt a node to ground. In both cases, the frequency selectivity is determined by the quality factor of the inductor. There is flexibility in topology design with various combinations of these two circuit blocks. For a new design, a detailed analysis of frequency-selective isolation or transmission efficiency, noise performance, and related metrics should be carried out using circuit simulation software such as Advanced Design System.

An RF tank is another LC network which has a self-resonance frequency and works as either a capacitive or inductive element at other frequencies. At its resonance, it cuts off the signal path due to a high impedance. This circuit can be used as a variable capacitor/inductor component for tuning and/or matching. Therefore, it adds additional detection frequencies to a resonating sample coil. Two common RF tank circuits are displayed in Fig. 2.9 (c) and (d). Multi-resonance circuit designs based on tank circuits are considerably more complex than those employing trap circuits. Since the tank circuit does not act as a short or open circuit at working frequencies, the isolation between different channels is impossible, which further constrains the application of tank circuits [131].

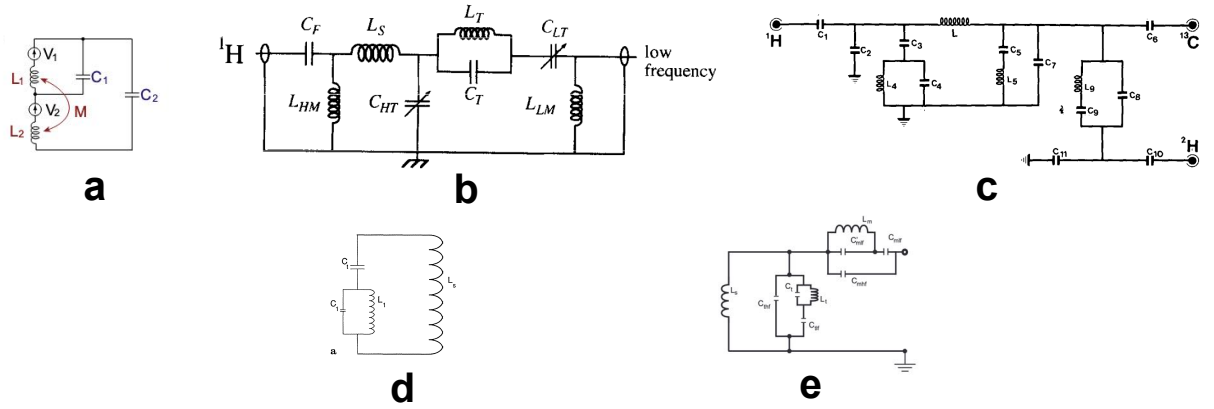

Figure 2.10: *Different multi-resonance circuit topologies. (a) Circuit diagram of a double-resonance MACS (Reproduced from Ref. [132] with permission from Elsevier). (b) Double-resonance circuit (Reproduced from Ref. [130] with permission from Elsevier). (c) Double-resonance circuit (Reproduced from Ref. [133] with permission from AIP Publishing). (d) Multiple-pole double-resonance circuit model (Reproduced from Ref. [129] with permission from Springer Nature). (e) Single-channel double-resonance coil (Reproduced from Ref. [134] with permission from Elsevier.)*

In practice, these circuit blocks are applied in various topologies for constructing multi-resonance probes. A most straightforward approach to multinuclear detection utilizes multiple coils, where each frequency is assigned to a single coil. Collins *et al.* presented such a double-coil design taking full advantage of the MEMS process for micro coils [135]. Two coils can be arranged in an orthogonal geometry and thus be intrinsically decoupled. Apart from the geometrical design, these two micro coils were further isolated with the tuning and matching circuit. Inukai and Takeda proposed another two-coil double resonance detector in MACS NMR [132]. The electrical model is shown in Fig. 2.10 (a). L_1 and L_2 represent two solenoid coils wound on a same sample tube. By solving the equation of the circuit, two resonance frequencies are realized. While this method simplifies tuning for individual nuclei, it is severely limited by the restricted space in the magnet bore and the challenges of coupling between coils. Additionally, different coils have different regions of interest and it is hard to optimize the filling factor of all coils.

Another solution is multiple resonance with a single coil. A typical configuration is multiple output/channels being connected to the individual coil and facilitate simultaneous heteronuclear

detections as well as respective signal processing through each channel. There is also the possibility of using a single output port with the tuning and matching circuit for different frequencies at this port. An example of the former case is shown in Fig. 2.10 (b) by Harbison *et al.*, where L_s stands for the sample coil, components with subscript H are for the high-frequency channel and subscript L for the low-frequency channel [130]. A distinctive feature of this design is the use of the high-frequency tuning capacitor C_{HT} to create a virtual ground, thereby suppressing cross-talk between two channels. Fig. 2.10 (c) displays a triple-channel probe by Kan **et al.** [133], in which $^{1}\mathrm{H}-^{13}\mathrm{C}$ measurement with a deuterium frequency lock was implemented. Based on a triple-tuned solenoid coil, Collier *et al.* also designed a quadruple-resonance probe (^{1}H, ^{13}C, ^{2}H, ^{14}N) with up to 10 capacitors composed of transmission line segments in the circuit [34].

As for the latter case with a single channel, tank circuits are employed to match the coil impedance at two or more frequencies simultaneously. Schnall proposed a single-channel design with two resonance frequencies, as shown in Fig. 2.10 (d) [129]. A single carrier frequency can be split into two detection frequencies with the tuning and matching circuit, corresponding to $^{1}\mathrm{H}$ and $^{13}\mathrm{C}$ signals in the sample. It is important to have precise calculations of the LC component values for this circuit to perform properly, taking the sample inductance into consideration. A slightly different approach is the topology shown in Fig. 2.10 (e), in which two resonance frequencies were governed by sophisticated tank and trap circuits with 2 inductors and 6 capacitors in total [134]. A parallel LC tank was connected to the sample coil, which isolated the high-frequency circuit from the low-frequency channel. The probe resonated at 510 kHz and 128 kHz respectively for $^{1}\mathrm{H}$ and $^{13}\mathrm{C}$ measurements. Considering an inherently lower sensitivity at 128 kHz than that at 510 kHz, the relative design efficiency in this design was biased to the low frequency channel in order to compensate for the sensitivity. Achieving three or more resonances within a single coil requires more complex circuit constructs, i.e., the combination of differential mode and common mode trap circuits [128]. Compared to the multi-channel approach, it is generally more challenging to add extra detection frequencies in the single-channel configuration.

Transmission line network

Transmission lines, including coaxial cables, microstrip transmission lines, and microwave waveguides, can be used to realize tuning/matching and channel isolation, serving the same function as LC trap circuits [34, 128]. The characteristic impedance of a transmission line, Z_0, is determined by its geometry and materials. Unlike lumped components, the capacitance and inductance are distributed along the transmission line. The capacitance of a transmission line per unit length depends on the diameter ratio of the outer and center conductors and on the dielectric constant of the insulating material [17]. A transmission line can be incorporated into the circuit with a length between 0 and $\lambda/2$, allowing a wide range of reactance values to be realized. As the transverse electromagnetic (TEM) wave propagates along the transmission line, forward and reflected standing waves are formed and must be considered in the design.

Transmission lines may be configured as open-ended or short-ended sections, as illustrated in Fig. 2.11 (a) and (b). The operating frequency for each configuration is selected by adjusting

the line length. For an open-ended transmission line, the cable end is left unconnected and thus presents an effectively infinite load impedance. A half-wavelength segment presents a very high input impedance, whereas a quarter-wavelength segment presents a low input impedance. Conversely, for a short-ended transmission line, the inner conductor is physically connected to the outer shield to produce an ideal zero load impedance. In such case, a quarter-wavelength line yields a high input impedance, whereas a half-wavelength section results in a low input impedance. Although a transmission line can perform the same function as a lumped-element LC trap, its implementation in an NMR probe differs fundamentally in terms of construction and integration. It is noted that for low-frequency resonances, the required transmission line length might exceed the spatial constraints of the probe. In addition, power dissipation in long transmission lines introduces additional signal loss and contributes extra noise to the probe.

Fig. 2.11 (c) shows a single-coil triple-resonance probe ($^{2}\mathrm{H}-^{13}\mathrm{C}-^{15}\mathrm{N}$) with transmission line components [34]. The coaxial elements were distributed over the length of the probe to make efficient use of the available volume. This approach could be further extended to a quadruple-resonance probe. However, the 2-inch-diameter bore already imposes severe spatial constraints on the implementation of all components required for a quadruple-resonance design.

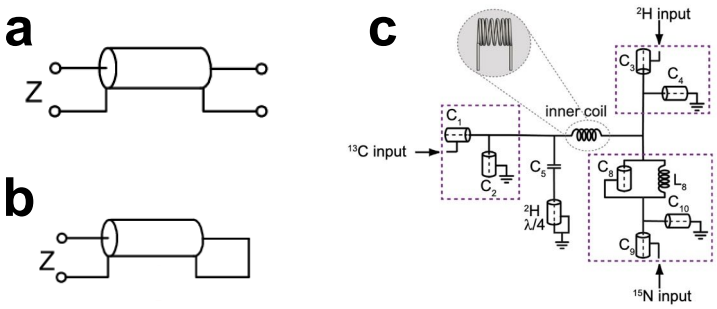

Figure 2.11: *Two different transmission line configurations. (a) open-ended transmission line. (b) short-ended transmission line. And (c) Triple-tuned solenoid with transmission lines (Reproduced from Ref. [34] with permission from Elsevier).*

Despite the significant progress in multi-resonance designs, the increased number of passive elements in micro-coil applications raises circuit complexity and difficulty of manual tuning. It further degrades power efficiency due to parasitic effects and cross-talk between channels, which leads to the exploration of alternative broadband designs with minimal number of components.

2.6.2 Non-tuned broadband coils

In contrast to the multi-resonance circuits discussed in the previous section, non-tuned coils are directly connected to the transceiver circuit and utilize signals over a wide frequency range without the need for manual re-tuning. It could circumvent the design complexity in the tuning circuit and limited operating frequencies, resulting in a universal detection platform capable of acquiring signals across a wide band. This provides an ideal solution for metabolomics, enabling instantaneous multi-nuclear screening of fragile, time-sensitive biological specimens without hardware

reconfiguration. Additionally, non-resonant broadband approach offers an inherent robustness against environmental shifts, e.g., unstable static field or material transitions in the sample.

In miniaturized systems, the broadband strategy with non-tuned coils becomes exceptionally effective due to the electromagnetic properties of micro-coils discussed in Sec. 2.5.2. A micro coil has a flat impedance change close to its DC value within a wide frequency band. Meanwhile, micro coils usually possess very high self-resonance frequencies. In practice, the upper limit of the detection band is suggested be lower than one quarter of the self-resonance frequency of the micro coil [136]. In the excitation mode, the currents passing from the coaxial cable into the micro spiral with a small resistor value remain sufficient [38]. Therefore, the RF pulse is able to induce the oscillating magnetic field around the sample in a broad band. According to the reciprocity theorem, once a reasonable value of B_1 is produced, a low-impedance micro coil can always drive a 50 Ω load from the cable and has a good reception efficiency. Under such circumstances, the impedance matching is intentionally compromised in favor of a much larger operational bandwidth, which results in unoptimized yet relatively flat detection sensitivity across a wide frequency range. For micro-scale samples where volume is at a premium, the broadband micro-coil eliminates the need for complex trap circuits that typically degrade the filling factor in multi-tuned designs.

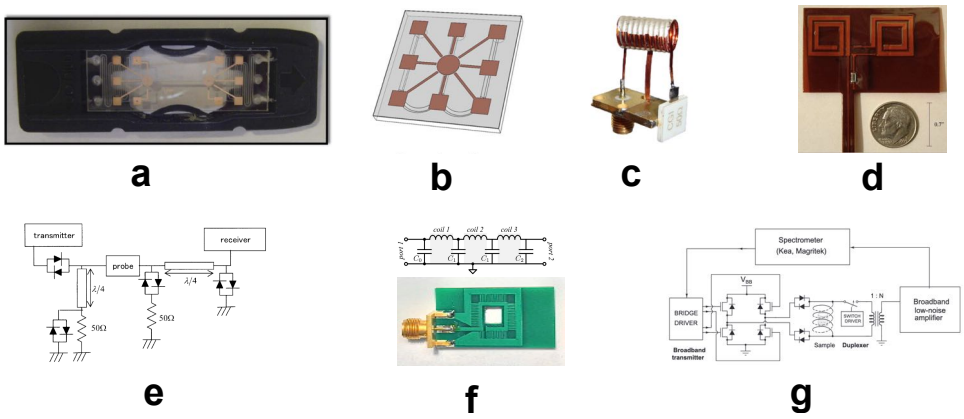

Figure 2.12: *Various non-tuned NMR coils (a-d) and non-tuned circuit topologies (e-g). (a) Microfluidic non-tuned NMR chip (Reproduced from Ref. [85] with permission from Springer Nature). (b) Planar spiral coil (Reproduced from Ref. [137] with permission from Springer Nature). (c) Solenoid-shape transmission line probe (Reproduced from Ref. [138] with permission from Elsevier). (d) Non-tuned saddle coil based on flexible PCB (Reproduced from Ref. [139] with permission from Elsevier). (e) Non-tuned circuit configuration using transmission lines and diodes (Reproduced from Ref. [140] with permission from Elsevier). (f) Circuit for lumped-element delay line probe (Reproduced from Ref. [141] with permission from Elsevier). (g) Block diagram of the broadband MR system, corresponding to Fig. 2.5 (b) (Reproduced from Ref. [50] with permission from Elsevier).*

A series of studies has demonstrated the potential of non-tuned micro spiral coils. A micro quasi-spiral coil was fabricated on a CMOS board and had a diameter of around 150 µm [52]. It worked at up to 300 MHz and was matched with a large resistance of 20 kΩ to decrease the noise at low frequencies. Davoodi *et al.* presented a micro planar spiral coil and the full microfabrication

process based on a glass wafer [84]. To compensate for the resolution loss and spectral distortions of the planar coil over a wide frequency range, finite element analysis was applied to optimize the coil dimensions and reduce the magnetic susceptibility mismatches. The detector chip was directly connected to the preamplifier via a coaxial cable without tuning and matching circuits. It covered a frequency range from 126 MHz to 501 MHz for measuring 7 different nuclei.

Fratila *et al.* reported another non-tuned non-matched micro spiral coil based on glass, as shown in Fig. 2.12 (a) [85]. The micro spiral coils were employed in 1D and 2D NMR measurements from 61 MHz to 400 MHz, spanning the detection range from ^{15}N to ^{1}H. Since there was only one coaxial cable connected to the coil, a combiner was used to connect the transmitter and decoupler outputs to the micro coil. Another non-tuned spiral coil is displayed in the center of Fig. 2.12 (b) as a copper disc [137]. In order to realize a triple-resonance probe with this single-channel coil, two combiners and three filters were used in the front-end circuit to guide the signal of each frequency. In these experiments, the micro spiral coils provided comparable sensitivity to tuned and matched coils, showing its potential in molecular structure analysis and metabolomic NMR.

Transmission line components can also serve as NMR coils and work without being tuned [17, 142, 143]. The transmission line coil is constructed from one or a series of conducting strips isolated from a grounded plane with a dielectric layer. With its distributed capacitance and inductance, the device can be seen as a low-pass filter. Each strip section consists of either an inductor and two capacitors (π-type low-pass filter) or two inductors and a capacitor (T-type low-pass filter). A key parameter of the transmission line coil is the cut-off frequency determined by the strip section, below which the coil presents a flat impedance response over a wide band. Generally speaking, smaller L and C mean a higher cut-off frequency and a larger probe bandwidth, but a smaller portion of energy stored in the coil.

Fig. 2.12 (c) presents a non-tuned transmission line probe made of a solenoid coil [138]. The solenoid was wound with copper wire and then covered with epoxy resin as the dielectric. The outer surface of the coil was then covered with conducting material and connected to the ground. The conducting paint was applied in a way that it matches the whole coil to 50 Ω. The coil was connected to the transmitter at one port and to a 50 Ω resistor at the other port. This resistor made the coil non-resonant instead of forming a quarter-wave resonator. It worked within 15 MHz bandwidth at a center frequency of 217 MHz. Another transmission line coil was designed in a saddle coil geometry by Murphree *et al.* [139]. Fig. 2.12 (d) shows the unfolded saddle coil fabricated on a flexible PCB. The probe was tested at around 20 MHz though it could work up to 150 MHz. It is worth noting that the RF field strength decreased as the frequency increased, since a higher impedance mismatch led to more signal reflection. However, as a signal path within the circuit, the power transfer efficiency of a transmission line coil is low compared to a pre-tuned circuit. The utilization of high-speed active T/R switches and low-noise differential amplifiers can increase the reception sensitivity in transmission line probes[144]. Compared to resonant detectors, the transmission line probe requires a larger input power for a sufficient pulse length and is up to an order of magnitude less sensitive than common resonant probes.

The transmission line coil was actually built on the concept of delay line coils. Delay line coils were first developed and named by Lowe and Engelsberg, which principally employed discrete lumped capacitors and inductors instead of distributed impedance. Similarly, a delay line coil can be seen as a low-pass filter below a cut-off frequency. Kubo and Ichikawa provided a detailed analysis model and circuit configuration of the delay line probe, the latter of which is shown in Fig. 2.12 (e) [140]. The coil can be modeled as N cascaded T-networks, in which each section has $1/N$ of the coil inductance L and a capacitance C to the ground. The cut-off frequency is calculated as $\omega_c = \sqrt{4N/(LC)}$. The coil impedance follows $Z = \sqrt{L/(NC)}$. Scharfetter *et al.* introduced a different delay line probe constructed with a sample coil and a group of lumped inductors in series [145]. The probe operated within 50 MHz at a center frequency of 122 MHz.

Evetts proposed an unmatched delay line probe design [141]. The bare coil was fabricated on PCB and is shown in Fig. 2.12 (f). The interdigitated electrodes form multiple distributed LC units rather than a lumped LC network. As a result, this structure resembles a transmission line probe more closely than a delay line probe, despite the author's original designation. The units determine the cut-off frequency and quality factor of the coil. It has a measurement range of 4 MHz to 400 MHz. The unmatched delay line probe generated a higher current in the coil, and therefore a stronger RF field. The primary challenge in delay-line probe design is minimizing parasitic effects and signal losses from the interconnection of a large number of components. In addition, the presence of extra inductors that are not coupled to the sample leads to a reduction in probe efficiency. In comparison to the delay line probe, transmission line probe exhibits a better field homogeneity thanks to its compatibility with microfabrication techniques.

An emerging trend in non-tuned coil development is the digital control of the resonance frequency shift and bandwidth sweeping by integrated circuits. A digitally-controlled tuned receiver was used together with a non-tuned transmitter aimed at low-frequency NMR applications by Hopper *et al.* [146]. At low frequencies, the power reflection from the cable is insignificant since the wavelength is much larger than the sizes of the used circuit components. On the other hand, the low-inductance non-resonant coil presents great power transfer efficiency and adequate current for RF excitation when the transmitter is designed with a low output impedance. In the design, RF switches replaced tuning or matching capacitors in the transmitter network. It was also pointed out that the circuit built with a non-resonant coil (low quality factor) would be less sensitive to environmental factors, i.e., temperature.

Mandal *et al.* developed an ultra-broadband system with a non-tuned solenoid coil within 0.1 MHz to 3 MHz, as shown in Fig. 2.12 (g) [50]. By integrating a low-noise amplifier directly with the coil, they minimized the noise figure and successfully avoided the power reflections typically associated with impedance mismatch. A specific RF waveform was synthesized and controls the current in the micro coil to drive the spin excitation directly. The electronics also detect the signal current induced in the coil so that the reception is calibrated automatically.

In the work mentioned above by Grisi *et al.* [52], the micro coil was also driven by a unique transmitter network. The matching network used reversed biased diodes as voltage controlled capacitors though there was power dissipation in the diodes during signal transmission. In this

particular case, a non-resonant coil with a smaller Q was preferred since a smaller voltage signal was required for the coil, and the power dissipation decreased in the diodes. In addition, the transmitter and receiver were controlled and isolated with switches, which realized an isolation of higher than 50 dB. Both channels worked in a frequency range of 1 MHz to 1000 MHz. In recent years, a TX/RX switch based on PIN-diode was also explored as the front-end for the broadband coil by Xu *et al.* [147].

These active NMR detectors with customized circuits provide extended design flexibility for high power transmission and sensitive reception systems. Owing to their wider bandwidth and shorter dead times, such designs have the potential to significantly enhance system performance across a broad range of NMR applications.

2.6.3 Trade-offs with broadband detectors

The high frequency selectivity of a tuned NMR probe acts as a double-edged sword. While a high Quality factor maximizes sensitivity at a specific resonance, the resulting narrow bandwidth (see Eq. 2.16) renders the system inherently fragile to frequency mismatches.

The intrinsic lineshape of an NMR signal is determined by the relaxation processes, typically Lorentzian in liquids, or Gaussian in solids/inhomogeneous fields. In this work, the normalized signal amplitude A can be expressed with the Lorentzian distribution mathematically:

$$A(\omega) = \frac{1}{1 + Q^2 \left(\frac{\omega - \omega_0}{\omega_0}\right)^2}. \tag{2.22}$$

When the probe with a high-Q coil (e.g., Q>100) is perfectly matched and tuned, the power transfer is maximized. However, even a minor frequency error or drift results in a sharp increase in reflected power and a concomitant degradation of the signal phase and amplitude, thereby a drastic SNR reduction.

This inherent frequency selectivity creates a critical trade-off between sensitivity and versatility. In conventional NMR, the pursuit of maximum SNR through high-Q resonant circuits requires complex, bulky, and expensive hardware for each target nucleus. In contrast, a non-tuned broadband approach deliberately sacrifices this resonant gain to achieve a flat frequency response. While this results in a reduction in raw SNR at a specific frequency, it eliminates the sensitivity to frequency errors and enables the simultaneous or rapid sequential detection of multiple isotopes without manual intervention or hardware reconfiguration. This trade-off is particularly advantageous for broadband detectors in micro-scale NMR and constrained environments. By optimizing the filling factor, coil geometry and reducing parasitic effects at the micro-scale, the practical gap in SNR can be significantly narrowed, making broadband detection not only a viable but a superior solution for multi-nuclear analysis.

The practical superiority of non-resonant approach can be best demonstrated through several emerging applications where the operational flexibility and the broad-spectrum acquisition of broadband detectors overcome the fundamental physical limitations of conventional resonant hardware. The integration of NMR spectroscopy with X-ray spectroscopy, especially synchrotron,

represents a frontier in multidisciplinary instrumentation [148]. It can provide valuable information by capturing rapid transient processes where multiple nuclei are monitored near-simultaneously during X-ray acquisition. In high-flux environments, the NMR detector must operate within a limited spatial space, which is shared with X-ray optics, electrochemical cells, or cryostats. Under these conditions, the inclusion of bulky variable capacitors for tuning and matching is physically prohibitive. In addition, switching detection frequencies via manual tuning operation under stringent time constraints is nearly impossible. The engineering challenge here shifts from maximizing peak SNR to optimizing the sample holder and resonator geometry to survive the electromagnetic interference and radiation-rich high-temperature environment of the beamline. With the growth in portable electronic device, the development of advanced electrode materials becomes important. The study during battery charge-discharge cycles presents a unique challenge that the bulk magnetic susceptibility of the electrode material changes dynamically as ions intercalate. In resonant NMR systems, these changes cause significant de-tuning, leading to signal loss or artifacts. The development of broadband detectors also paves the way for stable, long-term operando monitoring of energy storage systems.

Chapter 3

Broadband stripline Lenz lens

The contents of this chapter are based on the author's contribution to the material published in the article [J1]. **Materials from: Liang, Jianyi *et al.*, Broadband stripline Lenz lens achieves 11× NMR signal enhancement, Scientific Reports, published in 2023, Springer Nature**

This chapter provides a comprehensive study on the development of a broadband NMR detector based on the stripline and Lenz lens. It covers the entire process, from the initial conception and design, the optimization and manufacturing, to the characterization and final NMR/MRI measurements. Several important aspects are addressed in this chapter. First, it analyzes the new variant of broadband detectors with solid electromagnetic simulations of the combined stripline and Lenz lens structure. Second, a complete fabrication workflow for the glass wafer-based NMR detector fabrication in the clean room is outlined, including the challenges encountered including etching and bonding multiple layers. Third, we show the implementation of this broadband detector as an add-on device for a commercial probe, and the protocol for multinuclear measurements as well as for HSQC measurement.

3.1 Introduction

As a non-invasive and non-destructive analytic technique, NMR reveals an exquisitely detailed inner picture for a wide range of materials, providing insight into their structures and dynamics with atomic level resolution. NMR also suffers from low sensitivity. In a field of 11.74 T, roughly only 1 in about 100000 identical spins contributes to the total detected NMR signal.

As introduced in the previous chapter **Background Information**, miniaturized NMR detectors are advantageous when the amount of sample is limited, and arise in numerous practical situations, such as working with toxic, expensive, or otherwise limited-availability samples, or the necessity to perform a large number of experiments and reduce the associated waste. The smallest possible NMR detector that fully contains the sample to be analyzed, leads to the highest achievable SNR [66].

Yet the miniaturization of NMR detectors also poses a series of challenges [149]. Usually, miniaturization implies a dense arrangement of constituent materials in a very limited volume, e.g., metals for the detector itself, glass and/or polymers as substrate and sample holder, as well as the sample itself. The materials may exhibit very different magnetic susceptibilities, which lead to B_0 non-uniformities degrading both spectral resolution and SNR. B_1 uniformity in the limited sensitive volume of a miniaturized NMR detector requires precise RF field optimization. Sample handling at small length scales poses its own specific challenges as well.

Among numerous variants of miniaturized detectors reported in the literature, striplines have checked a number of boxes on the list of challenges brought by miniaturization: affordable fabrication that allows for batch manufacturing; their slender predominant dimension can be easily aligned to the static field, thus not only inherently creating a B_1 field perpendicular to the static field, but also minimizing the B_0 jumps and offering an intrinsically good spectral resolution. Even early approaches have reported sensitivities better than $0.5\,\mathrm{nmol}/\sqrt{\mathrm{Hz}}$, B_1 homogeneity (A_{810}/A_{90}) better than 76%, and sub-Hz spectral resolution [73, 87, 88]. Stripline NMR detectors have demonstrated their versatility in handling both liquid and planar thin film samples, being employed for in-situ NMR monitoring of chemical reactions [63] or metabolomic analysis [150, 151], continuous flow measurements with flow rates between $0.55\,\mu\mathrm{L/min}$ and $15\,\mu\mathrm{L/min}$ [64], as well as together with generic DNP enhancement in the solid state demonstrating solid-state ^{1}H enhancement factors of up to 500 for $H_2O/D_2O/d_6$-glycerol samples doped with TEMPOL radicals [152].

Remarkably, the beautifully simple structure of stripline detectors has proven to be amenable to integration with a series of add-ons, offering additional capabilities: a tapered stripline structure is generating arbitrarily-defined one dimensional B_1 gradients enabling spatially resolved spectroscopy even in inhomogeneous static fields [74], or acting as a simple and cheap alternative to B_0 pulsed filed gradients [153]. An innovative combination between a stripline (for detection) and a flattened solenoid-like coil (for transmission) was employed to demonstrate novel differential-mode NMR measurements [154].

In this chapter, borrowing from another branch of miniaturized NMR detectors, i.e., the Lenz lens, a stripline is developed that is wirelessly connected to the rest of the hardware. Lenz lenses have been previously described as a method to manipulate the magnetic flux distribution by controlling the induced currents in passive elements [155], eventually being studied, optimized and introduced in the design of NMR detectors [23, 25, 156, 157]. Lenz lens structures collect and concentrate the magnetic flux in a certain volume and are intrinsically broadband [128]. By integrating the stripline detector with the Lenz lens add-on in a novel structure called stripline Lenz lens (**S3L**), the following features are demonstrated: (1) Inductive coupling to custom-made saddle coils tuned for various Larmor frequencies. (2) Broadband operation covering the frequency range from ^{13}C to the proton in an 11.74 T NMR scanner (roughly between 125.76 MHz to 500 MHz). This is demonstrated as a proof of concept, however, the S3L structure is able to cover a much broader bandwidth. (3) Up to one order of magnitude NMR signal-to-noise enhancement measured at 500 MHz. (4) Cancellation of the B_1-field outside of the focal region

by the Lenz effect, leading to precise localization of the NMR excitation. (5) Manipulation of the B_1-field orientation with a 90° phase difference. The stripline Lenz lens rotates B_1 by 90° with respect to the driving RF field generated by the saddle coil. This is also useful for applications such as battery structures with driving electrodes, or thin film samples, which then avoids the excitation of unwanted sample regions.

3.2 Experimental set-up

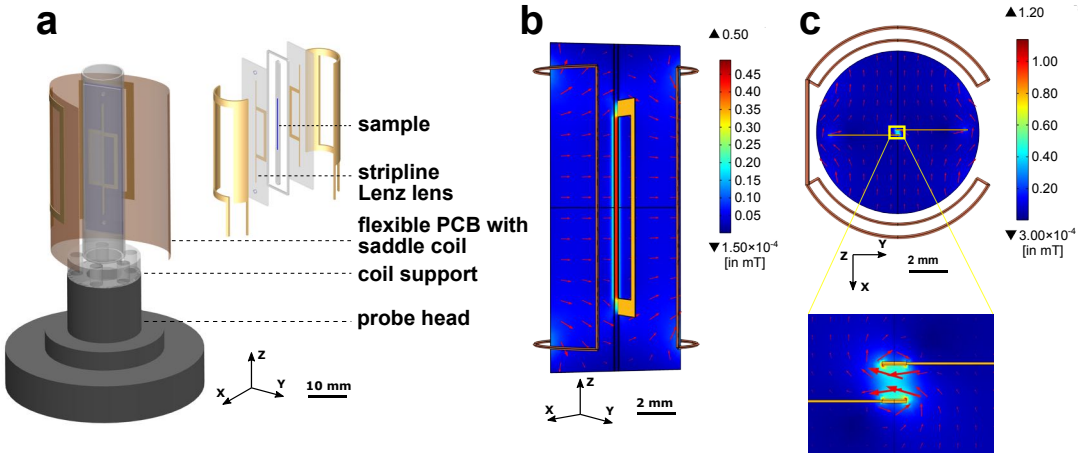

Figure 3.1: *Configuration of stripline Lenz lens chip on an NMR probe-head, and its magnetic field distribution. (a) Illustration of the coil system with a saddle coil and an S3L chip mounted on the probe head. Exploded view of the coils, with the sample region shaded blue. (b) B_1-field distribution on the XZ-plane via a color map and an arrow surface plot. (c) B_1-field distribution on the XY-plane and a zoom-in view around the stripline. Reproduced from the author's own publication **J1** with the permission from Springer Nature.*

Fig. 3.1 (a) shows the measurement probe head, including the stripline Lenz lens (S3L) insert and the custom-made saddle coil. The S3L structure consists of two striplines running parallel to the main axis of the magnet Z-axis, i.e., along the direction of the static magnetic field B_0. Each stripline is connected to a rectangular loop located symmetrically on either side of the main axis. The plane of each loop is oriented perpendicular to the B_1 field generated by the saddle coil. As a result, each loop acts as a Lenz lens. It intercepts the incident RF magnetic field over the loop-defined area, $B_{1,\mathrm{s}}$, and converts it into an induced current flowing along the metallic loop conductor. This current, in turn, generates a secondary RF magnetic field in the vicinity of the metal track.

Because the stripline forms an integral part of the Lenz lens loop, the narrow sample region confined between the two striplines experiences the superposition of the RF magnetic fields generated by the two loops, denoted as $B_{1,\mathrm{S3L}}$, as illustrated in Fig. 3.1 (b). In addition, the Lenz lens geometry modifies the orientation of the incident RF field, effectively rotating it by 90°, as shown in the inset of Fig. 3.1 (c). The stripline elements extend beyond the loop insertion points to ensure material continuity and magnetic susceptibility uniformity along the Z-axis (see Sec. 3.4.3).

The saddle coil was fabricated using a flexible PCB–based manufacturing approach, which enabled rapid design and fabrication of transmit coils optimized for different Larmor frequencies. This versatility was essential for demonstrating the broadband capabilities of the S3L detector. Renderings of the S3L insert and the flexible PCB saddle coil are shown in the inset of Fig. 3.1 (a). Detailed dimensions and fabrication procedures are provided in the Methods section.

The S3L insert itself is a sandwiched structure composed of two glass substrates carrying gold metal tracks that define the striplines and Lenz lens loops. The fabrication process relied on standard photolithography, electroplating, and etching steps. Ordyl dry-film photoresist layers were used as a spacer between the glass substrates, simultaneously defining the sample chamber between the stripline conductors. During operation, the NMR signal generated by the sample was detected by the striplines and inductively coupled to the saddle coil. The combined S3L–saddle coil system was tuned to the Larmor frequency of interest and impedance-matched to 50 Ω using capacitors mounted on the probe head.

3.3 Equivalent circuit for stripline Lenz lens

The signal to noise ratio (SNR) of an NMR detector is a complex figure of merit that is influenced by multiple parameters that take into account the experimental conditions (static field), the sample itself (volume or concentration and nuclei to be detected), and the detector design. In the pursuit of high-sensitivity NMR, maximizing the SNR becomes the central goal, as it directly governs the detection limits and the precision of spectral analysis. The present section provides an evaluation of the SNR enhancement when using the saddle coil with the S3L insert compared to the situation when only the standard saddle coil is used as a detector for the same sample volume and geometry. This discussion is based on the electrical model of an NMR probe with a Lenz lens stripline pair shown in Fig. 3.2 (a). Considering the fact that the total noise is due exclusively to the ohmic resistance of the detector, the SNR enhancement ζ can be written as

$$\zeta = \frac{B_{1,S3L}/\sqrt{R_x}}{B_{1,s}/\sqrt{R_s}} = \frac{\eta B_{1,s}/\sqrt{\gamma R_s}}{B_{1,s}/\sqrt{R_s}} = \frac{\eta}{\sqrt{\gamma}}, \tag{3.1}$$

in which $B_{1,S3L}$ and $B_{1,s}$ are respectively the B_1-fields generated by the Lenz lens stripline and the saddle coil in the sample region, R_x and R_s are the terminal resistances of the saddle coil with and without the S3L insert. The ultimate SNR enhancement is based on the RF field enhancement η and the resistance increase γ. The calculation of Eq. 3.1 for this design is presented in detail in **Appendix** Sec. A2. This calculation uses the circuit model of the saddle coil which is inductively coupled with the S3L insert and shown in Fig. 3.2 (a). The saddle coil is connected to a tuning and matching network with two capacitors and a 50 Ω coaxial cable. Upon the insertion of the S3L, the voltage measured at the terminals of the saddle coil, v_x, is modified by the voltages induced due to the coupling between the saddle coil and each of the loops of the S3L (α and β), as described by the equation below, written at the operating frequency ω

$$v_x = (R_s + j\omega L_s)i_s - v_\alpha - v_\beta. \tag{3.2}$$

The presented model also takes into account the symmetry of the problem, which translates into the interchangeability between the indices α and β, so that the induced voltages are

$$v_\alpha = v_\beta = j\omega M_{s\alpha} i_\alpha = j\omega M_{s\beta} i_\beta, \tag{3.3}$$

which determines the terminal impedance of the saddle coil

$$Z_x = R_s + j\omega L_s - 2j\omega M_{s\alpha} \frac{i_\alpha}{i_s}, \tag{3.4}$$

where $M_{s\alpha/\beta}$ is the mutual inductance between the saddle coil and loop α/β, and $i_{\alpha/\beta}$ is the current in loop α/β ($M_{s\alpha}$=$M_{s\beta}$ and i_α=i_β), R_s, L_s, i_s are the resistance, inductance and current values corresponding to the saddle coil. Taking into account the actual geometry of the saddle coil, and the S3L loops (see Fig. 3.2 (b)), as well as the individual B_1-field distributions (shown in Fig. 3.1 (b) and (c)) for the calculation of mutual inductances, a numerical dependency of the SNR enhancement is derived with respect to the distance between the the two striplines, i.e., between the two planes of the S3L loops.

Fig. 3.2 (c) shows both the SNR enhancement effect as a result of using the S3L insert and the absolute SNR provided by the S3L insert at 500 MHz, the former calculated by Eq. 3.1 and the latter from the numerator in Eq. 3.1 given a unit current. The profiles of the B_1-field generated by the striplines (two yellow blocks representing the cross sections) at respectively $h = 200,\ 390\ \mu m$ are also displayed. The results were obtained for a sample volume of 0.4 µL, and for the following geometrical parameters of the S3L insert, $w = 200\ \mu m$, $l = 2\ cm$, and $m = 4\ mm$, see Fig. 3.2 (b).

As expected, there is a significant and rapid increase in the SNR enhancement for small h values, i.e., for a small distance between the striplines, due to the $B_{1,\mathrm{S3L}}$ field being severely restricted between the metal strips. However, the SNR enhancement plot in Fig. 3.2 (c) does not take into account the proximity effect, which becomes important at very low h values and is expected to limit the enhancement effect. As the distance between the striplines increases, the enhancement effect becomes less pronounced. However, it must be noted that it remains around one order of magnitude even for a relatively large separation of $h = 0.5$ mm between the metal strips. The SNR enhancement curve does not depend on the actual amount of sample. The absolute SNR of the S3L insert shows a logarithmic dependency on h, i.e., the SNR increase becomes moderate for larger separations between the strips. The curves in Fig. 3.2 (c) must always be considered in conjunction with the uniformity of the $B_{1,\mathrm{S3L}}$ field, and two profile plots of the field strength at $h = 200$ µm and 390 µm are attached as examples. The stripline confinement effect quickly diminishes with increasing distance between the strips, with the S3L SNR increase being only due to the increase in sample amount. This also means that the B_1 field generated by each stripline will be concentrated around the stripline, thus leading to a highly non-uniform B_1 field distribution between the striplines. This optimization is discussed in more detail in the next section.

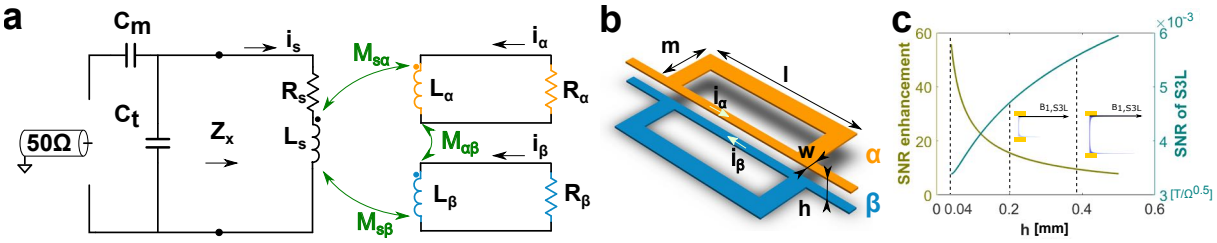

Figure 3.2: *(a) Circuit model of the saddle coil inductively coupled to the S3L insert for SNR enhancement; (b) Dimensional parameters of S3L geometry; (c) Calculated SNR enhancement and absolute SNR vs. stripline spacing h based on the circuit model, and profiles of the B_1-field distribution between two striplines (yellow blocks) respectively with $h = 200,\ 390\ \mu m$. Reproduced from the author's own publication* ***J1*** *with the permission from Springer Nature.*

3.4 Stripline Lenz lens geometry optimization

As with any inductive NMR detector, performance is characterized by several figures of merit. These are evaluated in this section as a function of the geometric characteristics of the S3L insert, including the relative SNR, excitation efficiency, B_1 homogeneity, and B_0 homogeneity.

The SNR has been thoroughly discussed in the previous section and the **Appendix** A2. The excitation efficiency describes the power transfer from an excitation source to the coil through the terminal, depicted as a 50 Ω coaxial cable in Fig. 3.2 (a). By definition, the excitation efficiency is the frequency of the nutation signal at 1 W excitation power [84]. B_1 homogeneity is a critical factor for spin manipulation; poor homogeneity results in varying tip angles across the spin ensemble, leading to deteriorated sample magnetization and reduced SNR. This is commonly evaluated by the ratio of nutation signal intensities at pulse lengths of 450° and 90°, $A_{450°}/A_{90°}$ [88]. B_0 homogeneity directly affects the resolution of the NMR spectra and is primarily influenced by discontinuities in the magnetic susceptibility of the constituent materials of the NMR probe, especially in the vicinity of the sample. The spectral resolution is evaluated here by the linewidth at 0.11% of the full signal height.

The primary optimization parameter of the S3L structure is the spacing between the two striplines, h. As shown in the previous section, h regulates the B_1-field distribution and the mutual coupling between coils, thereby affecting the electrical parameters and the SNR. To ensure a fair comparison of the SNR, the sample volume is calculated as $(h - 2t) \times w \times l$ and is kept constant throughout the optimization by assuming a maximal filling factor. The sample length l coincides with the length of the Lenz lens for two reasons. First, any sample volume outside the Lenz lens suffers from reduced detection sensitivity. Second, a susceptibility mismatch exists at the junctions between the Lenz lens and the stripline (see Sec. 3.4.3). As shown in Fig. 3.1, the stripline extends beyond both sides of the Lenz lens, and this additional length is accounted for in our simulations by assuming it is filled with a susceptibility-matching fluid (matched to the water sample).

3.4.1 Simulation strategy

To evaluate the RF field produced by the S3L chip and optimize the detector geometry, Finite Element Method (FEM) simulations were performed using COMSOL Multiphysics 5.6 (COMSOL AB, Sweden) with the RF module (Electromagnetic Waves, Frequency Domain).

For the geometry model, the reference was established with a 10 mm saddle coil without the S3L insert, which was then compared to a configuration with the chip positioned at the coil center. To ensure a consistent comparison, the sample channel volume was fixed at 0.6 µL with a constant length of 1.4 cm, while the cross-sectional geometry varied as a function of the parameter h. The coil structure utilized the COMSOL built-in property for electroplated gold, while the surrounding domain was defined as air. The sample was modeled as liquid water with an electrical conductivity of $0.005\,\mathrm{S\,m^{-1}}$ and a relative permittivity of 80.2. More material properties used for COMSOL simulations are listed in **Appendix** Sec. A1.

The coil system was enclosed within a spherical domain with a diameter of 6 cm. A perfect electric conductor (PEC) condition was assigned to the boundary to facilitate the characterization of the internal magnetic field. A free tetrahedral mesh was applied to the entire domain, with a refined maximum element size of 250 µm specifically assigned to the coil structure and sample region to ensure numerical convergence in the areas of high field gradient.

We swept stripline spacing h at 500 MHz for water measurement. As the excitation source, a lumped port with 1 A terminal current was connected to the saddle coil model. The relative tolerance of the RF simulation was 1×10^{-4} . The results were processed in MATLAB R2018a for Fig. 3.3. The code used for this processing is demonstrated in **Appendix** Sec. A3.

3.4.2 Computational optimization regarding the stripline spacing

The S3L structure optimization was conducted across 5 configurations generated by sweeping h values from 190 µm to 390 µm, in steps of 50 µm. The stripline width w was adjusted accordingly for each h value to maintain a constant sample volume of 0.4 µL, ensuring a consistent basis for signal extraction. It is important to note that while h and w were coupled to preserve volume, their individual influences on the NMR results were discussed independently. The simulation results for these configurations are presented in Fig. 3.3. For comparison, nutation curves and spectra for the same sample geometries without an S3L insert were simulated and included in Fig. 3.3 (a) and (b).

Fig. 3.3 (a) displays for each configuration the nutation spectrum for the case when the S3L insert is used and for the case when only a dummy insert is considered, i.e., no metal tracks for the stripline or for the Lenz lens structures. The information from Fig. 3.3 (a) was further processed to generate the bar charts of excitation efficiency in Fig. 3.3 (c) and B_1 homogeneity in Fig. 3.3 (d). As expected, the excitation efficiency deteriorates with the increase in stripline separation h because of a weaker coupling between two striplines. B_1 homogeneity shows a similar trend with increasing separation h as the device approaches the situation of two independent

wires. Normalized SNR and SNR enhancement shown in Fig. 3.3 (e) also decrease with the spacing between the striplines. The static field (B_0) homogeneity is reflected by the spectral resolution, which is crucial in building micro detectors. Fig. 3.3 (f) indicates that the optimal field homogeneity is achieved at a spacing of approximately 300 µm.

Fig. 3.3 (b) depicts the simulated NMR spectra, where all signal peaks are normalized with respect to the spectrum at $h = 190\ \mu m$. The signal peaks obtained without the S3L insert (grey area) were adjusted to 0 *ppm* as a reference. Without the S3L, the spectra are greatly affected by low sensitivity, resulting in lower peak magnitudes for the same sample amount. In order to compare the spectral resolutions for different configurations, the linewidths at 0.11% full height were compared, the highest resolution around 1.1 *ppm* being achieved for the first two separation values $h = 190,\ 240\ \mu m$ and being the result of the interplay between h and w.

Based on these results and as a good strategic compromise among the SNR, spectral resolution, as well as the restrictions imposed by the fabrication (detailed in Sec. 3.5.3), a stripline spacing of 210 µm and a track width of 200 µm were selected for the final device.

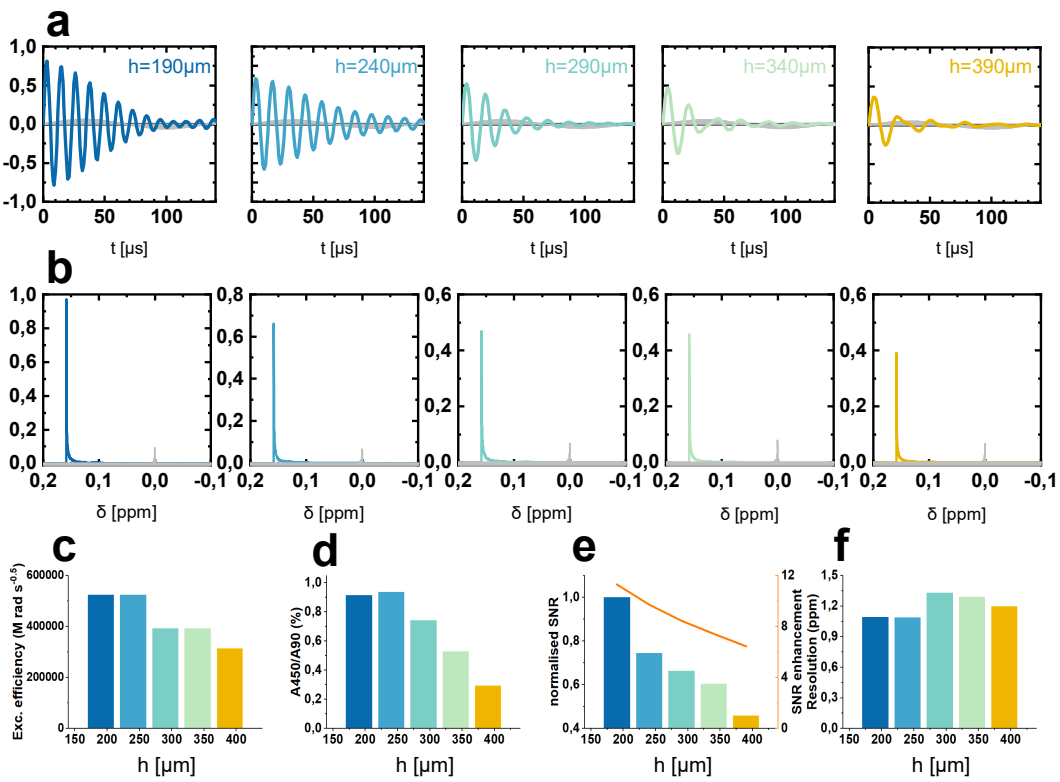

Figure 3.3: *5 different configurations for stripline Lenz lens were simulated in order to determine the optimal spacing (h) between the lobes. The simulation results were processed to calculate: (a) nutation signals for the different configurations compared to the case without an S3L insert (grey signals); (b) NMR spectra following a 90°-pulse and collected for different configurations together with the case where no S3L chip was employed (grey spectra); (c) excitation efficiency; (d) B_1 homogeneity; (e) relative SNR (left axis) and SNR enhancement (right axis), and (f) B_0 homogeneity. Reproduced from the author's own publication* ***J1*** *with the permission from Springer Nature.*

3.4.3 B_0 field distribution analysis along sample channel

In this section, we present a COMSOL simulation study of the influence of material interfaces on the B_0 field distribution along the sample channel. The objective is to evaluate the effective sample volume located within a homogeneous static magnetic field.

A static magnetic field of 11.7 T is applied to the simulation domain, and the field strength along the center of the sample channel is plotted in Fig. 3.4. The full channel length within the Lenz lens is considered the active sample region, while at both ends of the channel the sample volume is extended by a constant length of 0.01 m, designed as a susceptibility-matching plug.

Owing to the geometric symmetry about the vertical axis, only the left half of the structure is analyzed. Four positions (labeled *i*–*iv*) corresponding to changes in the field strength are identified. Point *i* is located at the interface between air and the susceptibility-matching material, where an abrupt decrease in field strength is observed. The results indicate that a 0.01 m susceptibility-matching plug is sufficient to suppress the field inhomogeneity introduced by this interface. Point *ii* corresponds to field perturbations induced by the metal striplines covering the channel. Points *iii* and *iv* mark the locations of the Lenz lens side wings, which give rise to a local increase in the B_0 field. Overall, the static magnetic field within the Lenz lens region exhibits high homogeneity, within a few parts per billion (*ppb*). The residual field inhomogeneities observed near the edges are primarily caused by the loop wings.

An enhanced RF field generated by the S3L is present along the purple-tinted section. A simulated nutation spectrum for this region, shown in Fig. 3.4, yields an amplitude ratio of $A_{450^\circ}/A_{90^\circ} \approx 85\%$, indicating good RF field homogeneity. This computed value is in good agreement with the experimentally measured result reported in the main text.

Ideally, the sample volume should not extend beyond junction point *iii* from the center in order to avoid field perturbations. Further studies are required to develop reliable methods for confining the sample precisely within the homogeneous field region.

3.5 Probe head fabrication

3.5.1 Saddle coil layout and fabrication

For 1D proton measurements at 500 MHz, a Bruker 10 mm saddle coil was available at our institute. However, for other isotopes with lower frequencies, saddle coils were fabricated in-house. For this purpose, a customized saddle coil was designed with the same diameter and length as the standard Bruker coil. It was fabricated by wrapping a flexible PCB sheet around a 3D-printed tube.

Flexible PCB, also known as flexible printed circuit (FPC), uses a thin, flexible plastic substrate to allow the board to bend, twist, or fold without damaging the electrical connections. The substrate materials, such as PEEK and polyimide, are highly durable and thermally stable. Flexible PCB can be fabricated in up to 10 layers, but it is still much thinner than conventional

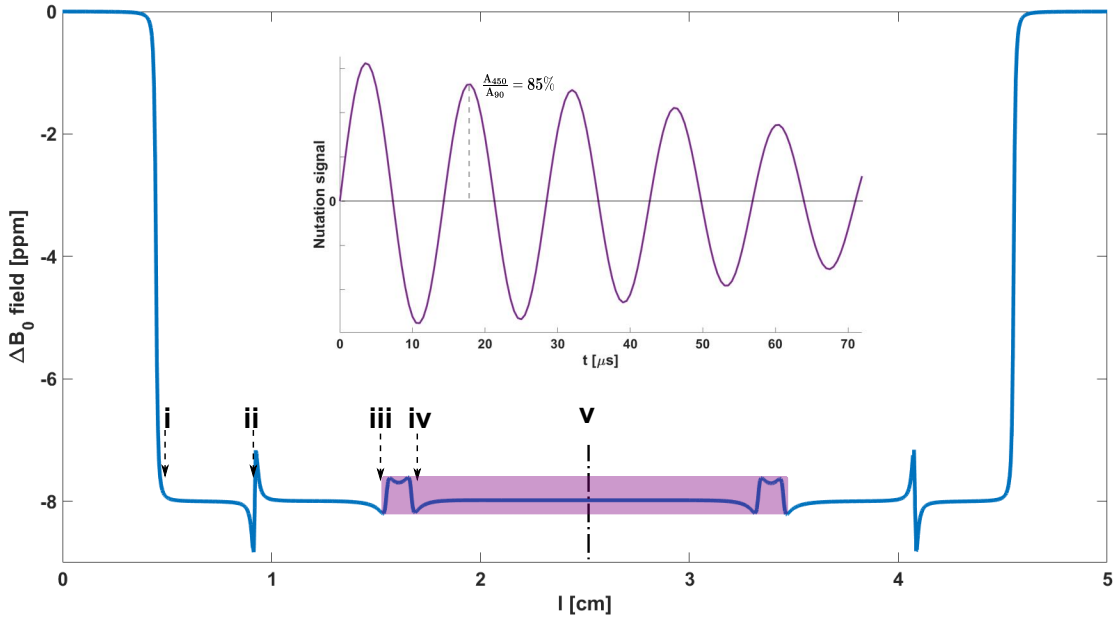

Figure 3.4: *B_0-field strength along the centerline of the chip, intersecting the sample channel and the S3L chip. The insert shows the theoretical proton nutation spectrum envelope, derived from the magnetic field profile corresponding to the sample region as highlighted in purple.*

rigid boards. FPC allows for ultra-compact designs with lightweight and has been applied in integrated passive components, miniaturized coils and coil arrays, and scalable flexible electronics [158, 159, 160, 161]. In the NMR field, flexible PCB exhibits great potential to develop detection coils and coil arrays [139, 162, 163]. The primary advantages of the FPC-based coil include higher achievable SNR and the ability to realize multi-channel coil arrays. A flexible receiver coil can best conform to the sample geometry and avoid the SNR loss from poor coil placement [164]. A FPC-based coil array with multiple channels can be fabricated as series with good reproducibility and enables high-quality individual elements of the array.

In this project, compared to other investigated fabrication methods (e.g., winding copper wire around a plastic tube), flexible PCBs facilitated a well-defined saddle configuration and ensured higher field homogeneity. Additionally, using exposed copper pads on the flexible PCBs simplified the soldering of tuning and matching circuit components compared to traditional copper wires, thereby reducing the introduction of environmental noise. The three-layer flexible PCB substrate was 217 µm thick (Multi Leiterplatten GmbH, Germany). The conductor tracks on the board were 35 µm thick and 2 mm wide. Two conductor layers of chemical gold were utilized in the S3L layout, separated by a 25 µm polyimide insulation layer.

The planar layout of the customized flexible saddle coil is presented in Fig. 3.5 (a), where the openings for tuning and matching capacitors (C_t and C_m) are indicated. The flexible saddle coil was wrapped around a transparent support tube, as shown in Fig. 3.5 (b). The support tube was 3D-printed using ABS filament on an Ultimaker 2+ (Ultimaker B.V., Netherlands) with a 0.4 mm nozzle and the dimension is displayed in Fig. A3 (see **Appendix** Sec. A5.2). The

final rolled-up saddle coil has a height of 20 mm, a diameter of 10 mm, and an aperture angle of 120° based on previous studies [165, 166]. The vertical position of the coil was aligned with the homogeneous region of the static field. The base of the tube featured through-holes for copper sockets, which were compatible with the pins on the NMR probe.

The self resonance frequency of the flexible PCB-based coil was measured to be around 460 MHz, which could be further tuned with non-magnetic capacitors for most nuclei, but was not appropriate for ^{19}F at 470 MHz. The self-resonance frequency of the flexible PCB-based coil was measured at approximately 460 MHz. While this allowed for tuning to most nuclei using non-magnetic capacitors, it was unsuitable for ^{19}F measurements at 470 MHz. Furthermore, the limited availability of specific capacitor values complicated the tuning and matching adjustments. Additionally, when targeting resonance frequencies below 100 MHz, the larger tolerances of high-value capacitors increased uncertainty during the tuning process. For single-resonance detection of ^{31}P at 202 MHz, the inductance and quality factor of the wound coil were 154.3 nH and 37.6, respectively, requiring tuning (C_t) and matching (C_m) capacitances for and C_m were 5.1 pF and 7.5 pF. For ^{7}Li detection at 194 MHz, the coil exhibited an inductance of 147.8 nH and a a Q factor of 38.3, yielding C_t and C_m values of 5.6 pF and 7.5 pF. For ^{23}Na detection at 132.3 MHz, the measured inductance and quality factor were 118.5 nH and 79.9, with both C_t and C_m calculated at 15 pF.

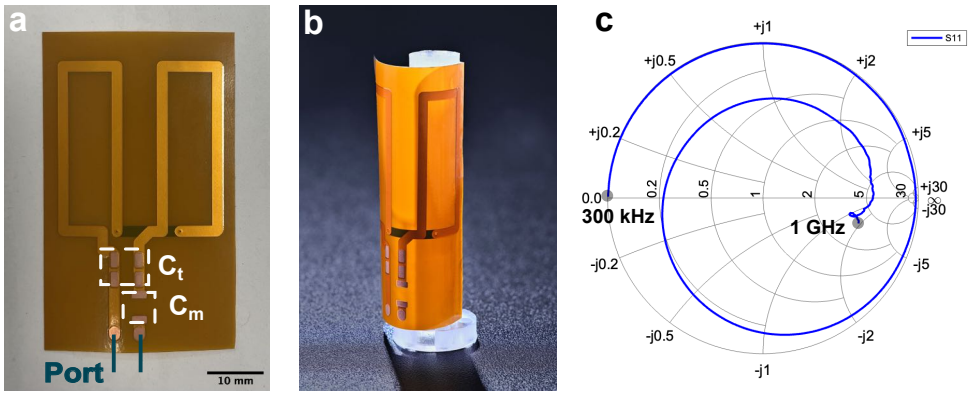

Figure 3.5: *(a) Low-frequency homonuclear saddle coil (< 460 MHz) fabricated on a flexible PCB, featuring buried conductor traces and exposed solder pads for tuning and matching capacitors. (b) Partially wound coil mounted on a 3D-printed support frame. (c) Smith chart of a bare saddle coil from* 300 kHz *to* 1 GHz *without a tuning and matching network, measured using an E5071C network analyzer (Agilent Technologies, CA, USA). Reproduced from the author's own publication* ***J1*** *with the permission from Springer Nature.*

3.5.2 Tuning/Matching for a double resonance saddle coil

For the purpose of demonstrating the S3L capabilities of high frequency homonuclear and heteronuclear experiments, a double channel driving saddle coil was designed, where the resonances for the nuclei ^{1}H and ^{13}C were achieved.

The double resonance circuit is based on the trap circuit design described by Plata *et al.*

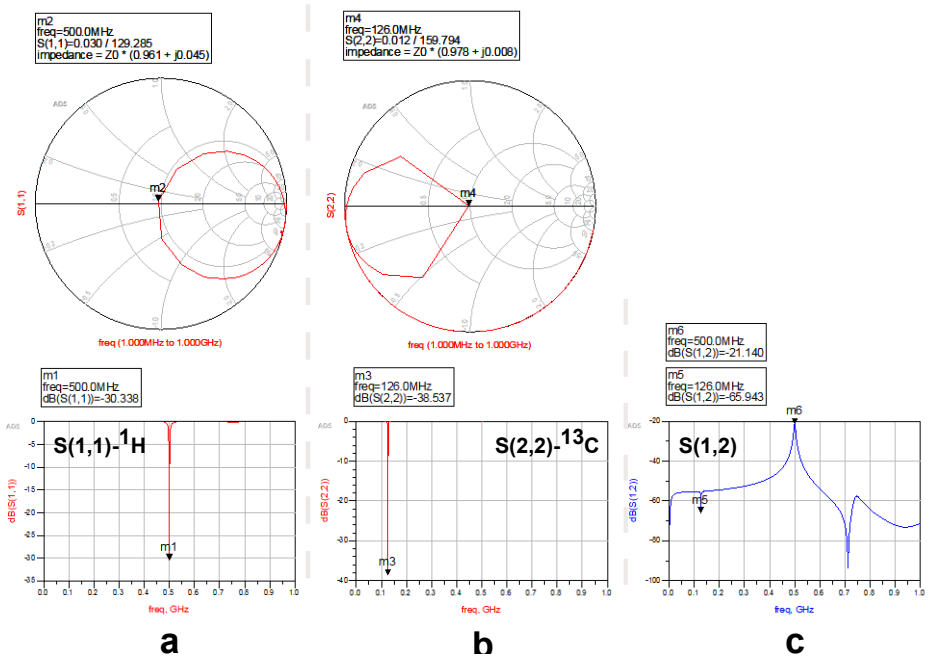

Figure 3.6: *The reflection and transmission curves of $S(1,1)$ (a), $S(2,2)$ (b) and $S(1,2)$ (c) after the component parameter optimization. Port 1 and 2 are connected to the ^{1}H and ^{13}C channels respectively.*

[167, 168]. This configuration is advantageous because, depending on the target nuclei, only the double channel trap circuits require adjustment.

Two optimization goals were implemented in Advanced Design System (ADS): first, $db(S(1,1))$ from the ^{1}H port was required to be lower than $-20\,$dB at approximately 500 MHz while remaining above $-1\,$dB at 125 MHz; second, $db(S(2,2))$ from the ^{13}C port was required to be lower than $-20\,$dB at approximately 125 MHz while remaining above $-1\,$dB at 500 MHz. L_3 was determined by the geometry of the wound saddle coil body, whereas the fixed-value inductors L_1 and L_2 within the trap circuits were selected based on the operating frequencies and laboratory availability.

The simulated reflection curves for $S(1,1)$, $S(2,2)$ and $S(1,2)$ are presented in Fig. 3.6 (a), (b) and (c), showing that reflection is reduced to $-30\,$dB in both channels. To account for potential discrepancies in resonance conditions between simulations and experimental setups, two adjustable non-magnetic capacitors were utilized for fine-tuning.

To circumvent the issue of a self resonance frequency lower than the proton frequency, an alternative design was developed where the coil body was formed by copper tape strips, as shown in Fig. 3.7 (a). The saddle coil maintained the same height and diameter as the single resonance coil described previously, with the conductor strips supported by rounded Kapton foil, the same substrate material used for the flexible PCB in Fig. 3.5. Because double resonance tuning and matching require a more complex circuit, a rigid PCB was deployed at the base of the saddle coil rather than being integrated into a flexible PCB, as presented in Fig. 3.7 (a). The circular PCB was fabricated to fit precisely into the gradient sleeve. The assembled double

channel saddle coil was mounted on the probe head and fine-tuned using two variable capacitors.

The reflection curves for both channels at ^{1}H and ^{13}C frequencies are presented in Fig. 3.7 (b). At their respective resonance frequencies, the proton channel achieved $S(1,1) < -53dB$ and the carbon channel showed $S(2,2) < -38dB$. The data also confirmed sufficient isolation between the two channels at both resonance frequencies.

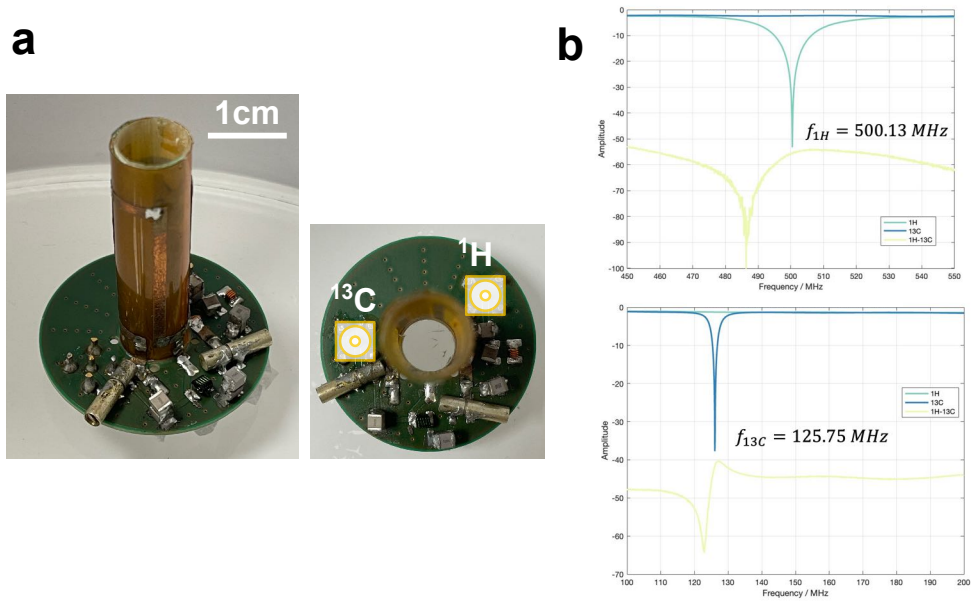

Figure 3.7: *(a) Side and top views of the fabricated double channel saddle coil. (b) Reflection curves ($S(1,1)$ and $S(2,2)$) of both channels across the two frequency ranges of interest. Fine-tuning of the coil inside the magnet was achieved using two adjustable capacitors. The ^{1}H channel exhibits a reflection of -53 dB at its resonance frequency, while the ^{13}C channel shows -38 dB at its respective resonance. The $S(1,2)$ curve displays high isolation between the two channels.*

3.5.3 Microfabrication of S3L chip based on glass wafer

Adopting the optimized geometry described in the section Stripline Lenz lens geometry optimization, the S3L chip was fabricated in the cleanroom following the steps illustrated in Fig. 3.8. Due to geometric symmetry, only half of the chip is presented. Note that the vertical dimension in the schematic is not to scale to allow for better visualization of the layer stack. Further details regarding the cleanroom operations and associated parameters are provided in Table. A2 (see **Appendix** Sec. A4). The mask designs utilized in this process are shown in Fig. A2 (a) (**Appendix** Sec. A5.1).

- **Seed layer deposition** The stripline Lenz lens chip was a sandwiched structure which consisted of two 200 µm 4 " D263 Teco gold-coated glass wafers and an around 200 µm thick Ordyl layer (a dry film photoresist) in between. The glass wafer was first cleaned with a typical routine in the cleanroom by Acetone and Isopropanol and then exposed to Oxygen plasma for 5 min. The wafer was later coated with chromium/gold seed layers (20 nm and 60 nm) for following growth of gold structure.

- **SU-8 lithography** Standard SU-8 lithography process was applied on the top side for patterning the gold Lenz lens and stripline. The thickness of the photoresist was around 20 µm. The utilized mask was shown in Fig. A2 (b).
- **Electroplating & etching** With the seed layer connectd to a DC source, around 20 µm thick gold was electroplated in the SU-8 mould. After SU-8 was stripped off, the seed layer area, which was not covered by the stripline Lenz lens, was also etched away.
- **Ordyl lithography** On the top of the gold structure, an Ordyl layer of around 110 µm (90 µm + 20 µm) was directly laminated on an office laminator. The microfluidic channel and the supporting sidewall of the chip were patterned using lithography process and developed in Ordyl SY developer for 20 min assisted by ultrasound bath. The utilized mask is shown in Fig. A2 (c).
- **Bonding & drilling the inlet and outlet** Ordy lost its stickiness and got dried easily in the air. After development and necessary cleaning of the surface, the wafer was exposed to oxygen plasma for a very short time for a better bonding quality. Taking advantage of the geometry symmetry, we flipped one out of the two identical wafers and covered it on the other. The assembly was aligned under the microscope aided by the align markers and fixed with thermal tapes, and then brought to bonding employing a compression-bonding machine (EVG510 EV Group) under 5 kN force at 95 °C for 4 h. The inlets and outlets were cut with a nanosecond laser (PIRANHA ACSYS) into the top layer, with a hole diameter of around 260 µm. The utilized mask was shown in Fig. A2 (d). The entire wafer assembly was then diced into individual chips using the laser and one batch with two 4 " glass wafers was able to produce 12 pieces of chips.

The final S3L device is shown in a top view in Fig. 3.8 next to a fabricated dummy chip. For the dummy chip, the steps from the seed layer to gold electrodeposition were excluded. Due to the flexibility of Ordyl layer, the thickness difference of the whole chip introduced by the extra gold tracks could be neglected after bonding process.

3.5.4 Characterization of microfabrication process

In this section, the characterization results of two critical stages are presented: stripline Lenz lens electroplating and Ordyl photolithography. These steps significantly influenced the structural and functional integrity of the final devices, making their assessment essential for reliable chip performance. By systematically evaluating these key fabrication steps, potential issues were identified and the fabrication flow was optimized accordingly.

Gold electroplating

In Fig. 3.9, the electroplated conductor structures were characterized via microscopy and vertical scanning interferometry (VSI). VSI is a non-contact optical measurement technique used to characterize surface topography with high vertical resolution, typically in the nanometer range. Compared to other profilometry techniques, VSI is particularly suitable for measuring relatively rough or structured surfaces, such as electroplated features or patterned photoresist

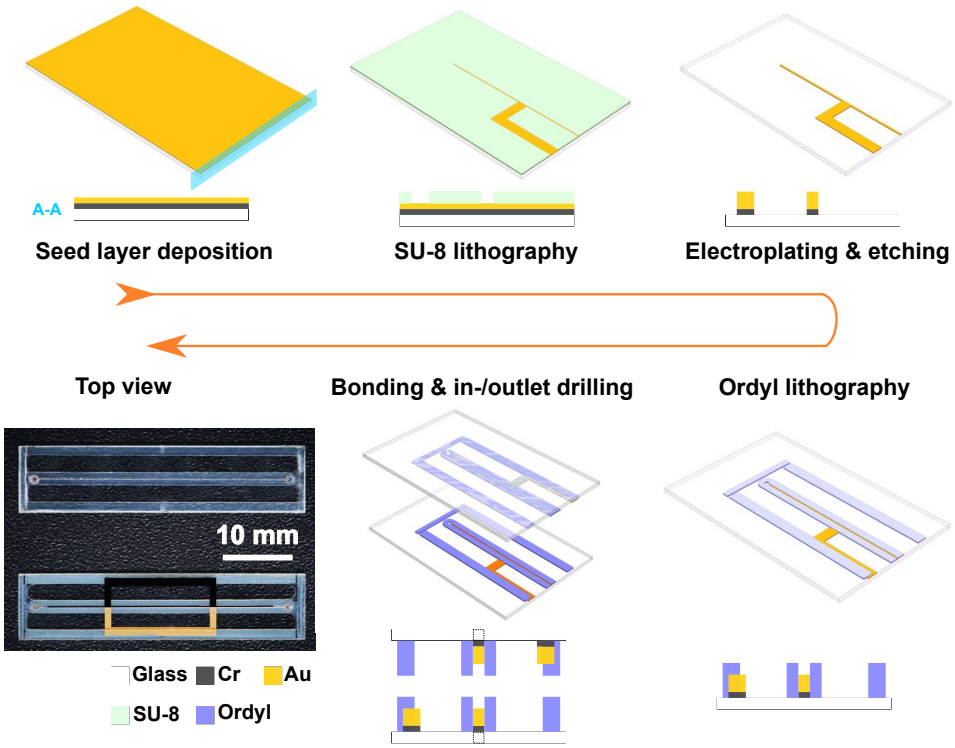

Figure 3.8: *Fabrication process of the S3L chip with both 3D model and 2D illustration, as well as a top view of the fabricated S3L chip alongside with a dummy chip. Reproduced from the author's own publication* ***J1*** *with the permission from Springer Nature.*

layers, which are difficult to characterize with conventional optical or stylus profilometry.

Fig. 3.9 (a) to (c) show microscopy images with a scale bar of 20 µm. Fig. 3.9 (a) demonstrates good uniformity of the electroplated surface despite slightly higher edges. Fig. 3.9 (b) shows a bead artifact occasionally occurring at the corner of an alignment marker, which could influence the electrical properties of the conductor. Occasionally, shadowy spots were observed on the surface, as shown in Fig. 3.9 (c). These were suspected to be burned organic material, which could be removed in the subsequent cleaning process.

Fig. 3.9 (d) and (e) show the 3D surface profiles at the junction of the stripline and Lenz lens obtained via VSI. Two lines were defined as the X and Y profiles, providing quantitative data for the thickness and surface roughness of the electroplated layer. Fig. 3.9 (e) reconstructs a 3D surface profile of the junction, offering a clear view of the electroplating uniformity and structural dimensions. The VSI measurements show that the electroplated structures have good thickness uniformity and low surface roughness. Both the 3D surface profile and the line profiles demonstrate a uniform electroplating quality that satisfies the requirements of the stripline Lenz lens chips.

Ordyl dry film photolithography

Ordyl etching quality is another major concern, as it directly affects sample capacity and bonding stability. Fig. 3.10 shows the microscopy images of the developed Ordyl structures.

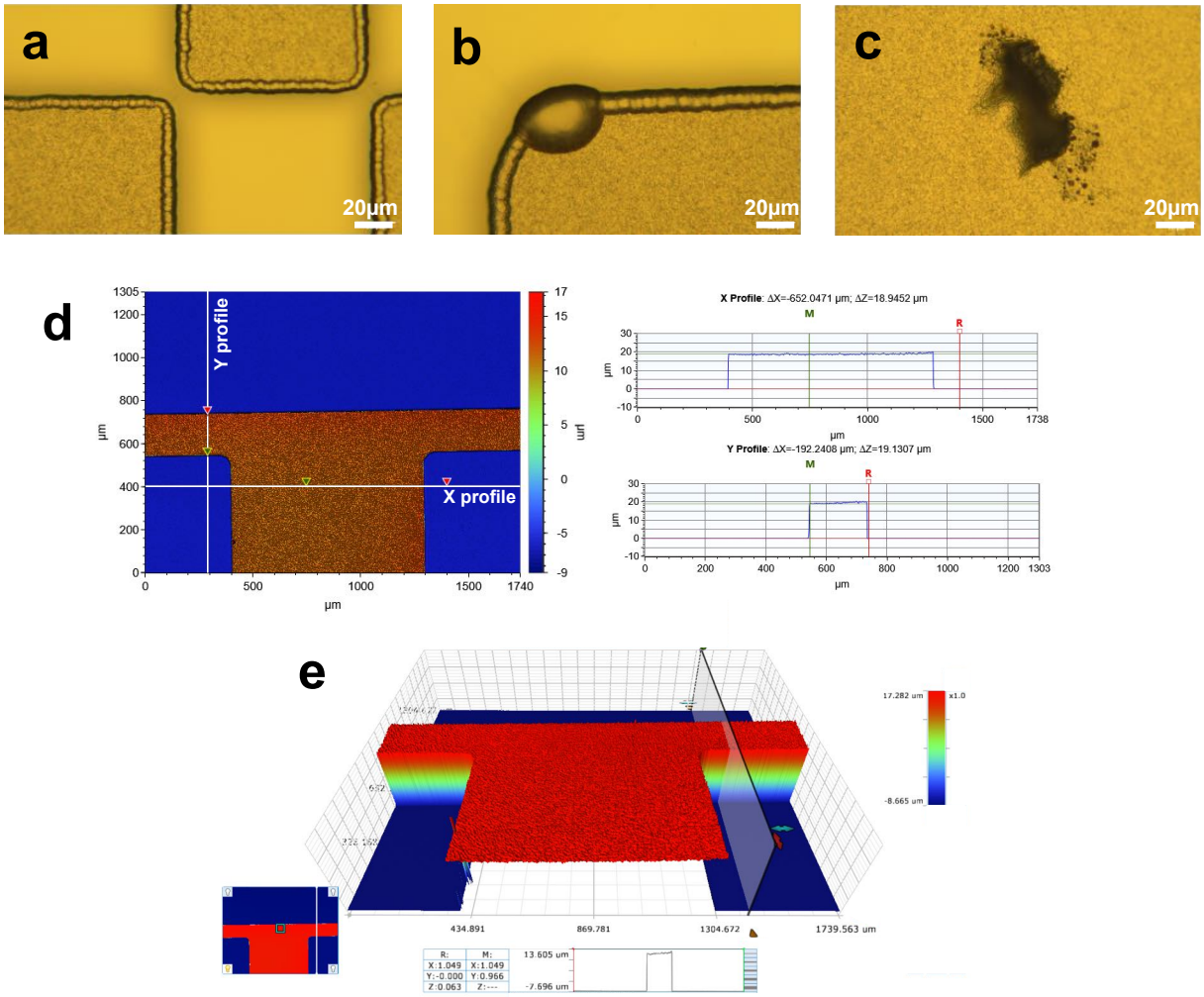

Figure 3.9: *(a) Microscopy image of the electroplated elements, showing excessive plating at the edges of the conductive features. (b) Bead defect at the edge. (c) Shadowing defect on the metal surface. (d) and (e) VSI 2D and 3D images of the junction between the stripline and the Lenz lens, revealing the dimensions and surface profile of the gold structure deposited on the seed layer.*

Etching performance depends primarily on the structure geometry, substrate material, exposure dosage and development time. Etched channels with high aspect ratios typically exhibit a width difference between the top (Fig. 3.10 (a)) and bottom (Fig. 3.10 (b)) surfaces of the resist layer. In some cases, the developer solution cannot completely remove the unexposed resist, resulting in a clogged channel. Meanwhile, excessive exposure may lead to unintended hardening of structures outside the boundaries due to reflected light. Increased development time led to the detachment of small structures, such as alignment marks, from the wafer (Fig. 3.10 (c)). Thus, the flip-and-assembly method—using two wafer pieces each with half the total aspect ratio—improved fabrication quality and simplified the process despite the extra effort required in the layout. Cross-sectional characterization revealed that the sample channel in an S3L chip was approximately 160 µm wide with vertical sidewalls. In contrast, the dummy chip exhibited an inverted trapezoidal cross-section, with a short base of approximately 100 µm at the glass surface and a long base of 160 µm. Consequently, the sample volume in a dummy chip was

approximately 15% less than in an S3L chip.

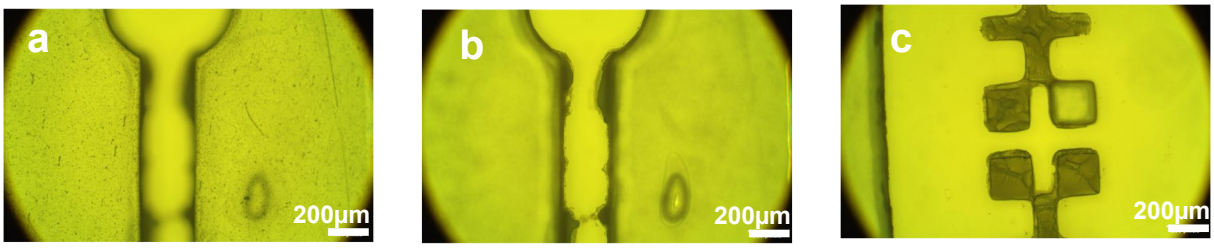

Figure 3.10: *Optical microscopy images of the laminated Ordyl structures after the development process. Panels (a)–(c) focus on the top surface, the glass surface of the channel, and the alignment marks, respectively.*

Glass wafer dicing using laser

Fig. 3.11 presents the experimental setup for dicing a glass wafer with dummy chip modules inside the chamber of a nanosecond laser, as well as optical microscopy images of the chips after laser cutting. The laser was first guided to cut the inlet and outlet, followed by cutting the chip outline. Upon completion, the finished chip fell onto the metal surface below. Owing to its low mass and sufficient mechanical robustness, the chip was not damaged during this process.

Fig. 3.11 (b) shows that the periphery of the inlet hole was melted by the laser, resulting in a diameter of approximately 260 µm. Fig. 3.11 (c) and (d) show that the laser reached the bottom glass layer and induced cracks on the surface. Therefore, preliminary optimization of the laser intensity and exposure duration was necessary to prevent cutting through the chip and potential sample leakage from the backside. Fig. 3.11 (e) shows the channel interior after laser cutting, where debris and residues were observed. The chip was rinsed multiple times prior to experiments.

Artifacts in chip alignment

As explained in the section **Apparatus** and **Stripline Lenz lens geometry optimization**, both the alignment between the two striplines and the alignment of the stripline with respect to the static magnetic field are critical. In addition, the sample channel is formed by multiple overlaid layers. Therefore, even slight misalignment can significantly affect the available sample space. To evaluate the alignment quality, both the S3L chip and the dummy chip were cut into two halves using the laser, and the cross-sectional surfaces were held vertically under the microscope for inspection, as shown in Fig. 3.12 (a) and (c). In parallel, the S3L chip and the dummy chip were tested with sample loading, as shown in Fig. 3.12 (b) and (d). The dimensions of the different structural features are shown in detail.

Fig. 3.12 (a) shows a misalignment of approximately 50 µm between the two striplines in the cross-section of an S3L chip. This chip was bonded from two wafers, each laminated with a single Ordyl layer. As a result, two misaligned sample chambers with well-defined profiles were formed. In this case, the sample capacity was not significantly affected by the alignment error. The channel width was approximately 190 µm, slightly smaller than the stripline width, while the channel height was around 151 µm. However, the misalignment between the two striplines

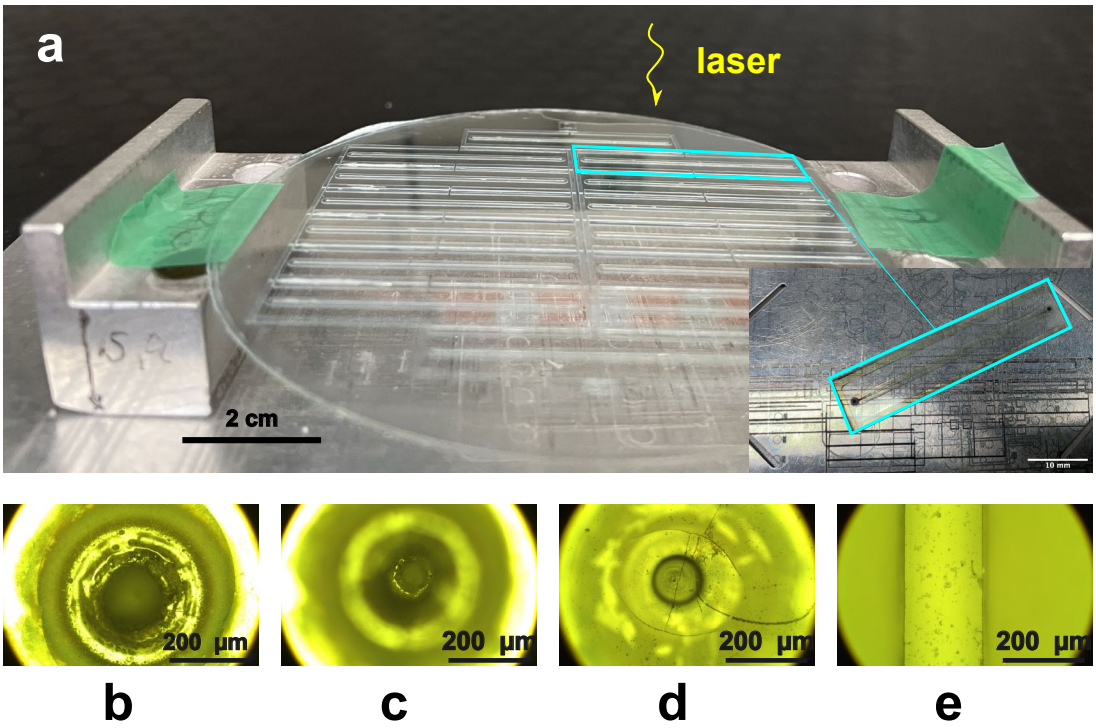

Figure 3.11: *Experimental setup of the glass wafer in the laser cutter chamber and optical microscopy images of the laser-fabricated holes. (a) The wafer, consisting of 14 dummy chips, was positioned on the platform using tape. (b) Microscopy image of a hole focusing on the top surface. (c) Microscopy image focusing on the channel surface through the hole. (d) microscopy image of the back surface of the chip. (e) Optical microscopy image of the channel after laser cutting.*

is expected to substantially distort the B_1 field distribution and reduce the excitation efficiency. Consequently, such a chip configuration is not ideal for subsequent NMR measurements.

In contrast to the S3L chip, the channel in the dummy chip was strongly affected by the development process, resulting in a cross-sectional profile resembling a hexagon, as shown in Fig. 3.12 (c). Nevertheless, the channel width at half height was approximately 185 µm, which is close to the designed dimension. Fig. 3.12 (b) shows effective sealing of the channel, and sample loading was not adversely affected by the misalignment. However, Fig. 3.12 (d) shows air bubbles along the channel in the dummy chip, indicating a potential issue during loading. Ordyl is a hydrophobic material with a water contact angle of approximately 75° [169], which increases the likelihood of air bubbles becoming trapped within the channel. Therefore, vacuum pumping was routinely applied to filled chips for a sufficient duration prior to sealing the inlets and outlets.

This section presents a series of characterization results for the fabricated S3L and dummy chips, which are essential for optimizing the fabrication procedures and increasing the yield of functional S3L chips in future work. It should be noted that the NMR results presented in the subsequent sections were obtained using only qualified chips.

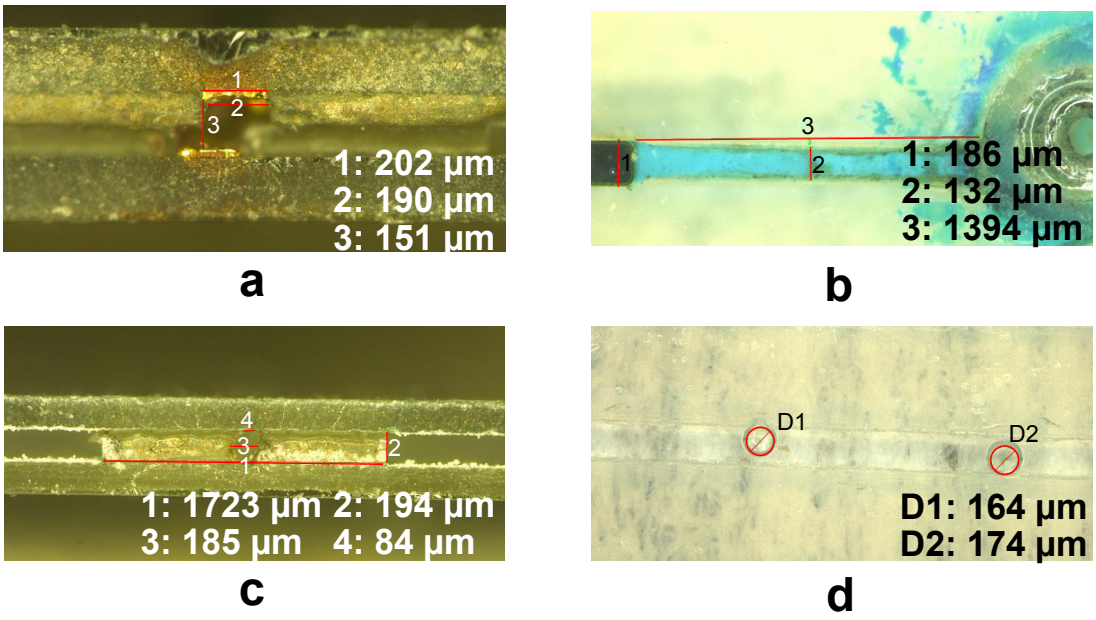

Figure 3.12: *Dimensional characterization of structural alignment in two different chips and their sample-loading conditions. (a) Microscopy image of the cross-section of an S3L chip. (b) Optical microscopy image of the S3L chip filled with tinted water. (c) Microscopy image of the cross-section of a dummy chip. (d) Microscopy image of the dummy chip filled with pure water, with two air bubbles highlighted.*

3.5.5 Attempt of S3L chip based on rigid PCB

The S3L chip fabricated on the glass wafer using cleanroom processes proved to be highly reliable and fully functional. As described in the previous section, the final successful fabrication route was established through an iterative process of trial and error. Prior to adopting this methodology, we explored an alternative approach based on rigid PCB substrates, which offered lower cost and faster prototyping compared to cleanroom fabrication. In this section, we report the fabrication attempts using rigid PCBs and explain why this approach was ultimately abandoned, providing practical insight for researchers considering similar device architectures.

The PCB-based S3L chip design and layout are shown in Fig. 3.13 (a). The core component was single-layer S3L PCBs (green), which incorporated the conductive trace geometry and enabled rapid and economical prototyping. Two PCB pieces were bonded using double-sided Kapton tape, and a physical prototype is shown as an inset next to the exploded view. The assembled S3L chip was mounted inside the saddle coil using transparent PMMA support structures. The dimension of the PMMA supporter is shown in is displayed in Fig. A4 (see **Appendix** Sec. A5.2). The central spacer layer consisted of three stacked Kapton tapes, each approximately 70 µm thick, resulting in a total sample channel height of about 210 µm. The microfluidic channel and inlet/outlet structures in the middle layer were patterned by laser cutting, as shown in Fig. 3.13 (b) and (c). However, laser processing introduced surface glitches and residual debris along the inner sidewalls. In addition, the soft adhesive layer of the Kapton tape rendered the structure less mechanically stable and highly sensitive to applied pressure.

By contrast, Ordyl-based lithography offers substantially higher dimensional accuracy and a more rigid structural layer at the micrometre scale than laser-cut Kapton tape. These limitations in mechanical stability, surface quality, and fabrication reproducibility, in the first place, led us to abandon the PCB-based approach in favor of the cleanroom-fabricated S3L chips.

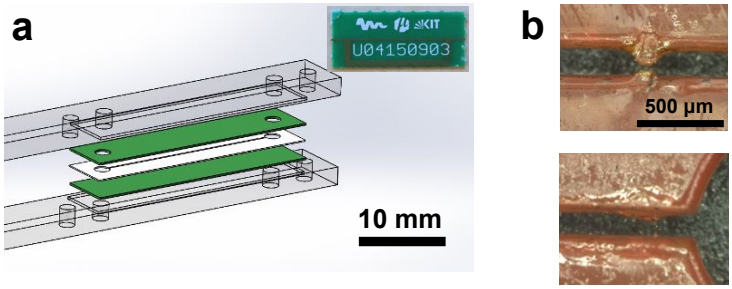

Figure 3.13: *Structural configuration and fabrication details of the rigid PCB-based S3L chip. (a) Exploded schematic view of the device assembly alongside a physical prototype (inset). The chip comprises two single-layer stripline Lenz lens (green) and a central double-sided Kapton tape. (b) and (c) Detailed view of the the laser-cut double-sided Kapton tape (orange) used to bond two functional stripline PCBs.*

Beyond the structural reliability issues associated with the Kapton tape, a major limitation of the PCB S3L chip approach lies in the intrinsic material inhomogeneity of standard PCB substrates. Conventional PCBs are fabricated from woven glass cloth filled with epoxy resin [170]. In single-layer PCBs, the resin layer is relatively thin, making the buried glass weave pattern visible and even tactile on the surface. The dielectric properties of the glass fiber and the epoxy resin differ substantially. The glass strand forming the weave structure exhibits a relative permittivity of approximately 6 with very low dielectric loss [171], whereas the epoxy resin has a relative permittivity of approximately 3 and exhibits varying dielectric losses depending on the specific laminate formulation. This dielectric inhomogeneity results in a non-uniform electromagnetic field distribution, which can introduce artifacts in NMR spectra and MRI images.

To assess this effect experimentally, MRI measurements were performed on both a PCB S3L chip and a PCB dummy chip. The two chips were mounted on PMMA supports and positioned at the center of the saddle coil. For this validation experiment, minor positional offsets and corresponding magnetic field variations between the two samples were neglected. The experimental setup and resulting MRI images are shown in Fig. 3.14. The field of view (FOV) was 6 mm × 6 mm with an in-plane resolution of 0.0469 mm. Signal acquisition was performed with an echo time of 8.7 µs and a flip angle of 15°.

Figure 3.14 (b) shows the MRI signal in the XY-plane, perpendicular to the B_0 field direction. The clear brightness difference between the two signal regions confirms that the PCB-based S3L chip enhances the NMR signal as intended. Figures 3.14 (c) and (d) present signal distributions in the XZ- and YZ-planes across the sample channel. While the PCB dummy chip produces a weak but spatially uniform signal, the PCB S3L chip exhibits a strong signal with a pronounced periodic pattern. The period length is approximately 0.78 mm. Such periodic modulation is detrimental to NMR signal acquisition and image quality. For reference, the typical glass weave

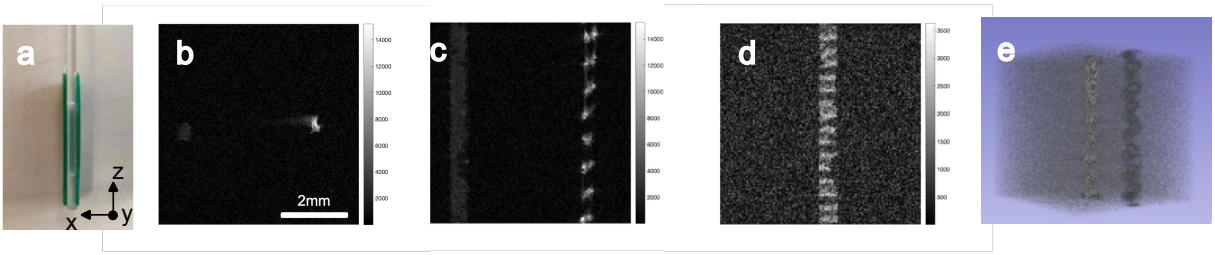

Figure 3.14: *Multidimensional MRI Analysis of PCB S3L chip and dummy chip. (a) Photo of the experimental setup. (b) MRI signals along the Z-axis (B_0 direction). (c) MRI signals along the Y-axis (perpendicular to B_1 direction), showing the cross section of the sample channel. (d) MRI signals along the X-axis (parallel to B_1 direction). (e) 3D reconstruction of the MRI signal.*

pitch in FR4 materials is approximately 0.45 mm (17.9 mil for 106 glass weave) [172], which is comparable to the observed spatial periodicity. In contrast, residues originating from laser-cut Kapton layers are random in nature and would not generate a regular spatial modulation. The observed periodic signal pattern is therefore attributed to the fiberglass weave structure inherent to the single-layer PCB substrate.

These results demonstrate that single-layer PCB substrates are unsuitable for fabricating stripline Lenz lens components that are in direct contact with the NMR sample, due to the dielectric inhomogeneity imposed by the fiberglass weave.

3.6 NMR measurements

3.6.1 NMR system setup

The NMR/MRI experiments were conducted on an 11.74 T Avance III Bruker NMR system (Bruker BioSpin, Rheinstetten, Germany) equipped with a Micro5 micro-imaging probe and a gradient sleeve.

For sample loading, the capillary effect was insufficient despite the microscale dimensions of the channel, due to the rough surfaces and edges of the laser-cut holes and the Ordyl sidewalls. Therefore, a syringe fitted with polymer tubing at the tip was used to inject the sample solution into the channel. The inlet and outlet were subsequently sealed with small pieces of tape. The detector assembly, consisting of the loaded chip and the saddle coil, was then mounted onto the probe and aligned with the aid of a PMMA support, such that the chip was oriented vertically parallel to the static B_0 field and horizontally perpendicular to the RF B_1 field. With manual alignment, the angular deviation from the ideal perpendicular orientation was less than 11°, primarily due to the finite thickness of the support structure.

For NMR measurement operation and spectra processing, the software TopSpin 3.5pl2 is applied. ^{1}H signal is routed through a narrow-band pre-amplifier (^{1}H LNA Module 500, Bruker BioSpin, Rheinstetten, Germany) with 1 dB noise figure while X-nuclei signals are routed through a broadband pre-amplifier (XBB19F 2HS Module 500, Bruker BioSpin, Rheinstetten, Germany)

with 2 dB noise figure. The temperature is measured to be 30 °C from the system. Main NMR acquisition data for all isotopes are presented in Table 3.1.

MRI measurements were performed using ParaVision 6.0.1 (Bruker BioSpin). A FLASH sequence was applied with modified parameters to obtain the MRI results shown in Fig. 3.15 (f). The repetition time was set to 1 s. The field of view was 2 mm × 2 mm with an in-plane resolution of 0.025 mm. The slice thickness was 0.2 mm, and the receiver bandwidth was 20 MHz. Image post-processing was carried out using MATLAB.

To assess the broadband performance of the S3L insert, four nuclei were selected to cover a Larmor frequency range from 132 MHz to 500 MHz, namely ^{23}Na, ^{7}Li, ^{31}P, and ^{1}H. The corresponding one-dimensional spectra are presented in Fig. 3.15. The characterization was performed using the following samples: 300 mM sucrose and 30 mM TSP in deionized water for the ^{1}H spectrum; 1 M LiTFSI in EMI–TFSI for ^{7}Li; and 3 M NaH_2PO_4 in deionized water for both ^{23}Na and ^{31}P. To account for fabrication-related imperfections of the chip, such as irregularities in the photoresist-defined channel that may reduce the available sample volume, the effective sample volume was corrected to 0.32 µL.

Furthermore, we performed a ^{1}H-^{13}C HSQC (Heteronuclear Single Quantum Coherence) measurement to present its promising application in 2D NMR spectroscopy, which is shown as Fig. 3.16.

The performance of the S3L insert was evaluated using two experimental configurations, as shown in Fig. 3.1. In the first configuration, the S3L insert was positioned such that the plane of the Lenz lens was perpendicular to the B_1 field of the saddle coil. In the second configuration, a dummy chip containing only the sample channel, without a stripline Lenz lens, was used as a reference.

When operating in the S3L configuration, the following precautions were taken to maximize coupling between the saddle coil and the Lenz lens structure. The Lenz lens was fully inserted into the saddle coil, and its plane was precisely aligned perpendicular to the saddle coil's B_1 field. Simultaneously, the stripline and the sample channel were aligned parallel to the static B_0 field.

3.6.2 1D NMR with multiple isotopes and MRI experiments

Fig. 3.15 summarizes the NMR spectra with four different isotopes, and nutation signals recorded with ^{1}H. For a clearer visual comparison, the spectra with the same isotope were scaled to have the same noise level, i.e., the same baseline height. The peak corresponding to TSP was set at 0 ppm in the proton spectrum, while the peaks corresponding to ^{23}Na, ^{7}Li, ^{31}P in the respective spectra were set to 0 ppm. The key experimental parameters are summarised in Table 3.1 for a quantitative comparative evaluation.

As presented in Fig. 3.15 (a), a zoomed view along with a full view shows the ^{1}H signal enhancement with the S3L chip coupled to the saddle coil. From these two spectra obtained

with 10 W excitation power and a receiver gain of 32, the respective SNR of the singlet water peak at 4.8 *ppm* was calculated. The single scan SNR enhancement between a perpendicular S3L chip and dummy chip, i.e., orange and blue curves, was 7030/628 = 11. With the S3L chip facing the B_1-field, the pulse length was cut down from 27 µs to 3 µs showing a 9-fold field enhancement. In addition, the linewidth of the peak with a perpendicular S3L chip was narrowed from 6 Hz down to 3 Hz, which reflects an improved field homogeneity. The shim condition was calibrated separately for each setup. The S3L add-on featured an equivalent nLOD value calculated at 600 MHz of 18 nmol$\sqrt{\text{s}}$, which was slightly lower compared to the NMR micro-detectors, keeping in mind however that all other detectors are active devices, whereas the S3L insert operated in a passive mode. The S3L thus compares favorably in terms of spectral resolution (around 6 *ppb* in the benchmarking proton measurement) and B_1-field homogeneity [19, 20, 21, 22, 173, 174].

^{7}Li experiments displayed a single peak from the LiTFSI sample as displayed in Fig. 3.15 (b). Switching from the dummy chip to the S3L chip, the SNR enhancement was around 8.4, reaching an SNR of 402 with 512 averages, due to the lower NMR sensitivity and an nLOD of 82 nmol$\sqrt{\text{s}}$. At the same time, the linewidth dropped from 4.6 Hz to 2.4 Hz. From the nutation spectrum (not displayed here), $A_{450°}/A_{90°}$ was around 81%.

^{23}Na and ^{31}P spectra (Fig. 3.15 (c) and (d) respectively) were obtained with 3 M NaH_2PO_4 solution in DI water. The relatively high concentration of this sample was necessary due to their even lower molar receptivities than ^{7}Li. As shown in Table 3.1, the ^{23}Na signal had an enhancement of around 6.6 and the ^{31}P signal had an SNR enhancement of 6.8.

Fig. 3.15 (e) presents the nutation spectrum acquired using a water sample in order to determine the 90-degree pulse length, and to assess the field homogeneity by calculating the ratio $A_{450°}/A_{90°}$. This revealed a good B_1-field homogeneity of 85.8% when using the S3L insert.

MRI experiment results with two different chips are presented in Fig. 3.15 (f), in which distilled water is used as the sample. Each image has 80×80 pixels with a pixel resolution of 25 µm, and is measured from a slice thickness of 200 µm. The pixel value is scaled to a range of 0–250. The repetition time and the excitation power are adjusted towards a best SNR respectively, 1 s and 0.18 mW for the S3L chip while 1 s and 20 mW for the dummy chip. It is noted that the dummy chip result is acquired with 16 averages, which brought a 4-fold SNR enhancement. As shown in the images, some spots appear to have weaker signals due to air bubbles formed in the water sample after continuing experiment. A profile of the signal amplitude across the sample region is also attached, which reflects directly the signal and noise level collected with one pixel. A sharp boundary of the signal area is observed due to the metal strip constrains.

For SNR calculation, regions of interest (ROIs) were defined in a no-sample region to estimate noise and in the sample region to estimate signal. The SNR was calculated as the ratio of the mean signal intensity in the sample region to the root-mean-square (RMS) noise measured in the noise region. To improve accuracy, four square ROIs were selected in the four corners of the image surrounding the stripline. For a single average, the MRI SNR was approximately 11.6 for the S3L chip and 1.38 for the dummy chip, corresponding to an enhancement factor of 8.4. This enhancement is in good agreement with the NMR results, as expected. The slightly lower

enhancement observed in MRI compared to the proton NMR experiment is primarily attributed to the presence of air bubbles in the fluidic channel.

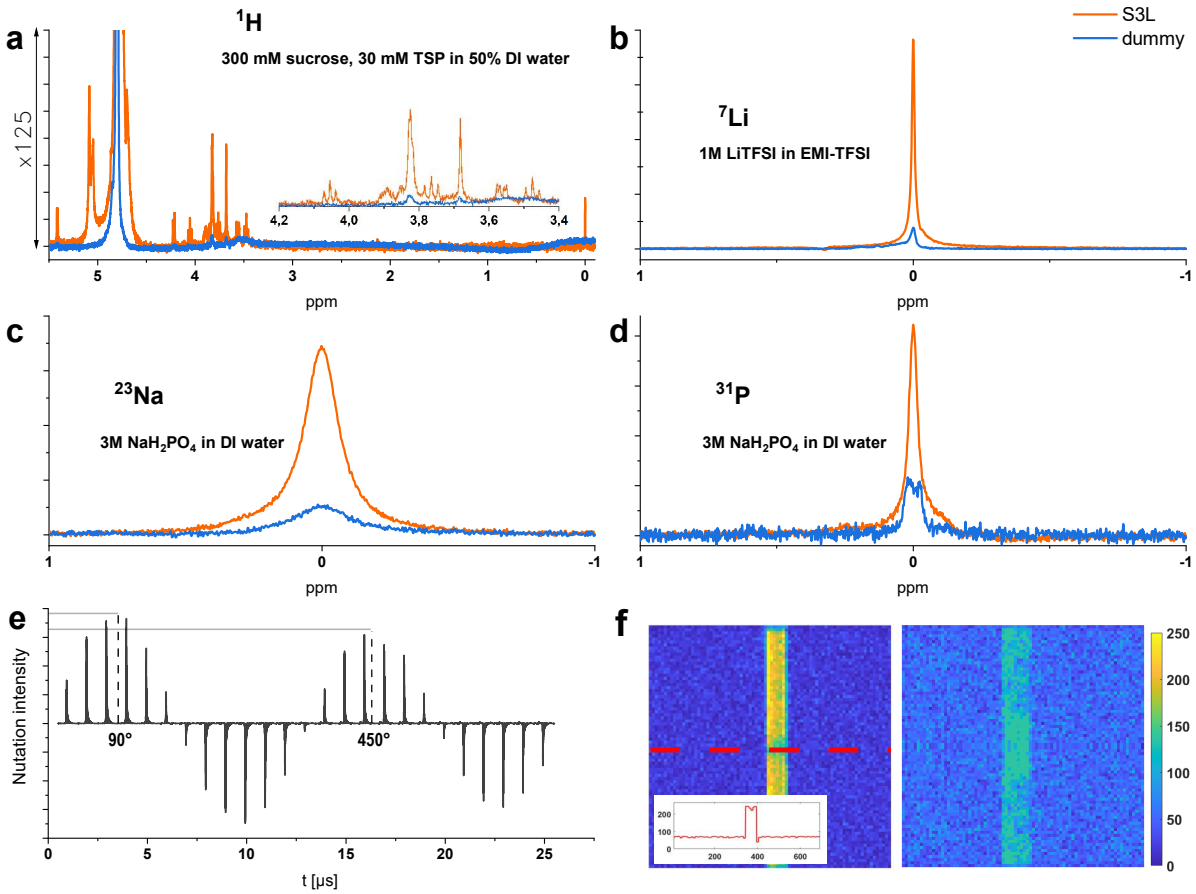

Figure 3.15: *Comparative spectra for different nuclei using a dummy chip and the broadband S3L add-on. (a) Proton ^{1}H spectra at* 500 MHz. *The insert shows more detail for the region between* 3.4 ppm *to* 4.2 ppm. *(b) Lithium ^{7}Li spectra at* 194 MHz. *(c) Sodium ^{23}Na spectra at* 132 MHz. *(d) Phosphorous ^{31}P spectra at* 202 MHz. *(e) A proton ^{1}H nutation spectrum obtained using the S3L, corresponding to the orange curve in (a). (f) MRI of DI water at the center of the stripline with an S3L chip (left) and MRI of DI water with a dummy chip (right). A profile of signal intensity along the red dotted line is addressed. Reproduced from the author's own publication* ***J1*** *with the permission from Springer Nature.*

3.6.3 Double channel NMR pulse sequences on the S3L

NMR is powerful tool to predict the structure of a molecule. Though most structural information can be extracted from single channel RF experiments, yet a double channel RF experiment may help to reveal obscured information. The two most used pulse sequences are heteronuclear, of which one class is referred to as decoupled sequences, the other as coherence spectroscopy experiments. Therefore, it is essential for a suitable resonator, in the present case, the S3L, to be capable of handling heteronuclear experiments.

Table 3.1: *NMR broadband reception at frequencies of different nuclei in an* 11.74 T *field.*

Isotopes	**^{1}H**		**^{31}P**		**^{7}Li**		**^{23}Na**	
Larmor freq. (MHz)	500		202		194		132	
Rel. molar receptivity	1.00		0.07		0.29		0.09	
Configuration	S3L	dummy	S3L	dummy	S3L	dummy	S3L	dummy
Power (watt)	10	10	10	10	10	10	10	10
Pulse length (µs)	3	27	15	15	30	30	10	10
Number of scans	1	1	128	128	512	512	256	256
Relaxation delay (s)	10	10	5	5	1	1	5	5
Linewidth (Hz)	3.1	6.2	6.8	14.6	4.6	6.8	19.6	34
Measured SNR	7030	628	68	10	402	48	79	12
nLOD (nmol$\sqrt{\text{s}}$)	18	204	914	6237	56	465	1038	7171
SNR enhancement	11.2		6.8		8.4		6.6	

Two types of pulse sequence were applied, ^{1}H-decoupled ^{13}C detection, and ^{1}H-^{13}C HSQC. The graphical representation of the pulse sequences is shown in Fig. 3.16 (a) and (c).

The spectra shown in the Fig. 3.16 (b) and (d) were acquired using an S3L, where the sample used was 1 M ^{13}C labeled D-glucose in 90:10 D_2O/H_2O. The pulse parameters for the experiments are summarized in Table 3.2 and 3.3. Without the the S3L, spectra of the measurements described could not be acquired due to low signal levels.

3.7 Conclusion

Micro-coil NMR has long been pursued as an effective route to improving sensitivity while reducing the required sample volume. Although a wide range of micro-coil geometries has been developed for specific applications, the design and fabrication of application-specific resonators remain time-consuming and costly, particularly in laboratories where experimental requirements evolve rapidly. Given the high cost and operational complexity of NMR instrumentation, there is a strong incentive to develop detector concepts that are simple to implement, compatible with existing probe hardware, and adaptable across a broad range of nuclei and frequencies on a single magnet.

In this chapter, a stripline Lenz lens (S3L) add-on has been introduced and systematically characterized as a solution to these challenges. By combining a mature stripline geometry with a Lenz lens structure, the S3L structure provides a simple yet effective means of concentrating the RF magnetic field generated by an external excitation coil into a confined sample region, while

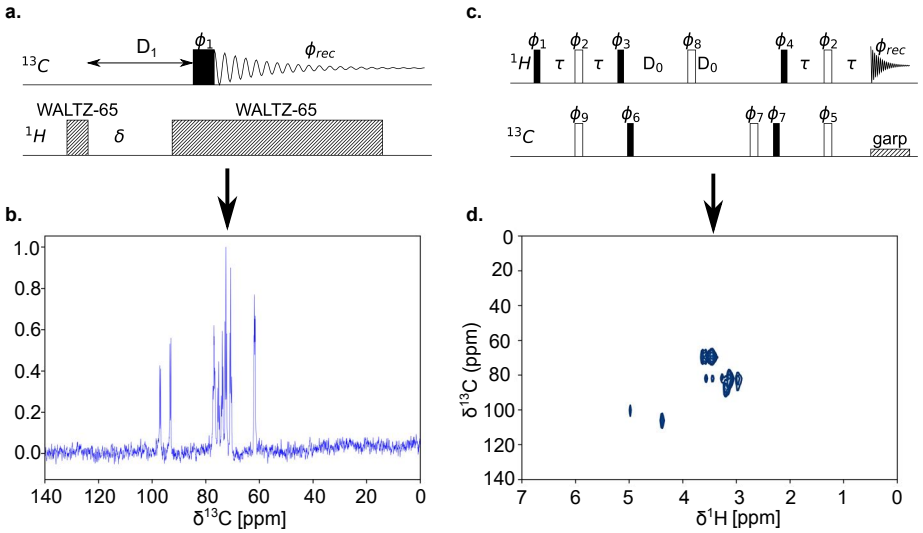

Figure 3.16: *(a) Pulse sequence used for the ^{13}C detection with ^{1}H. The composite pulse used for decoupling was "Waltz-65". (b) The ^{13}C spectrum obtained from the pulse sequence shown in (a). The solution used was 1M ^{13}C-labeled D-glucose in 90:10 D_2O/H_2O. (c) The pulse sequence used for 2D ^{1}H-^{13}C HSQC. The spectra were recorded without any gradients. (d) ^{1}H-^{13}C HSQC spectra plotted on a 2D scale, with y-axis representing frequency shift in ^{13}C, and x-axis representing frequency shift in ^{1}H. Reproduced from the author's own publication **J1** with the permission from Springer Nature.*

simultaneously reorienting the B_1 field flux by 90°. Numerical simulations predict a local RF field enhancement of up to a factor of 20, with corresponding SNR gains of up to 11, depending primarily on the spacing between the striplines. Importantly, the dimensions of the add-on can be readily adapted to different coil sizes to ensure efficient coupling, enabling the concept to be transferred to a wide range of experimental setups. At very small scales, however, fabrication tolerances, such as minimum achievable channel widths, must be carefully considered.

Experimental results presented in this chapter demonstrate good agreement with the theoretical predictions. Using an effective sample volume of approximately 0.32 µL, an SNR enhancement of nearly one order of magnitude was achieved for ^{1}H NMR, accompanied by a substantial reduction in the 90° pulse length, as confirmed by nutation measurements. For nuclei with lower receptivity, namely ^{7}Li, ^{31}P, and ^{23}Na, SNR enhancements of approximately 7–8 were observed. These values are partly attributed to the use of a common, non-optimized pulse length across nuclei and to the moderate RF excitation efficiency of the single-loop saddle coil employed, compared to commercial multi-loop designs. In addition to sensitivity gains, a consistent improvement in spectral resolution by up to a factor of four was observed across all investigated nuclei, highlighting the favorable B_0 homogeneity of the S3L configuration.

The results of this chapter highlight several broader implications. By deliberately trading sensitive volume for enhanced local sensitivity, the S3L add-on enables targeted NMR measurements on small regions of interest, such as thin films, layered materials, or cylindrical samples including biological biopsy plugs. It has also potential as a broadband implant for *in vivo* experiments.

Table 3.2: *Pulse parameters for ^{13}C NMR with ^{1}H Decoupling.*

Parameters	Values
RF power	25 W
90° flip angle pulse length	10 µs
Number of scans	128
Decoupling power	0.7 W
Decoupling length	90 µs
Recycle delay D_1	1 s
δ=D_1-100 msδ	900 ms

Table 3.3: *Pulse parameter for ^{1}H–^{13}C HSQC.*

Parameters	Values
^{1}H RF power	20 W
^{1}H 90° flip angle pulse length	6 µs
Number of data points in FID	4096
^{13}C RF power	25 W
^{13}C 90° flip angle pulse length	10 µs
Number of data points in FID	512
Decoupling power	0.5 W
Decoupling length	70 µs
Number of scans	8
J-coupling constant (J)	145 Hz
$\tau = (4J)^{-1}$	1.72 ms
Increment delay D_0	3 µs

Moreover, the broadband response of the S3L, from 125.76 MHz to 500 MHz at 11.7 T, covers most nuclei of practical relevance, making it well suited for multinuclear and frequency-flexible experiments. The excitation coil possesses a tunable resonance frequency, which can be disturbed by the inserted stripline chip. Depending on the adjustment range of the capacitors on the probe, it could possibly happen that the tuning and matching condition is not perfectly reached when the S3L add-on is loaded. In such case, the coil reflects more power and has a lower quality factor, leading to a longer excitation pulse length for a given power and worse sensitivity. In our design, the total terminal resistance is however far smaller than 50 Ω, so that it could be rematched. the terminal inductance change remained within 5%, thus any detuning could be easily compensated on the probe.

Beyond the demonstrations presented here, the ability of the Lenz lens to spatially redirect and confine the B_1 field opens avenues for future applications. In particular, systems that are otherwise difficult to excite due to electrical shielding, such as battery cells with metallic current collectors, could benefit from the flipped and localized RF field generated by the S3L. This makes the stripline Lenz lens add-on a promising platform for non-invasive, in-situ NMR studies of electrochemical and other technically relevant materials.

Overall, this chapter establishes the S3L add-on as a versatile, broadband, and experimentally

practical approach to sensitivity enhancement in micro-scale NMR, forming a key building block for the methodologies developed in this thesis.

Chapter 4

LTCC-based Broadband Double-Channel Spiral Detector

The contents of this chapter are based on the author's contribution to the material published in the article [J2]. **Material from: Liang, Jianyi *et al.*, Split spiral broadband double channel NMR detector facilitated by LTCC technology, Scientific Reports, published in 2025, Springer Nature.**

4.1 Introduction

To achieve the expected optimal performance, micro coils require higher fabrication accuracy and are limited to specific building materials. Therefore, multiple microfabrication techniques have been developed for both volume and planar coils, as reviewed in **Background Information** Sec. 2.5.2.

The fabrication process often includes creating an adjacent sample chamber or channel, as an effective RF field is generated close to the micro coil at a sub-cm scale. Glass wafers are widely used as coil substrates with sample channels, because they are non-conductive and do not induce eddy currents. Commercially, glass wafers are available with various thicknesses, roughly ranging from 25 µm to 500 µm, however they are mechanically fragile, and wafer cracks can occur at any step of the fabrication process. This makes processes such as stacking and bonding of glass wafers, for example in order to integrate detector coils with micro-fluidics, rather challenging. Additionally, creating structures with sufficient thickness through etching and deposition is difficult. These disadvantages of glass-based coils were also encountered in the work described in the previous chapter, and were mitigated through careful design optimization and process control.

As a result, low-temperature cofired ceramic (LTCC) technology has garnered our attention. LTCCs are sintered from laminated glass-ceramic green tapes, allowing for mechanical structuring, conductor printing on each layer, and through-layer connections. The term "low temperature" refers to sintering processes below 900 °C. This technology provides a multilayer package

with various embedded electrical components, such as resistors and resonators [175, 176]. Notably, the substrate material has a low dielectric loss (a loss tangent < 0.002 at 10 GHz for Ferro A6, for example), making it suitable for designing sensors and microwave devices [177, 178]. Open or closed cavities and cantilevers can be engineered with high mechanical strength, high temperature tolerance, and a fabrication resolution down to 10 µm [176, 179]. These mechanical structures can serve as fluidic systems and micropumps, among other applications. In terms of NMR applications, LTCC technology was first introduced by Krivic with LTCC-based micro spiral and solenoid coil, though its full potential has yet to be fully explored [68, 180].

An NMR coil is typically attached to an external tuning and matching circuit that has the role of tuning the resonance frequency of the detector to the Larmor frequency of interest, and ensures impedance matching with a cable, which is described in Sec. 2.4.3. To facilitate the simultaneous detection of different nuclei with high efficiency, multiple-resonance micro coils with corresponding circuits have been developed [34, 133, 181, 182, 183]. For example, a single coil equipped with a triple resonance circuit for the simultaneous detection of ^{1}H, ^{2}H, and ^{13}C was reported [133]. It is noted that the fine-tuning and matching circuit increases the complexity and cost of building a probe, and also adds to the workload during measurements and daily maintenance.

Instead of using a collection of coils for specific resonance combinations, a broadband coil can cover a wide detection range despite offering moderate sensitivity. It allows researchers to switch observation frequencies instantaneously via software rather than manual hardware adjustments. By prioritizing this robust, broadband versatility, the non-resonant probe enables operando experiments in dynamic or multi-nuclear experiments that are previously unfeasible due to the rigidity of resonant hardware. Taking correlated experiment with NMR and synchrotron-based X-ray spectroscopy as an example [148], the requirement for multi-nuclear information during rapid transient processes and system robustness outweigh the marginal loss in peak sensitivity. The first attempts at broadband NMR probes involved using transmission line coils [138, 139, 140]. In the last decade, several broadband micro detectors have been developed and have proven their functionality in high-resolution, high-field NMR [84, 137]. These studies have often employed planar spiral geometries, which were previously less favored for resonant detectors. While planar spirals have lower RF field homogeneity compared to solenoid and saddle coils, they offer advantages in coil geometry manipulation, easy fabrication, and flexible integration with microfluidic chips [50, 84, 85, 137, 146]. A common feature of these two spiral coils is that they are neither tuned nor matched, but are directly connected to the coaxial cable, differing from those transmission line probes mentioned earlier. Broadband NMR detector fabricated through LTCC is a very promising candidate under extreme environmental constraints that render conventional tuned probes impractical, e.g., high pressure, high temperature, static field distortions or mechanical vibrations [184, 185, 186].

In this chapter, we present an untuned, unmatched, double-port spiral coil design, fabricated using LTCC technology. Introducing a relatively simple but effective modification of the classical spiral geometry, i.e., by splitting the spiral into two segments, we improve sensitivity in two

specific frequency ranges for broadband detection. In the first section, we present simulations of the electrical characteristics of the planar spiral geometry and B_1 field optimization. This is followed by the fabrication of a series of chip devices thinner than 700 µm with an embedded 300 µm high sample channel owing to LTCC technology. We evaluate the fabricated structures and the electrical performance of the LTCC-based detectors. Finally, we report the capability of multinuclear 1D NMR with four different isotopes, as well as ^{1}H-^{13}C 2D NMR with a heteronuclear single-quantum correlation (HSQC) experiment in an 11.7 T magnetic field.

4.2 LTCC fabricaiton process

LTCC technology has originally emerged as a robust alternative to silicon-based microsystems, particularly when structural sizes exceed 50 µm [176]. Unlike traditional thin-film or silicon-based fabrication, LTCC allows for the independent processing of multiple layers before they are laminated and sintered. It provides high mechanical load capacity and simplified packaging. The standard fabrication process is characterized by its "layer-by-layer" approach, allowing for the integration of complex 3D internal structures.

As shown in Fig. 4.1, the typical LTCC fabrication process involves several key steps starting from the raw material, i.e., non-sintered green tapes. Green tapes are flexible sheets made of ceramic powder, glass frit, and organic binders. Based on the layout of different layers, features such as vias or mechanical structures are formed using laser cutting, punching, or cutting. Horizontal circuit patterns, such conductive traces, electrodes, or the micro cois used in this work are applied to the surface of each individual layer using screen printing. This method also allows for the deposition of relatively thick conductive layers, which is beneficial for reducing electrical resistance in sensors. After the functional patterns are printed, the individual layers are precisely aligned and stacked. The stack is then subjected to heat and pressure, either isostatic or uniaxial—to fuse them into a single monolithic body [187]. The laminated stack is cofired at a temperature typically below 900 °C °, which burns out organic binder and then densifies the ceramic stack. After cofiring, additional film components can be deposited on the top and bottom surfaces and additional. This process creates a chemically resistant, and mechanically strong ceramic substrate. After fundamental electrical and mechanical test of the modules, the LTCC board is cut into individual functional pieces using dicing saw or laser cutting.

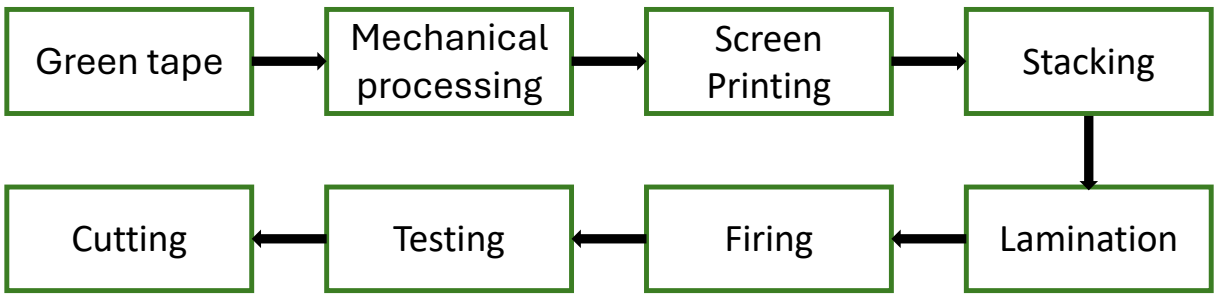

Figure 4.1: *Standard LTCC fabrication process flow.*

4.3 Resonance behavior of spiral coils

4.3.1 FEM simulation settings

COMSOL Multiphysics 6.1 and 6.2 (COMSOL AB, Sweden) were employed with the RF module (Electromagnetic Waves, Frequency Domain) for evaluating the resonance conditions and RF fields of the spiral coils, and optimizing the detector geometry.

The design rules for the devices presented in this manuscript were derived from the materials and process parameters for the LTCC materials released by the manufacturing company (VIA Electronic GmbH, Thuringia, Germany) [188]. We selected the DuPont 951 series for our coil fabrication, since this provided relatively thin-fired LTCC layers (down to ca. 45 µm), thus allowing for more design flexibility in case of multi-level devices. The loss tangent was also relatively low at 0.0063, which was around one-fifth of that for FR4, a widely used PCB substrate. The relative permittivity of 7.85 was among the highest for LTCC materials, providing a good quality factor. The relative permittivity change versus frequency was below 1.6% at a working frequency up to 10 GHz, which was around 5 times less than FR4. The LTCC thermal conductivity of $4\,\mathrm{W\,m^{-1}\,K^{-1}}$ was also one order of magnitude higher than that of FR4. The conductor pattern in LTCC, either in Au or Ag, had a rectangular cross-section defined by stencil or screen printing. The qualified minimum width of conductor lines and spaces was 100 µm, which was adopted in the designs above. The inner radius of the spirals was set to be 250 µm.

The coil was connected to a lumped port with a 1 A current source. The whole structure was located in a 19×15 mm^2 frame, simulating an NMR chip inside a cylindrical probe chamber, as shown in Fig. 4.4 (a). The sample in the simulation was assigned as water, as it is one of the most common solvents used in liquid NMR.

The results were processed and illustrated in MATLAB for Fig. 4.3, 4.4, 4.5 and 4.6. The basic processing manuscript is explained in **Appendix** Sec. A3.

4.3.2 Split spiral design and optimization

The planar spiral coil has been one of the first micro coil geometries used as an NMR detector [82, 84, 189, 190] due to its ease of fabrication and versatility. The impedance and the resonance frequency of the planar spiral coil can be easily tuned by modifying the number of turns, cross-sectional area of the metal track, loop spacing, and conductor material [84]. It has been shown that such a detector can be successfully used as a broadband detector, albeit with a certain trade-off [84, 85]. In a previous review [128], we have outlined that the frequency range between $\gamma = 0.73$ MHz per Tesla (^{197}Au) and $\gamma = 16.5$ MHz per Tesla (^{7}Li) of static magnetic field strength, covers the NMR frequencies of 94% of all active nuclei, whereas the two high-gamma nuclei, ^{1}H and ^{19}F, very relevant for a wide range of applications, are relatively well separated in frequency with $\gamma = 40.08$ MHz per Tesla and $\gamma = 42.58$ MHz per Tesla of static magnetic field strength, respectively. In order to address these two frequency bands in a single broadband detector, we present a subtle modification of the simple one port planar spiral geometry that

involves an additional contact along the spiral track, thus transforming the same device into a two-port detector. The concept is presented schematically in Fig. 4.2 for a 12-turn planar spiral with an additional contact added after 4 turns. We will denote such a structure as a **4/12** turn two-port detector. The goal of this modification is to use the inner (shorter) spiral to detect high gamma nuclei, whereas the full spiral is used for the low gamma nuclei.

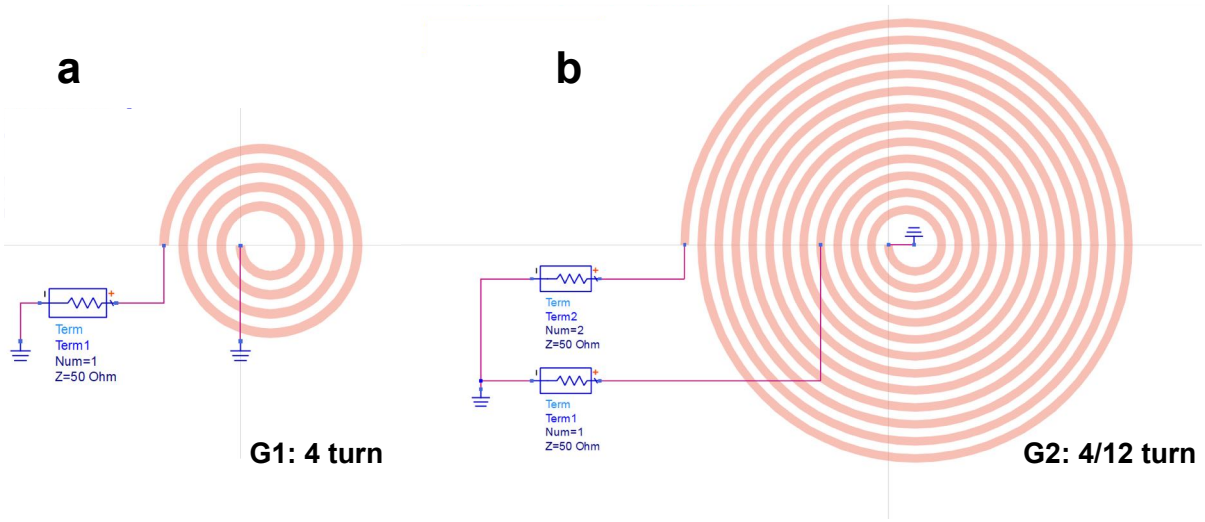

Figure 4.2: *The two spiral models built with the Advanced Design System (a) with a single port at 4 turns, and (b) with two ports at 4 and 12 turns, respectively referred to as **G1** and **G2** in this work. The spiral model is set to be* 100 µm *in width as well as spacing, and* 10 µm *in height. The frequency was swept over* 0 GHz *to* 2 GHz*. Reproduced from the author's own publication **J2** with the permission from Springer Nature.*

4.3.3 Spiral resonator on LTCC substrate

The electrical behavior of a spiral resonator built on the LTCC substrate was investigated by conducting a parametric simulation (COMSOL Multiphysics 6.1, Comsol Multiphysics GmbH, Germany) by sweeping the turn number and comparing the frequency and impedance differences.

The example of simulation model illustrated in Fig. 4.3 consists of an embedded G1 spiral with 9 turns and a centered via connected to a lumped port with 1 A. A serial simulation of the single channel G1 coil was run with a varying turn number n ranging from 3 to 14. The results are shown in Fig. 4.3 (a) and (b). Fig. 4.3 is consolidating a straightforward and well-known result: the behavior of the real and imaginary part of the planar spiral coil impedance as a function of the number of turns, showing that the resonance frequency decreases with increasing the number of turns. The position of the resonance peak exceeds the upper limit of the simulated range of 4 GHz for spirals with $n = 3 - 5$ turns, as shown in Fig. 4.3 (a), while the 6-turn spiral resonates at around 2.4 GHz. The 14-turn G1 spiral has a primary resonance at around 500 MHz. As reported by Anders and Velders [136], the reactance as the imaginary part of the impedance is almost flat up to around a quarter of the resonance frequency. Thus, a spiral with less than 14 turns in our simulation can ideally detect signals up to 125 MHz while a spiral with less than 12

turns is suitable for 500 MHz. The assumption is based on the result with a spiral alone and is modified with a more complete chip structure design [78].

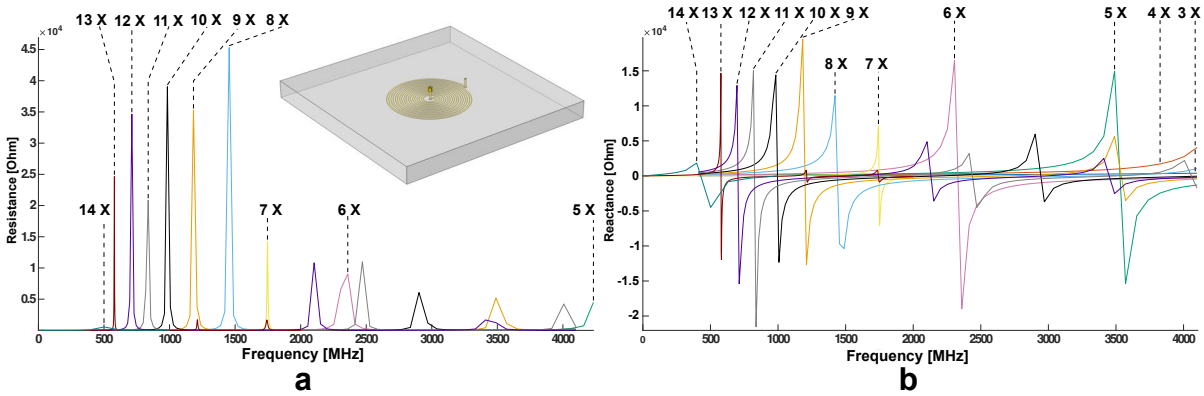

Figure 4.3: *Computational results of the (a) real, and (b) imaginary parts of the impedance for a single-port G1 spiral with a varying turn number from 3 to 14. Each curve is labeled with the turn number at the first resonance peak. It is noted that the resistances of 3 and 4-turn coils are relatively low at this frequency range and not labeled in (a). Reproduced from the author's own publication **J2** with the permission from Springer Nature.*

4.3.4 Optimization of the detector geometry

In this section, we look into the NMR-related characterization of the spiral coils, and optimize the coil geometry towards a high sensitivity and field homogeneity. Davoodi *et al.* built a framework for engineering broadband NMR detectors where two main figures of merits, excitation efficiency and signal-to-noise ratio (SNR), were introduced to evaluate the coil performance at different tuning/matching conditions [84]. We utilized COMSOL Multiphysics to study explicitly the magnetic field distribution of the spiral coils on LTCC substrates.

The effect of the LTCC substrate on the magnetic field distribution is of vital importance in this study, which is enabled by the comprehensive building material assignment in COMSOL. The LTCC substrate is defined with relative permittivity $\epsilon_{\mathrm{rel}} = 7.85$, relative permeability $\xi_{\mathrm{rel}} = 1$, thermal conductivity $\kappa = 4\,\mathrm{W\,m^{-1}\,K^{-1}}$, Young's modulus $E = 120\,\mathrm{GPa}$, and loss tangent $\tan\delta = 0.006$, according to the fabrication specification. The spiral and tracks were set to be solid gold.

The embedded coil was connected to conductive pads via through-layer gold vias with a diameter of 150 µm as shown in Fig. 4.4 (a). A lumped port was added to provide a 1 A source to the coil.

The simulated nutation spectra for $n = 2 - 15$ at three frequencies are presented in Fig. 4.4 (b) to (d) and further processed for a group of figures of merit in (e) to (h). Fig. 4.4 (e) shows that a higher turn number requires a longer pulse length to realize a 90° flip angle, i.e., more power from the probe, and the power consumption is inversely related to the frequency. The average B_1 field in Fig. 4.4 (f) shows that the field strength benefits from a larger turn number at a low-frequency band, while at 500 MHz it reaches a maximum at $n = 10$ since the coil is

close to resonance. The sensitivity in Fig. 4.4 (g) is evaluated as the ratio to a field strength and the square root of the applied power, and the optimal sensitivity is reached by $n = 5$ at all three frequencies. It is noted that the signal region (1000 µm in diameter) for the sensitivity calculation remains the same for consistent comparison and thus the filling factor is almost 1 for $n < 6$. As the turn number increases, 150 MHz outperforms the other two frequencies, and the sensitivity difference between 150 MHz and the other two gets larger due to a lower filling factor. Fig. 4.4 (h) presents the B_1 field homogeneity normalized with respect to the maximum value for convenient comparison. The RF-homogeneity is calculated by the ratio of the nutation signal amplitudes at 450° and 90°. By increasing the turn number, the B_1 field homogeneity for a fixed sample space is enhanced, and shows little difference between low and high-frequency bands before $n < 10$. From the nutation, the spiral is no longer an effective RF resonator when $n > 10$, but the damping becomes less, making the field homogeneity even higher. Considering these results, we identified 5-turn with the highest sensitivity, and 10-turns as a critical length reaching close to proton resonance, thus selecting the **5/10** G2 spiral for subsequent fabrication and measurement.

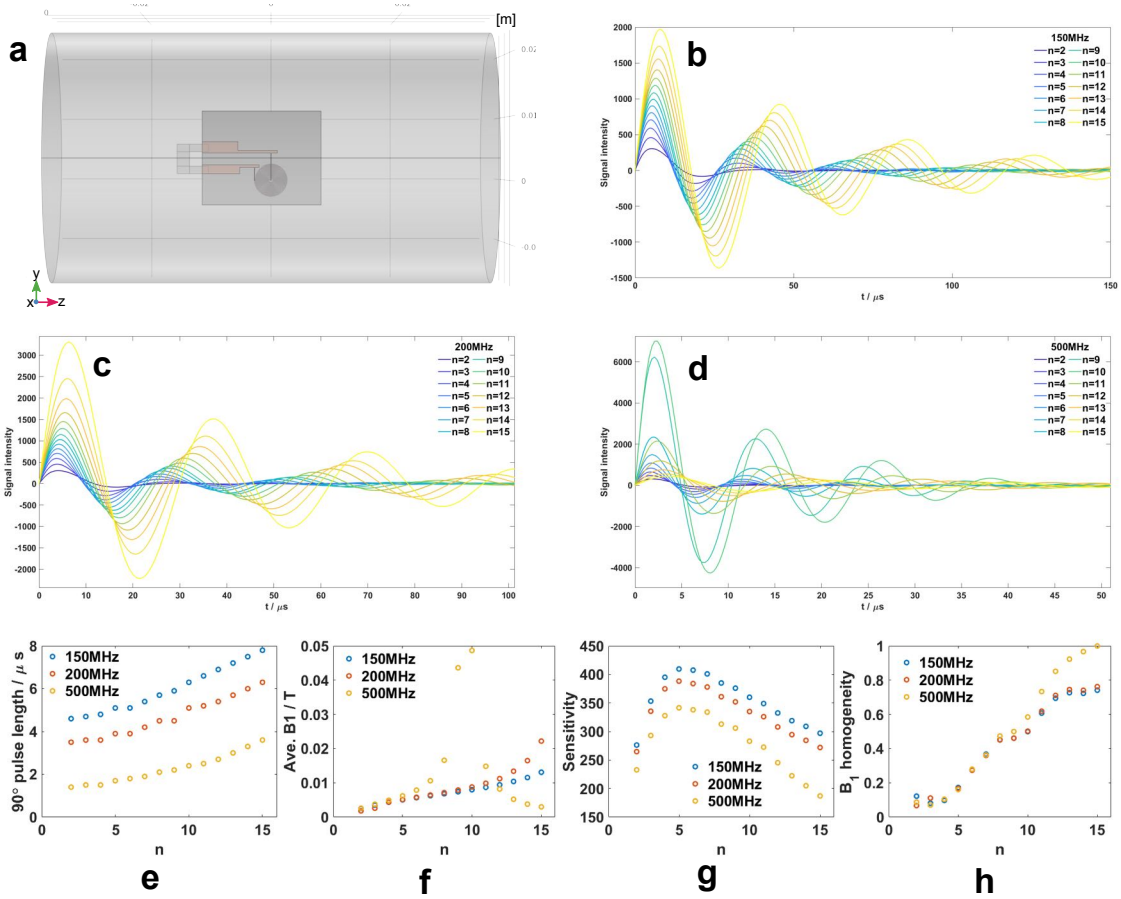

Figure 4.4: *(a) Top view of the chip placed at the center of a tube. The conductor structure, including the spiral, is highlighted in orange. (b)-(d) Simulated nutation spectra for $n \in (2, 15) \in \mathbb{Z}$ at three representative frequencies. The time axis is adjusted to reveal flip angle details around 4π. The following 4 figures are processed from the resulting nutation spectra. (e) 90° pulse length. (f) Average B_1 field strength. (g) Sensitivity. (h) B_1 field homogeneity. Reproduced from the author's own publication **J2** with the permission from Springer Nature.*

4.3.5 Resonance behavior of the optimized split coil

With the split coil geometry established, we did a detailed simulation study of the terminal impedance and the RF field distribution by the split 5/10 coil. The model was further enriched with a sample channel beneath the spiral for an increased simulation accuracy.

Fig. 4.5 compares the self-resonance condition in the inner loop of the 5/10 split coil to that in a simple 5-turn G1 coil. The current density in the coil and the B_1 field strength (normal to the spiral plane) for 3 working frequencies of the G2 spiral are shown in Fig. 4.6.

The mesh distributions for two coil models were individually optimized to enhance the simulation precision and to decrease the computation time, as illustrated in Fig. 4.5. With the complete chip stack, the self-resonance is decreased due to a higher parasitic capacitance between the substrate and the coil, as the 5-turn G1 spiral presents a self-resonance at 1000 MHz, and the inner 5-turn spiral of the G2 coil resonates at around 900 MHz, which is around one-third of the resonance frequency of a pure G1 spiral without adding any tracks and pads, as displayed in Fig. 4.3. The resistances at 500 MHz are respectively 6.0 Ω and 5.1 Ω, which creates a similar matching condition with the signal cable.

With the inner port being connected to the 1 A current source and the outer port let as an open circuit, the average current density was lower at the respective frequencies in comparison with the full loop case of a G1 spiral, and the average B_1 field strength level at the sample region was also lower, as shown in Fig. 4.6 (a) and (b). Fig. 4.6 (a) shows the increasing inductive coupling of the outer turns of the 5/10 G2 spiral with the inner, i.e., active turns. This becomes clear in the simulation for 500 MHz. This accounts for the lower self-resonance in Fig. 4.5 (b). When the outer port was connected to the source, as proven in previous studies[83, 190], the current was more focused in the central segment of the spiral and generated a more homogeneous field with a higher field strength in the sample channel region. Comparing three frequencies, the spiral exhibited the highest excitation efficiency at 200 MHz, which was beneficial to the application since the full loop should serve a low-frequency range.

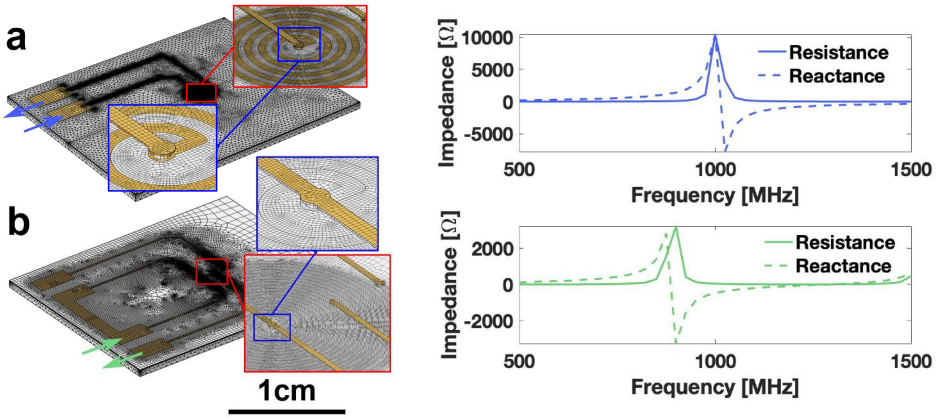

Figure 4.5: *(a) Meshed G1-type single 5-turn chip finite element model consisting of ca. 1031k elements and 196k nodes. (b) Meshed G2-type split 5/10 spiral chip finite element model with ca. 2353k elements and 460k nodes. In each case the terminal impedance at the port varied from* 500 MHz *to* 1500 MHz. *Reproduced from the author's own publication* ***J2*** *with the permission from Springer Nature.*

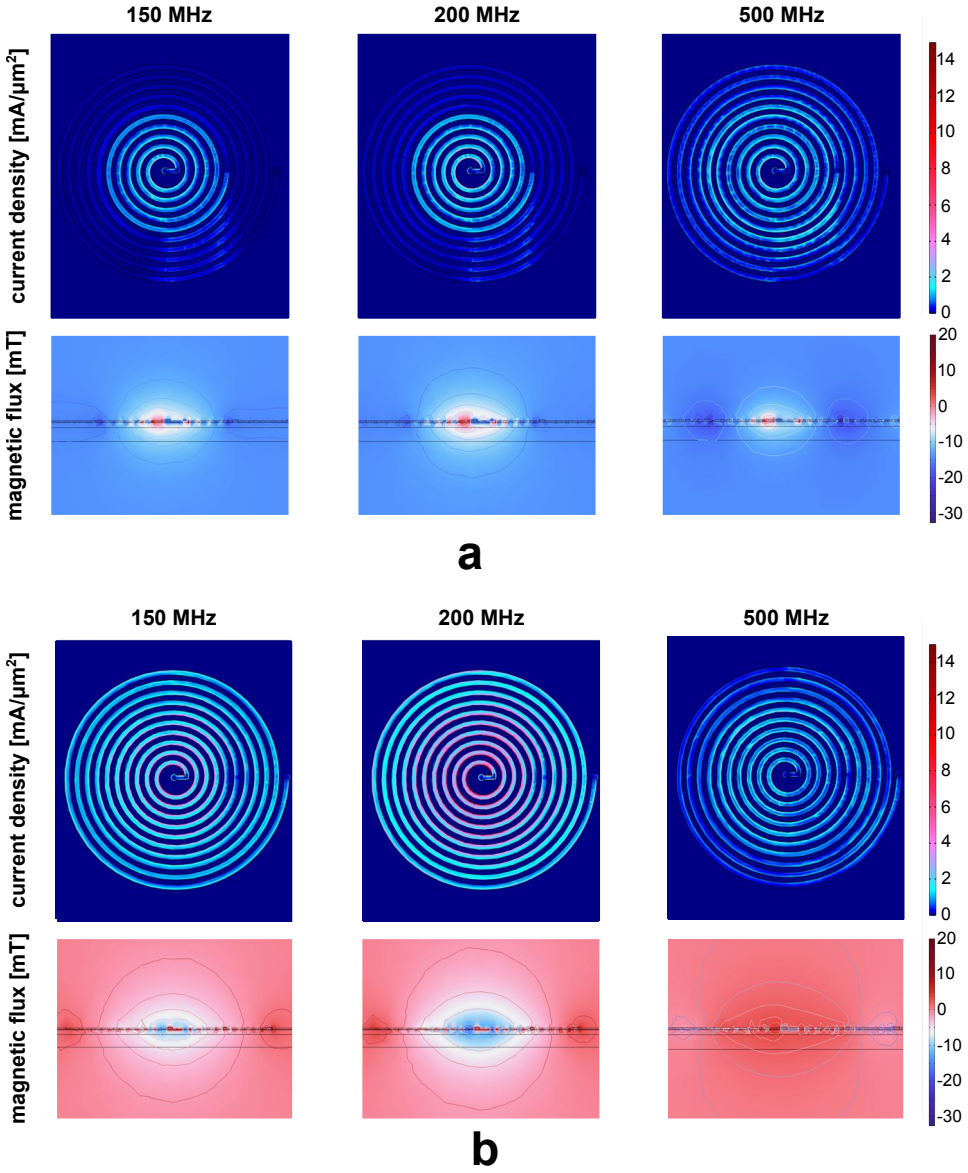

Figure 4.6: *Current density (color map) on each G2-type coil's lateral cross-section and B_1 field strength (color map and contour plot) on the transverse plane with the (a) inner port, or the (b) outer port connected to the terminal. A negative value in the field strength plot refers to a negative B_1 direction.*

4.4 Coil fabrication and characterization

4.4.1 Chip layout design

The layouts of spiral chips in the top view are shown in Fig. 4.7: the 5/10 G2 spiral based on the optimization above, the 5- and 10-turn G1 spiral for comparison, two spirals of respectively 6/14-turn G2 type and 14-turn G1 type being derived from the optimal design to verify the optimization. The layouts were plotted in LayoutEditor (Juspter GmbH, build: 20190108). The conductor tracks in pink color were printed on the top LTCC layer while the spiral track in green color were printed on the second layer from the top. The channel in teal color and the hole in brown color were cut on corresponding layers before the lamination process.

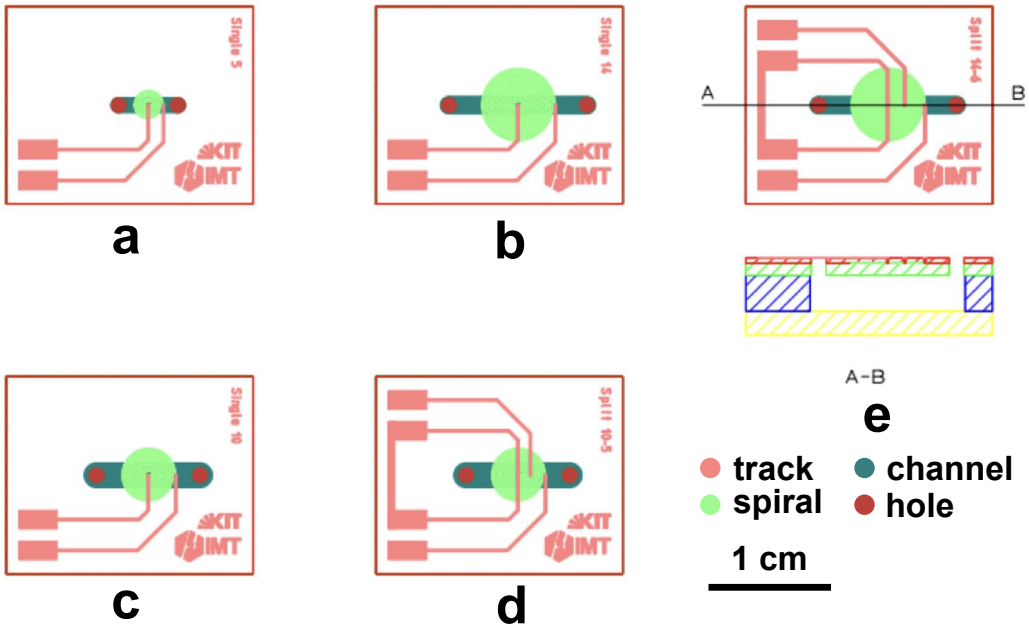

Figure 4.7: *(a) - (c) Illustrations of the G1-type chips with respectively 5-turn, 10-turn, and 14-turn spirals. The colors denote different structures (see the legend). (d)-(e) Illustrations of the G-2 type chips, split 5/10-turn and split 6/14-turn. A cross-sectional illustration of the split 6/14-turn chip is attached, consisting of four layers. For details of the layer arrangement with dimensional data, see Fig. 4.8.*

The channel dimensions of each chip variant are presented in Table 4.1 in detail. In order to have a low field distortion induced by a material boundary close to the detection region [84], the rectangular sample channel width was set to be half of the outer diameter in the 5- and 10-turn spiral, while the channel length was double the diameter. The split 5/10 spiral took up the dimensions from the 10-turn spiral. The effective sample volume V_{eff} was calculated as a box, $2r \times w \times h$ beneath the spiral layer in respective cases. The split 6/14-turn spiral chip was adjusted to have the same effective sample volume as the split 5/10 G2 spiral for an SNR comparison.

Table 4.1: *Sample channel dimensions of all broadband spiral coil chips.*

Device		**Channel width** w **[mm]**	**Channel length** l **[mm]**	**Eff. sample volume** V_{eff} **[µL]**
G1	5-turn	1.20	4.80	0.70
	10-turn	2.00	8.00	2.13
	14-turn	1.40	11.20	2.03
G2	Split 5/10-turn	2.00 2.00	8.00 8.00	0.97 (5-turn) 2.13 (10-turn)
	Split 6/14-turn	1.40 1.40	11.20 11.20	0.81 (6-turn) 2.03 (14-turn)

4.4.2 Chip fabrication based on LTCC technology

A top view of the five variants of LTCC chips being fabricated is shown in Fig. 4.8 (a).

Based on the conceptual stack arrangement in Fig. 4.7, the chips were designed in the 7-layer stack structure illustrated in Fig. 4.8 (b), where two tape thicknesses are used, respectively 43 µm and 97 µm after firing, thus the total chip thickness adds up to around 625 µm. Layer **I** is 194 µm consisting of two 97 µm tapes. The fluidic channel was patterned in the layer **II** using three 97 µm tapes. The 10 µm thick gold spiral was printed on the layer **III** and isolated from the sample channel with LTCC. On the top layer (**IV**), another 10 µm thick conductor layer was printed for conductive pads and tracks, and was connected to the spiral by through-layer vias. The via had a diameter of 150 µm. Inlets and outlets to the buried channel were cut through layer **III, IV** with a diameter of 1.2 mm. A complete layout for one batch of various chips is shown in Fig. A5 (see **Appendix** Sec. A5.3).

A cross-section image of one fabricated chip is displayed in Fig. 4.8 (c). The overall thickness was around 0.58 mm and the channel height was around 242.6 µm, which corresponds to a thickness shrinkage rate of around 8%, lower than the 15% given in the design specification. It is noticeable that the two chips with split spirals in Fig. 4.8 (a) are covered with silver material on the conductor pads, which are fired *AgPt* paste. Throughout the soldering work of the chip with the SMA connector, we found that the gold tracks were easily detached from the LTCC surface and removed when in contact with the heated soldering tips and soldering paste (up to around 350 °C). *AgPt* paste applied to the original gold proved to be an effective and robust solution.

Fig. 4.9 presents the characertization of the surface warpage on a G-2 type 6/14-turn spiral chip. In Fig. 4.9 (a), a sampling line **i** was drawn in the region between conductor tracks. The maximum height difference was around 0.99 µm, and the bump occurred close to the channel area. Fig. 4.9 (b) presented the height measurements along **ii** and **iii**. The measured height of the top LTCC surface, as denoted as X, was well controlled between the upper thickness limit

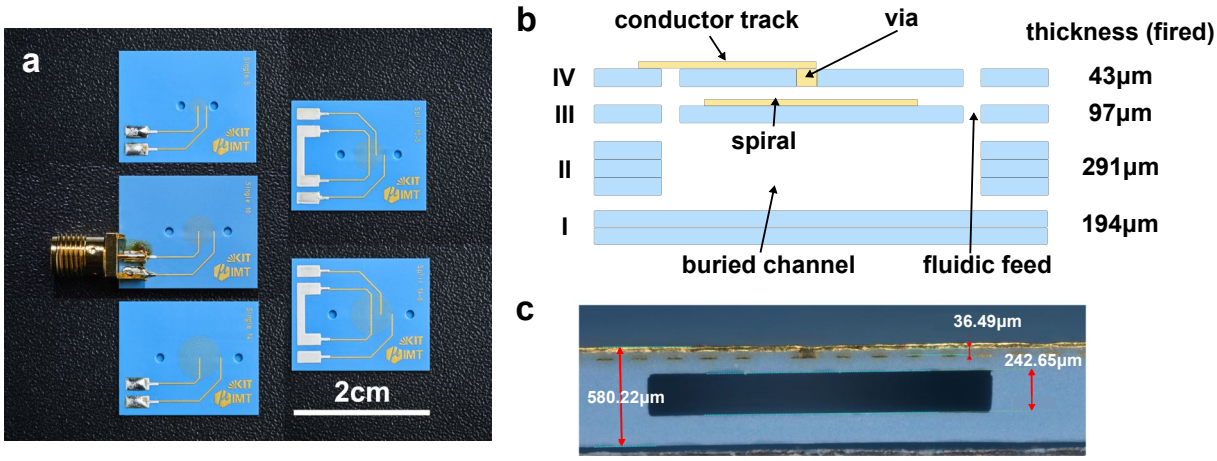

Figure 4.8: *(a) Top view of 5 chip devices. The middle device was connected to an SMA connector, for testing purposes. (b) Cross-sectional illustration of the designed low-temperature co-fired ceramic layer stack. (c) Correspondingly cut plane of a ceramic chip with annotated principal height dimensions. The dark area within the blue ceramic formed the buried microfluidic channel. Reproduced from the author's own publication* ***J2*** *with the permission from Springer Nature.*

and the lower thickness limit, and slightly smaller than the target due to the shrinkage. The surface warpage was measured to be $< 0.3\%$.

4.4.3 Electrical characterization of fabricated chips

Each fabricated chip was measured with a network analyzer to determine its impedance change, as well as the self-resonance frequency, the results being presented in Fig. 4.10. For split-spiral chips, two ports are measured independently.

The resonance frequency measured on the 5-turn, 10-, 14-turn G1 spiral is 903 MHz, 369 MHz, and 225 MHz, respectively. According to the untuned broadband chip concept, only a 5-turn spiral is ideal for the detection up to 500 MHz where the other two chips work as a capacitive component. On the split 5/10-turn spiral, the resonance frequency is 307 MHz at the outer port whereas the inner port resonance is higher than 1 GHz. This slightly higher resonance frequency of the inner port of the 5/10-turn G2 spiral than 5-turn G1 spiral can be caused by the double track from the coil center as shown in Fig. 4.8 since an additional inductor in parallel reduces the total inductance. With respect to the resistance, the inner port of the 5/10-turn chip and the 5-turn chip displayed a close result, 2 Ω/2.3 Ω at 125 MHz and 10.7 Ω/11 Ω at 500 MHz. The track length was not neglectable compared to the spiral total length, and the parallel track could also account for the slightly lower resistances on the split spiral coil. On the other hand, the outer port of the split 5/10-turn G2 spiral presented a 60 MHz lower resonance than the G1 spiral. Although the double track generated a lower inductance as discussed above, the open track at the 5th turn contributed a higher parasitic capacitance within the circuit, thus decreasing the resonance frequency. The 14-turn G1 spiral and the 6/14-turn G2 spiral showed a similar phenomenon in the resonance frequency change.

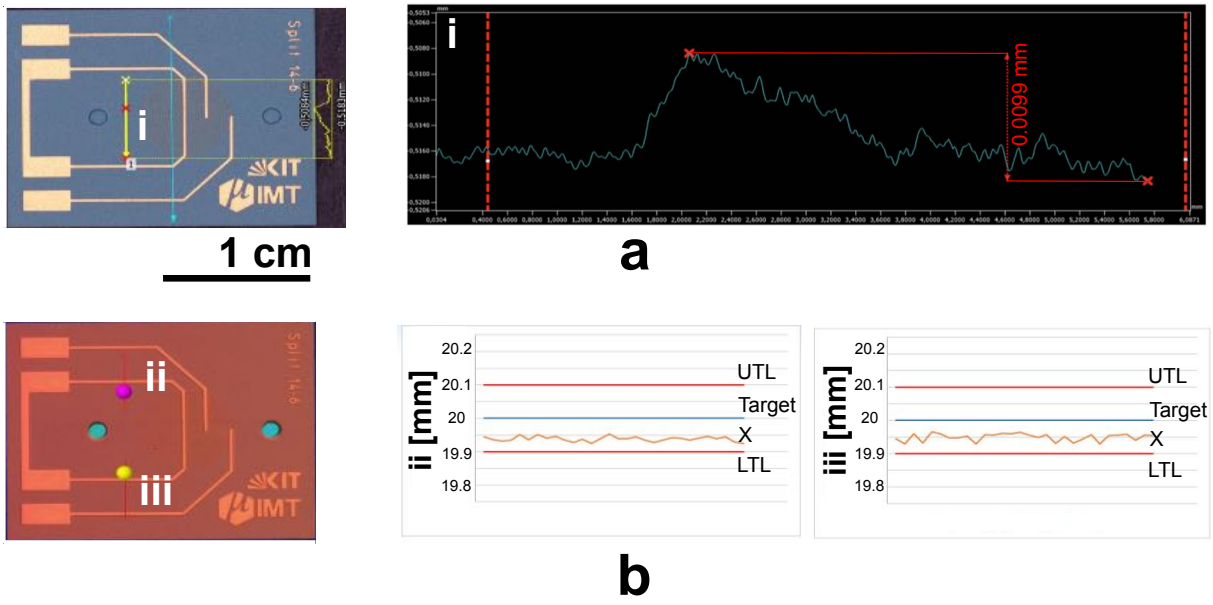

Figure 4.9: *(a) The chip thickness measurement of a G-2 type 6/14-turn spiral chip along the yellow line* ***i*** *across the channel. (b) The surface warpage characterization along* ***ii*** *and* ***iii****, across two separate pairs of conductor tracks. UTL: upper thickness limit. LTL: lower thickness limit. Target: thickness by design. X: measured thickness. The target value was calibrated to be* 20 mm *from the platform level.*

4.5 NMR setup and measurement

4.5.1 NMR characterization settings

The NMR/MRI experiments were conducted on an 11.74 T Avance III Bruker NMR system (Bruker BioSpin, Rheinstetten, Germany). The chips were fixed onto a home-built NMR probe skeleton with a 3D-printed half-cylinder supporter fitting the probe pins, which is shown in Fig. A6 with component dimensions (see **Appendix** Sec. A5.4). The chip was held vertically and loaded into the isocenter of the magnet, which was important to avoid local field gradients. The coaxial cable was guided out of the magnet to the pre-amplifier (LNA Module 500, Bruker BioSpin, Rheinstetten, Germany) through a copper tube at the center of the probe. No gradient sleeve or matching/tuning circuit were used for NMR measurements, as reported in this paper. The temperature was measured to be 30 °C from the system.

For NMR measurement operation and spectra processing, software TopSpin 3.5pl2 is applied. The pulse sequences and the measurement parameters for 1D and 2D NMR are presented with detailed explanation in Sec. **NMR spectroscopy**.

4.5.2 1D multi-nuclei NMR

In this section, we present the 1D NMR measurements with three single-port G1 chips and two double-port G2 chips in a broadband configuration. ^{1}H, ^{13}C, ^{23}Na, ^{31}P spectra were measured and presented in Fig. 4.11, covering a Larmor frequency range from 125 MHz to 500 MHz at

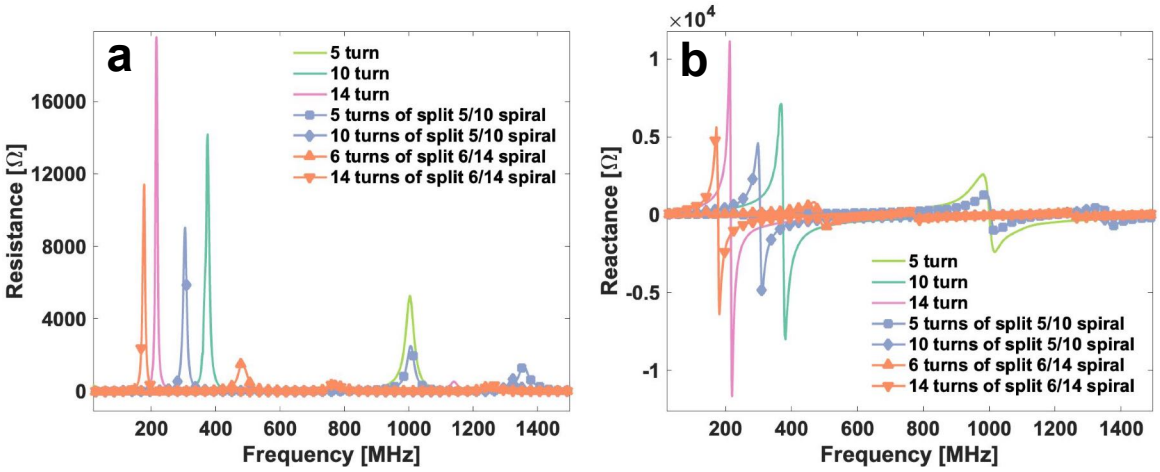

Figure 4.10: *(a) Terminal resistance R and (b) inductance L of all chips. The double-port G2 chip was measured such that each port was tested individually, while the other one was left floating. The value of each chip variation was averaged from the raw data collected from several available chip products. Reproduced from the author's own publication* ***J2*** *with the permission from Springer Nature.*

11.7 T. Detailed measurement parameters and results are presented in Table 4.2 for three G1 chips and Table 4.3 for two G2 chips, enabling further discussion in a quantitative way.

In three G1 chips, the same solution sample was loaded with 500 mM Na_2HPO_4, with 250 mM TSP dissolved in 50:50 H_2O:D_2O. The sample was injected into the channel by a syringe with a soft polymer tube. With a low roughness on the fired LTCC surface, the inlet/outlet was sealed with common laboratory tapes, and the sample was kept in the chips for a few days without leakage.

The proton signals in Fig. 4.11 (a) originated from water and TSP. The water signal peak at 4.8 ppm was picked for the SNR and linewidth calculation. The signal magnitude difference was caused by three factors: the sample volume, scan number, and the coil geometry. With the former two contributing factors deprived from the measured SNR, the 10-turn spiral showed the highest normalized limit of detection (nLOD) as 268 nmol$\sqrt{\text{s}}$ [191], i.e., the highest sensitivity among the different coil geometries, and 341 nmol$\sqrt{\text{s}}$ by the 5-turn and 989 nmol$\sqrt{\text{s}}$ by the 14-turn spiral as shown in Table 4.2. For each chip, the excitation power level and 90° pulse length documented in the table were optimized in the nutation spectrum and the required transmitted pulse increased with a higher turn number. Compensated by a larger power level, the pulse length ($\tau_{\pi/2}$) got shorter and led to a wider frequency offset from the carrier ($1/\tau_{\pi/2}$), which was advantageous in terms of measuring all signals at various chemical shifts in a broadband spectrum [52]. The 10-turn spiral also reported the lowest linewidth as 20 Hz, i.e., the best field homogeneity among three single-spiral G1 chips. Despite a high noise level, the 14-turn spiral had a 32 Hz linewidth as half of that by the 5-turn spiral. The sample was exposed to the local static field distortion at the interface between the building material and the sample. For a spiral coil with less turns and accordingly a shorter sample channel, the susceptibility mismatches became more dominant

and the linewidths were larger.

^{23}Na and ^{31}P each occurred a single peak in Fig. 4.11 (c) and (d). The maximum sensitivity for ^{23}Na and ^{31}P was realized with a 10-turn G1 spiral and a 5-turn G1 spiral respectively. While ^{1}H and ^{31}P are both spin-1/2 nuclei and thus not affected by quadrupolar relaxation, ^{23}Na is a quadrupolar nucleus (spin-3/2) and has very short T_2^*, leading to broader lines compared to ^{1}H and ^{31}P. Same as for the proton case, the 10-turn spiral provided the best B_0 field homogeneity, 33 Hz at ^{23}Na and 22 Hz at ^{31}P.

As clearly shown in Fig. 4.12, limited by its relatively low self-resonance frequency, the sensitivity loss on a 14-turn G1 spiral increased compared to the other two spiral chips as the detection frequency rose from 132.3 MHz to 500 MHz. With the same logic, the 5-turn G1 spiral was supposed to be more sensitive than the 10-turn spiral, which contradicts the data reported above. This is because of the fact that the 10-turn spiral reaches its resonance at around 500 MHz and the signal gain is enhanced. However, the narrow sensitivity gap between the self-tuned 10-turn and the broadband 5-turn spiral proves the potential of the broadband micro spiral design. Nutation spectrum of proton signal with a 10-turn spiral chip is presented in Fig. 4.13. $A_{450^\circ}/A_{90^\circ}$ was about 49%, which showed the intrinsically low field homogeneity of the planar spiral coil.

Two double-port G2 spiral chips were also tested for the 1D NMR scenario with a sample of 1 M ^{13}C-labeled D-glucose prepared in D_2O, i.e., ^{1}H from the inner port and ^{13}C from the outer port, with the results presented in Fig. 4.11 (d) and (e).

From the ^{1}H measurement parameter in Table 4.3, the inner port of the 5/10 G2 spiral required a 90° pulse of 11 µs as 10 W, which was almost twice that of the 5-turn G1 chip. This additional power consumption was caused by the energy dissipation in the outer spiral segment induced by coupling, which was shown in the previous simulation analysis in section **Resonance behavior of the optimized split coil**. nLOD data was respectively 43 nmol$\sqrt{\text{s}}$ and 59 nmol$\sqrt{\text{s}}$ by the split 10- and 14-turn spirals, i.e., a 6-8 times ^{1}H sensitivity enhancement as the single 5-turn port spiral. The split 14-turn G2 chip reported a signal linewidth of 35 Hz, which was reasonably between the resolutions of the G1-type 5-turn and 10-turn chips. The signal resolution with the 10-turn G1 spiral deteriorated to be 72 Hz, which may have been due to occasional drift of the B_0 field and an incomplete shimming during the measurement. The high noise level in ^{13}C measurements was compensated by an exponential line broadening factor of 15. The linewidth was calculated by the leftmost doublet at around 102 ppm, with the split 14-turn chip realizing a linewidth down to 74 Hz.

Based on the characterization above, the split 10-turn G1 chip was proven to have a high broadband sensitivity among the chips fabricated, and no notable degradation to the field homogeneity, while the excitation power was still within the range supplied by the electrical system. This experimental result was in good conformity with the simulation prediction and made the 10-turn G2 chip promising for subsequent 2D NMR measurements.

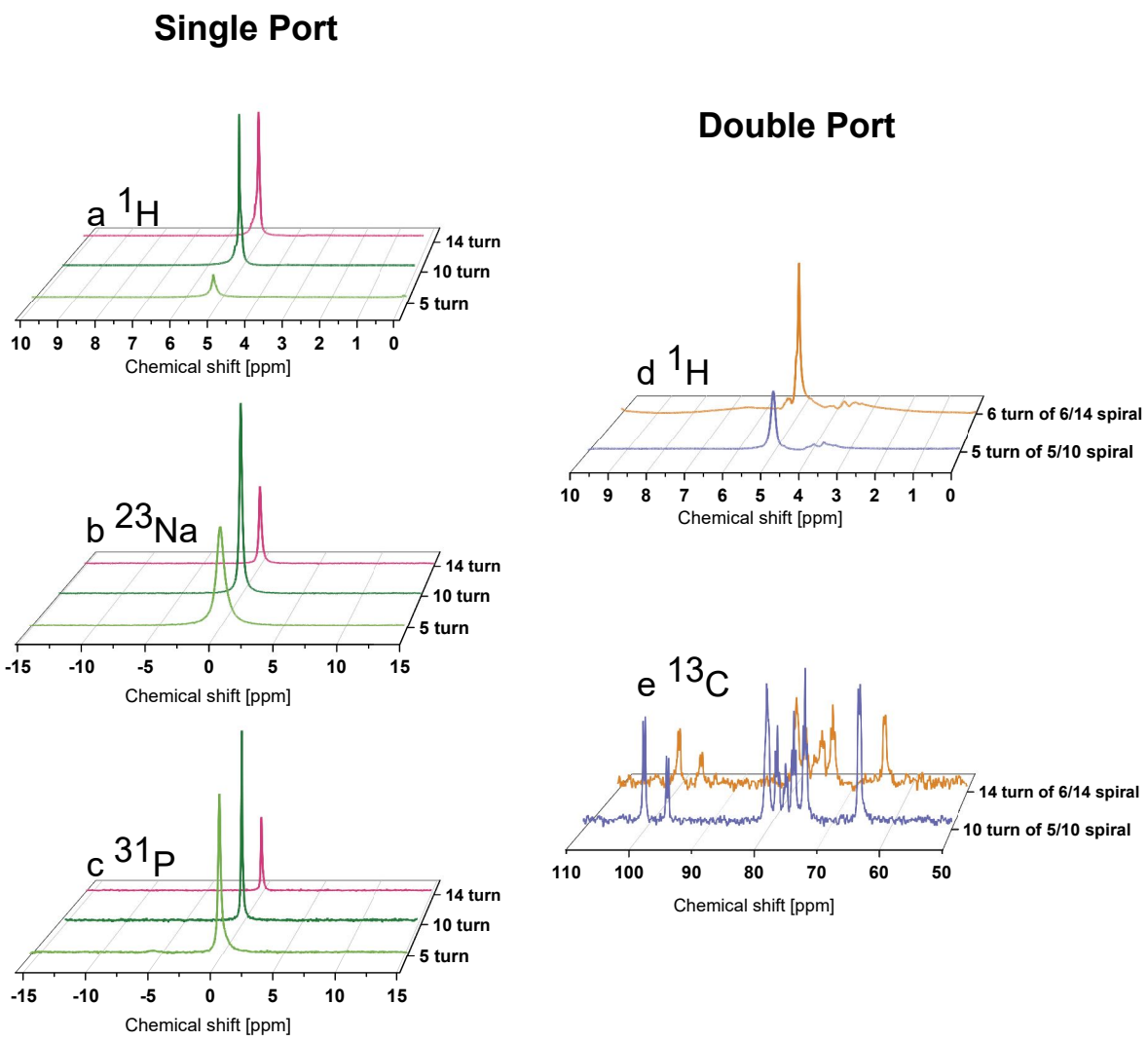

Figure 4.11: *1D NMR spectra of (a) ^{1}H, (b) ^{23}Na, (c) ^{31}P, from single-port G1 spiral chips, and of (d) ^{1}H, and (e) ^{13}C from double-port G2 spiral chips. Reproduced from the author's own publication **J2** with the permission from Springer Nature.*

4.5.3 2D HSQC NMR measurement

In this section, the split 10-turn and 14-turn G2 chips are implemented for 2D heteronuclear measurements and Fig. 4.14 shows the ^{1}H-^{13}C HSQC (Heteronuclear Single-Quantum Correlation) spectra obtained with 1 mol dm^{-3} ^{13}C labeled D-Glucose dissolved in 10:90 H_2O/D_2O.

The split 10-turn G2 chip provided better sensitivity in the 2D figure than the 14-turn G2 chip comparing Fig. 4.14 (a) and (b), which is consistent with the 1D NMR results. According to the optimization process, the split 10-turn G2 chip is an optimum design, while the 14-turn G2 chip, as a variant from the optimum variant, was built alongside this batch as a reference. As a result, the 14-turn G2 chip presented a lower sharpness at the closely spaced carbon signals ranging from 2.8 ppm to 3.7 ppm along the F2 axis (C2/C4 and C3/C5 group when referring to the glucose structure) [192, 193]. In both figures, the cross-peaks at around 96 ppm/4.8 ppm and

Table 4.2: *NMR broadband measurement at frequencies of different nuclei with single-port G1 chips.*

Device	**5-turn**			**10-turn**			**14-turn**		
Isotopes	**^{1}H**	**^{23}Na**	**^{31}P**	**^{1}H**	**^{23}Na**	**^{31}P**	**^{1}H**	**^{23}Na**	**^{31}P**
Power(watt)	5	10	10	10	20	20	10	25	25
Pulse length(µs)	12	18	15	25	35	20	60	65	50
Number of scans	8	1024	2048	512	128	2048	128	1024	2048
Relaxation delay(s)	10	0.1	5	10	0.1	5	10	0.1	5
Linewidth(Hz)	64	98	50	20	33	22	32	33	34
Measured SNR	703	145	166	13590	527	244	2775	256	150
nLOD ($\mathrm{nmol}\sqrt{\mathrm{s}}$)	**341**	**169**	**120**	**268**	**121**	**214**	**989**	**238**	**378**

100 ppm/4.3 ppm on the F1/F2 dimension were clearly resolved, which showed a good separation of the anomeric carbon signals between the β-D-glucose and α-glucose, as the main research target of analyzing glucose samples. It demonstrates the capability of the double-port spiral design to be used in molecular structure studies [194]. However, a successful readout of correlated dense ^{1}H peaks from closely spaced carbon peaks requires a higher spectral resolution than the current experimental setup .

Two types of pulse sequences were used in the measurement, ^{1}H-decoupled ^{13}C detection, and ^{1}H-^{13}C HSQC as illustrated in Fig. 4.14 (c) [J1]. The pulse parameters for the experiments are summarized in Table 4.4. The ^{1}H (F2 dimension) and ^{13}C (F1 dimension) sweep widths were 10 ppm and 150 ppm, respectively. In terms of the line broadening factor, we obtained 5 Hz for F1 and 10 Hz for F2.

4.6 Conclusion

Facing the challenge of expensive and complicated hardware in NMR systems, the untuned and unmatched planar spiral design is cost-effective and easy to use in conjunction with a flow-arrangement. Without the typical signal processing excitation/reception on a commercial probe, a simple single-port spiral chip, being connected to the system pre-amplifier directly, achieved a sensitivity down to 120 $\mathrm{nmol}\sqrt{\mathrm{s}}$ as shown in this work. Furthermore, a double-port spiral design was introduced featuring two favored detection ranges, which enhanced the sensitivity of the proton measurement by a factor of 6, and was capable of 2D NMR measurements for a wider application than a typical spiral detector.

Table 4.3: *NMR measurement of ^{1}H and ^{13}C with double-port G2 chips. Also see Fig. 4.11.*

Device	**10-turn**		**14-turn**	
Port	inner # 5	outer # 10	inner # 6	outer # 14
Isotope	**^{1}H**	**^{13}C**	**^{1}H**	**^{13}C**
Power (watt)	10	30	10	25
Pulse length (µs)	11	25	11	37
Number of scans	32	128	128	128
Relaxation delay (s)	10	1	10	1
Linewidth (Hz)	72	80	35	74
Measured SNR	1563	21	2664	11
nLOD ($\text{nmol}\sqrt{\text{s}}$)	**43**	**1329**	**59**	**1790**

The main challenge of using a micro spiral coil turned out to be the low spectral resolution. The susceptibility mismatch at the interfaces along the static magnetic field direction caused a field distortion, which should be considered when constructing the detector geometry [63, 195]. One simple solution to avoid the mismatch is to move the sample interface away from the coil region, which would inevitably lead to a higher dead sample volume. Another possible reason for the susceptibility mismatch in LTCC chips is the variation of layer thickness and a distorted planarity after firing of LTCC. Symmetric stack design and batch fabrication should be prioritized to avoid severe surface tension difference between top and bottom surfaces. At the same time, the B_1 homogeneity is of prime importance for the spiral to function as a transmit/receive coil [136]. In our case, the inner loop within a split spiral also recorded the signals from the vicinity of the outer windings. The field uniformity can be improved with a square spiral design and variant turn spacing adjustment [82, 83]. One promising direction is to configure the split spiral coil as a TX/RX coil, with the outer loop as the transmitter and the inner loop as the receiver. It could offer potential benefits in tailoring B_1 field distribution and optimizing sensitivity for multi-nuclear applications.

Low temperature co-fired ceramics (also denoted as LTCC), as a low-loss substrate material, improved the efficiency and robustness of the coil and sample handling with its high mechanical strength and chemical resistance. It also provides high design flexibility with multi-layer conductor structuring and an integrated microfluidic channel. Despite the limitation on minimal conductor width/spacing for printed structures on the LTCC board, as well as layer thickness limitations, an NMR coil based on the LTCC board can be integrated into a miniaturized spectrometer for most micro scale applications. LTCC substrates have dielectric parameters depen-

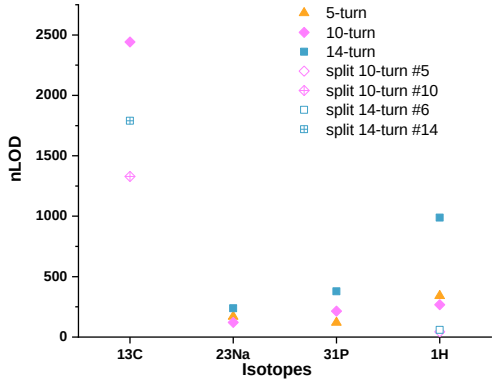

Figure 4.12: *Comparison of nLOD of 1D NMR measurements with various chips.*

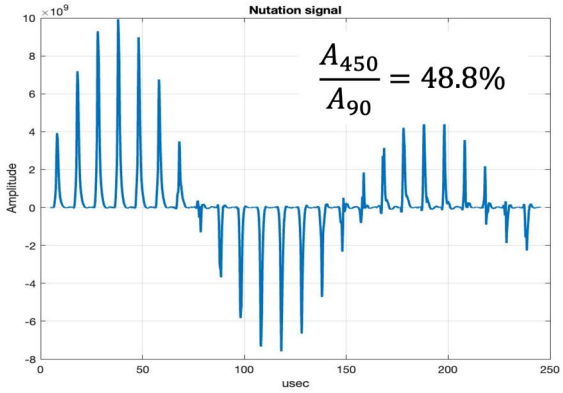

Figure 4.13: *Nutation spectrum of proton signal with a 10-turn spiral chip.*

dent on the different recipes for the ceramic compounds, and more LTCC series are emerging [178]. The substrate selection should be guided by the specific application requirements.

In this work, we developed a series of single-port and double-port spiral detectors fabricated using the LTCC technology. The successful execution of both 1D and 2D NMR measurements with a double-port spiral detector demonstrated the effectiveness of this detector design, which extends the application scope of the long-existing planar spiral geometry in NMR detection. This broadband detector design eliminates the hurdle of tedious manual retuning for instantaneous frequency switching across multiple isotopes, and presents a highly robust system under strict experimental constraints. With the discussion above, we envision a great potential of the LTCC-based split spiral device in the application to multi-FID detection and in combination with a flow set up [196, 197].

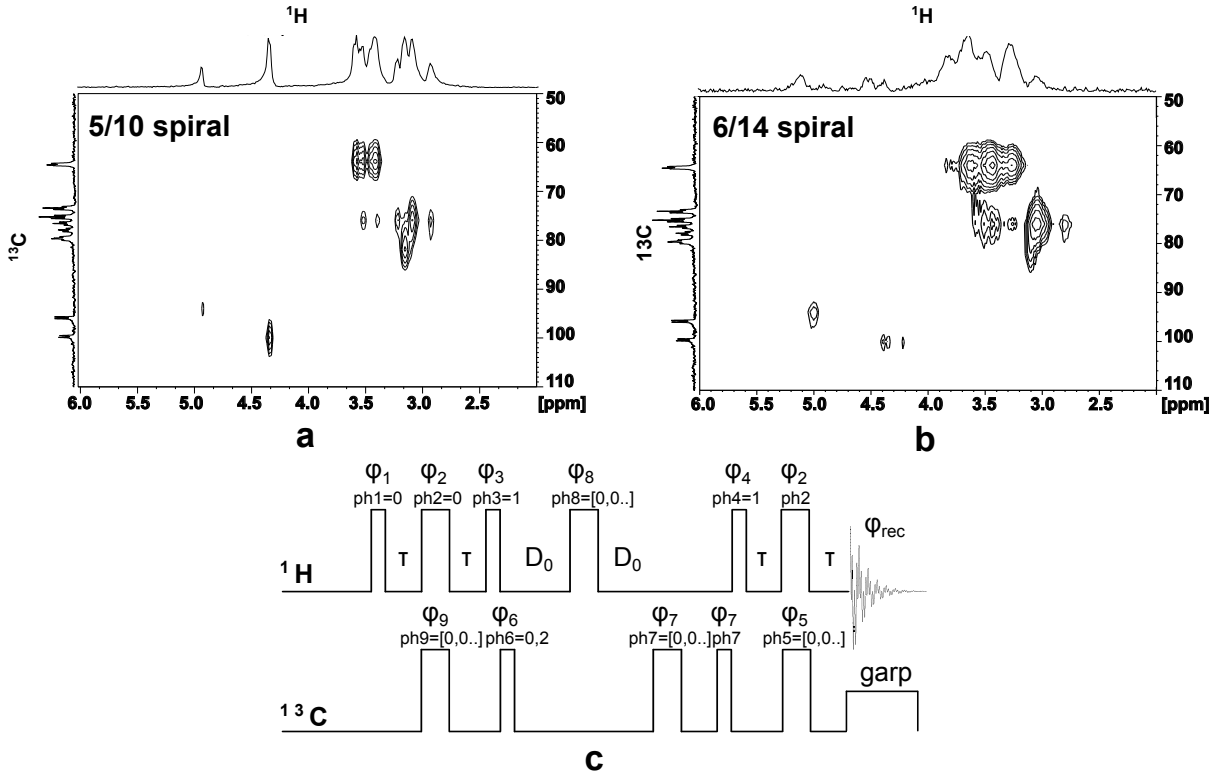

Figure 4.14: *^{1}H-^{13}C HSQC spectra from G2-type (a) 5/10 turn and (b) 6/14 turn chips, with y-axis representing frequency shift in ^{13}C, and x-axis representing frequency shift in ^{1}H. The required NMR pulse sequences for the two RF channels are shown in (c), with T and D_0 denoting delays, the ϕ_i's refer to the phase angle of each applied RF pulse, and a globally optimized alternating phase "garp" decoupled the carbon during proton acquisition. The different pulse parameters applied for two chip are shown in Table 4.4. Reproduced from the author's own publication **J2** with the permission from Springer Nature.*

Table 4.4: *Pulse parameters for ^{1}H–^{13}C HSQC. Also see Fig. 4.14.*

Parameters	**5/10 spiral**	**6/14 spiral**
^{1}H RF power (watt)	10	10
^{1}H 90° pulse length (µs)	11	11
Number of data points in FID	4096	4096
^{13}C RF power (watt)	25	30
^{13}C 90° pulse length (µs)	30	28
Number of data points in FID	512	512
Decoupling power (watt)	0.7	0.7
Decoupling length (µs)	20	20
Number of scans	8	8
J-coupling constant J (Hz)	145	145
$\tau = (4J)^{-1}$ (ms)	1.72	1.72
Increment delay D_0 (µs)	3	3

Chapter 5

Conclusion and outlook

5.1 Conclusion

The research presented in this thesis addresses the fundamental sensitivity and hardware complexity challenges of micro NMR by introducing two significant designs of broadband micro NMR detectors. This thesis involves three typical coil geometries, two distinct yet complementary microfabrication techniques. Taking advantages of the microfabrication techniques, both prototypes can be batch-fabricated with reliable reproducibility, and the fabrication processes and performance are systematically investigated. Both detector designs enable broadband operation from 100 MHz to 500 MHz, supporting 1D and 2D NMR experiments with sufficient sensitivity and spectral resolution. There is potential to measure more samples than the 5 nuclei presented in this thesis for different micro NMR applications.

In the third chapter, the stripline Lenz lens (S3L) demonstrates an effective method for focusing magnetic flux in micro NMR, using the combination of the Lenz lens and stripline coil as a non-resonant, passive element. This structure was able to rotate the RF field and confine excitation to a precise focal region. A major achievement of this work was the realization of a nearly uniform RF field with up to an 11-fold enhancement in SNR compared to standard setups. Because the S3L does not rely on its own geometry for resonance, it operates across a wide bandwidth, successfully detecting multiple isotopes. As an add-on chip, it effectively bridges the spatial gap between micro samples and standard resonators.

The fourth chapter reports on a robust, double-channel micro detector fabricated for the first time using low-temperature co-fired ceramic (LTCC) technology. By adding a third electrical contact at an intermediary position on a planar spiral, this design optimized detection sensitivity across two distinct frequency bands. This work highlighted the practical advantages of an untuned and unmatched broadband approach, which drastically simplifies probe hardware by removing complex tuning circuits while achieving sensitive multi-nuclear 1D and 2D NMR. The LTCC-based chips demonstrated high mechanical strength and chemical resistance, proving to be a durable platform for integrating microfluidics with multi-nuclear spectroscopy in cost-effective, high-resolution NMR applications.

The transition from a resonant paradigm to a non-resonant architecture is not merely a quantitative change in circuit parameters, but a fundamental shift in design philosophy. By prioritizing versatility over peak sensitivity, the broadband approaches in this thesis are intentionally adopted, in order to circumvent the physical bandwidth limitations, opening new pathways for investigating complex sample information in extreme and highly dynamic environments. While the suppression of resonance-induced signal gain leads to an intrinsic SNR reduction, this trade-off is strategically mitigated by optimizing the micro-scale geometry of the coils. Together, these works demonstrate that high-performance broadband NMR detector is achievable through coil geometry optimization at a micro-scale and proper fabrication techniques, significantly reducing the maintenance and cost barriers traditionally associated with high-field micro NMR spectroscopy.

5.2 Outlook

The research presented in this thesis establishes a foundation for a more flexible and universal micro-NMR detector. While the current work demonstrates the feasibility of broadband, untuned detection, several promising directions remain for transitioning these prototypes into widely deployable NMR hardware.

With an integrated micro sample channel, the stripline Lenz lens can be explored for needle-type samples, for example in biopsy tissue analysis. The design also provides a unique field-flipping capability that may be valuable in specialized industrial applications. By further refining the S3L's capability to reorient the RF field by 90°, it may become possible to circumvent the electrical shielding by metal electrodes in battery materials. This could enable in situ monitoring of electrochemical processes that are otherwise difficult to access with conventional NMR resonators. In addition, the non-resonant nature of the lens makes it suitable for studying thin films and membranes, where the detector could function as a "plug-and-play" interposer without extensive recalibration.

The successful implementation of split-spiral coils in LTCC technology also opens the door to more sophisticated three-dimensional geometries. In addition to the planar spirals presented here, multilayer micro-Helmholtz or solenoid coils could be fabricated and evaluated for NMR studies. Future developments may also explore the monolithic integration of complex microfluidic systems directly alongside the coils. At the same time, a thorough characterization of the magnetic susceptibility of LTCC substrates would be beneficial as more LTCC-based NMR coils are developed. Although LTCC offers high mechanical strength and low dielectric loss, small variations in layer thickness or planarity after firing can influence B_0 and B_1 field homogeneity. A systematic understanding of the material properties of different LTCC compositions will therefore be important for further improving the spectral resolution of broadband micro detectors.

The main trade-off for untuned, non-matched detectors is a moderate reduction in sensitivity. One approach to mitigating this limitation is the integration of advanced CMOS transceiver circuits directly at the detector head, which can reduce noise and improve power transfer. By

moving the complexity from analog hardware to digital signal processing, the next generation of detectors will likely feature MEMS-integrated broadband coils coupled with ultra-wide band low-noise amplifiers. In addition, artificial intelligence (AI) offers significant potential for broadband NMR applications [198]. Machine learning methods have been explored for broadband pulse design [199, 200], automated shimming [201], and spectrum or MRI reconstruction [202, 203]. Such approaches may help compensate for challenges such as field inhomogeneity in planar geometries, and signal crosstalk in broadband detection. By combining cost-efficient micro detectors with AI-assisted operation, broadband micro-NMR systems could become robust and widely accessible tools for researchers across a wide range of scientific and industrial disciplines. We envision a transition toward total-capture NMR with the entire available magnetic resonance spectrum in a single acquisition. This will not only lower the barrier to entry for multi-nuclear studies but also enable real-time, multi-modal characterization in the most demanding scientific environments.

Bibliography

[1] I. I. Rabi, J. R. Zacharias, S. Millman, and P. Kusch. A New Method of Measuring Nuclear Magnetic Moment. *Physical Review*, 53(4):318–318, February 1938.

[2] F. Bloch. Nuclear Induction. *Physical Review*, 70(7-8):460–474, October 1946.

[3] E. M. Purcell, H. C. Torrey, and R. V. Pound. Resonance Absorption by Nuclear Magnetic Moments in a Solid. *Physical Review*, 69(1-2):37–38, January 1946.

[4] Malcolm H Levitt. *Spin dynamics: basics of nuclear magnetic resonance*. John Wiley & Sons, 2008.

[5] Ekaterina Nikolskaya and Yrjo Hiltunen. Time-domain NMR in characterization of liquid fuels: A mini-review. *Energy & Fuels*, 34(7):7929–7934, 2020.

[6] Christoph Juchem and Robin A. De Graaf. B0 Magnetic Field Homogeneity and Shimming for in Vivo Magnetic Resonance Spectroscopy. *Analytical Biochemistry*, 529:17–29, July 2017.

[7] Gerald A Pearson. Shimming an NMR Magnet. pages 1–16, 1991.

[8] Andrew Phair, Michael Brideson, and Lawrence K. Forbes. A Cylindrical Basis Set for Shim Coil Design in Magnetic Resonance Imaging. *Concepts in Magnetic Resonance Part B: Magnetic Resonance Engineering*, 48B(3):e21400, July 2018.

[9] SF Ahmad, YC Kim, IC Choi, and HD Kim. Recent progress in birdcage RF coil technology for MRI system. Diagnostics 10 (12): 1017, 2020.

[10] Michael Schatz, Matthias Streun, Sven Jovanovic, Rüdiger-A Eichel, and Granwehr Josef. Workflow for systematic design of electrochemical in operando NMR cells by matching B 0 and B 1 field simulations with experiments. *Magnetic Resonance Discussions*, 2024:1–22, 2024.

[11] Minkyu Park, Hansol Noh, and Namkyoo Park. Mitigation of B1+ inhomogeneity for ultra-high-field magnetic resonance imaging: Hybrid mode shaping with auxiliary EM potential. *Scientific Reports*, 10(1):11752, 2020.

[12] Tales Santini, Sossena Wood, Narayanan Krishnamurthy, Tiago Martins, Howard J Aizenstein, and Tamer S Ibrahim. Improved 7 Tesla transmit field homogeneity with reduced electromagnetic power deposition using coupled Tic Tac Toe antennas. *Scientific reports*, 11(1):3370, 2021.

[13] Tamer S Ibrahim and Lin Tang. Insight into RF power requirements and B1 field homogeneity for human MRI via rigorous FDTD approach. *Journal of Magnetic Resonance Imaging: An Official Journal of the International Society for Magnetic Resonance in Medicine*, 25(6):1235–1247, 2007.

[14] Piotr Lepucki, Adam P Dioguardi, Daniil Karnaushenko, Oliver G Schmidt, and Hans-Joachim Grafe. The normalized limit of detection in NMR spectroscopy. *Journal of Magnetic Resonance*, 332:107077, 2021.

[15] Mark S Conradi. NMR instrumentation-a primer. *Journal of Magnetic Resonance Open*, 12:100081, 2022.

[16] Craig D. Eccles, Stuart Crozier, Wolfgang Roffman, David M. Doddrell, Philip Back, and Paul T. Callaghan. Practical Aspects of Shielded Gradient-Coil Design for Localised in Vivo NMR Spectroscopy and Small-Scale Imaging. *Magnetic Resonance Imaging*, 12(4):621–630, January 1994.

[17] Jose L Uribe and Rachel W Martin. A practical introduction to radio frequency electronics for NMR probe builders. *Journal of Magnetic Resonance Open*, page 100153, 2024.

[18] Seungmun Jeon, Gunhee Jang, Hyunchul Choi, and Sukho Park. Magnetic navigation system with gradient and uniform saddle coils for the wireless manipulation of micro-robots in human blood vessels. *IEEE transactions on magnetics*, 46(6):1943–1946, 2010.

[19] Henk Wensink, Fernando ... Benito-Lopez, and Albert van den Berg. Measuring reaction kinetics in a lab-on-a-chip by microcoil NMR. *Lab on a Chip*, 5(3):280–284, 2005.

[20] C Massin, F ... Vincent, and RS Popovic. Planar microcoil-based microfluidic NMR probes. *Journal of Magnetic Resonance*, 164(2):242–255, 2003.

[21] Jonathan D Trumbull, Ian K Glasgow, David J Beebe, and Richard L Magin. Integrating microfabricated fluidic systems and NMR spectroscopy. *IEEE Transactions on Biomedical Engineering*, 47(1):3–7, 2000.

[22] Oliver G Gruschke, Nicoleta ... Baxan, and Jan G Korvink. Lab on a chip phased-array MR multi-platform analysis system. *Lab on a Chip*, 12(3):495–502, 2012.

[23] Nils Spengler, Peter T. While, Markus V. Meissner, Ulrike Wallrabe, and Jan G. Korvink. Magnetic Lenz lenses improve the limit-of-detection in nuclear magnetic resonance. *PLoS ONE*, 12(8):1–17, 2017.

[24] Monica Bastawrous, Rajshree Ghosh Biswas, Ronald Soong, Mazin Jouda, Neil MacKinnon, Dario Mager, Jan G Korvink, and Andre J Simpson. Lenz Lenses in a Cryoprobe: Boosting NMR Sensitivity Toward Environmental Monitoring of Mass-Limited Samples. *Analytical Chemistry*, 95(2):1327–1334, 2022.

[25] Mazin Jouda, Robert Kamberger, Jochen Leupold, Nils Spengler, Jürgen Hennig, Oliver Gruschke, and Jan G Korvink. A comparison of Lenz lenses and LC resonators for NMR signal enhancement. *Concepts in Magnetic Resonance Part B: Magnetic Resonance Engineering*, 47(3):e21357, 2017.

[26] G. Pares, J.-P. Michel, E. Deschaseaux, V. Pernin, A. Giry, P. Ferris, and A. Serhan. Inductors Using 2.5d Silicon Interposer with Thick Rdl and Tsv-Last Technologies. *International Symposium on Microelectronics*, 2017(1):000072–000077, October 2017.

[27] Wen Huang, Zhendong Yang, Mark D. Kraman, Qingyi Wang, Zihao Ou, Miguel Muñoz Rojo, Ananth Saran Yalamarthy, Victoria Chen, Feifei Lian, Jimmy H. Ni, Siyu Liu, Haotian Yu, Lei Sang, Julian Michaels, Dane J. Sievers, J. Gary Eden, Paul V. Braun, Qian Chen, Songbin Gong, Debbie G. Senesky, Eric Pop, and Xiuling Li. Monolithic Mtesla-Level Magnetic Induction by Self-Rolled-up Membrane Technology. *Science Advances*, 6(3):eaay4508, January 2020.

[28] Hoa Thanh Le, Rubaiyet I. Haque, Ziwei Ouyang, Seung Woo Lee, Shelley I. Fried, Ding Zhao, Min Qiu, and Anpan Han. MEMS Inductor Fabrication and Emerging Applications in Power Electronics and Neurotechnologies. *Microsystems & Nanoengineering*, 7(1):59, August 2021.

[29] Eli Bendet-Taicher, Norbert Müller, and Alexej Jerschow. Dependence of NMR noise line shapes on tuning, matching, and transmission line properties. *Concepts in Magnetic Resonance Part B: Magnetic Resonance Engineering*, 44(1):1–11, 2014.

[30] F. Hwang and D. I. Hoult. Automatic Probe Tuning and Matching. *Magnetic Resonance in Medicine*, 39(2):214–222, February 1998.

[31] Bálint Koczor, Inez Sedyó, and János Rohonczy. An Alternative Solution for Computer Controlled Tuning and Matching of Existing NMR Probes. *Journal of Magnetic Resonance*, 259:179–185, October 2015.

[32] Oliver Pecher, Paul M. Bayley, Hao Liu, Zigeng Liu, Nicole M. Trease, and Clare P. Grey. Automatic Tuning Matching Cycler (ATMC) in Situ NMR Spectroscopy as a Novel Approach for Real-Time Investigations of Li- and Na-Ion Batteries. *Journal of Magnetic Resonance*, 265:200–209, April 2016.

[33] P Andris. Matching and Tuning RF Coils for NMR Tomograph. *Measurement Science Review*, 1(1):115–118, 2001.

[34] Kelsey A. Collier, Suvrajit Sengupta, Catalina A. Espinosa, John E. Kelly, Jessica I. Kelz, and Rachel W. Martin. Design and Construction of a Quadruple-Resonance MAS NMR Probe for Investigation of Extensively Deuterated Biomolecules. *Journal of Magnetic Resonance*, 285:8–17, 2017.

[35] David M Pozar. *Microwave engineering: theory and techniques*. John wiley & sons, 2021.

[36] David I Hoult and Balram Bhakar. NMR signal reception: Virtual photons and coherent spontaneous emission. *Concepts in Magnetic Resonance: An Educational Journal*, 9(5):277–297, 1997.

[37] Antoine Dupré, Ka-Meng Lei, Pui-In Mak, Rui P. Martins, and Weng Kung Peng. Micro- and Nanofabrication NMR Technologies for Point-of-Care Medical Applications – a Review. *Microelectronic Engineering*, 209:66–74, March 2019.

[38] Jens Anders, Frederik Dreyer, Daniel Krüger, Ilai Schwartz, Martin B. Plenio, and Fedor Jelezko. Progress in Miniaturization and Low-Field Nuclear Magnetic Resonance. *Journal of Magnetic Resonance*, 322:106860, January 2021.

[39] G. Boero, C. De Raad Iseli, P.A. Besse, and R.S. Popovic. An NMR Magnetometer with Planar Microcoils and Integrated Electronics for Signal Detection and Amplification. *Sensors and Actuators A: Physical*, 67(1-3):18–23, May 1998.

[40] B Sorli, J F Chateaux, M Pitaval, H Chahboune, B Favre, A Briguet, and P Morin. Micro-Spectrometer for NMR: Analysis of Small Quantities *in Vitro*. *Measurement Science and Technology*, 15(5):877–880, May 2004.

[41] A.G. Webb. Microcoil Nuclear Magnetic Resonance Spectroscopy. *Journal of Pharmaceutical and Biomedical Analysis*, 38(5):892–903, August 2005.

[42] Bernhard Blümich, Christian Rehorn, and Wasif Zia. Magnets for small-scale and portable NMR. *Micro and Nano Scale NMR: Technologies and Systems*, pages 1–20, 2018.

[43] Dongwan Ha, Jeffrey Paulsen, Nan Sun, Yi-Qiao Song, and Donhee Ham. Scalable NMR Spectroscopy with Semiconductor Chips. *Proceedings of the National Academy of Sciences*, 111(33):11955–11960, August 2014.

[44] Shuhao Fan, Qi Zhou, Ka-Meng Lei, Pui-In Mak, and Rui P. Martins. Miniaturization of a Nuclear Magnetic Resonance System: Architecture and Design Considerations of Transceiver Integrated Circuits. *IEEE Transactions on Circuits and Systems I: Regular Papers*, 69(8):3049–3060, August 2022.

[45] Sergey S. Zalesskiy, Ernesto Danieli, Bernhard Blümich, and Valentine P. Ananikov. Miniaturization of NMR Systems: Desktop Spectrometers, Microcoil Spectroscopy, and "NMR on a Chip" for Chemistry, Biochemistry, and Industry. *Chemical Reviews*, 114(11):5641–5694, June 2014.

[46] Hakho Lee, Eric Sun, Donhee Ham, and Ralph Weissleder. Chip–NMR biosensor for detection and molecular analysis of cells. *Nature medicine*, 14(8):869–874, 2008.

[47] Yong Liu, Nan Sun, Hakho ... Lee, and Donhee Ham. CMOS Mini Nuclear Magnetic Resonance System and Its Application for Biomolecular Sensing. In *2008 IEEE International Solid-State Circuits Conference - Digest of Technical Papers*, pages 140–602, San Francisco, CA, USA, February 2008. IEEE.

[48] Nan Sun, Tae-Jong Yoon, Hakho Lee, William Andress, Ralph Weissleder, and Donhee Ham. Palm NMR and 1-Chip NMR. *IEEE Journal of Solid-State Circuits*, 46(1):342–352, January 2011.

[49] Vasiliki Demas, Julie L. Herberg, Vince Malba, Anthony ... Bernhardt, and Jeffrey Reimer. Portable, Low-Cost NMR with Laser-Lathe Lithography Produced Microcoils. *Journal of Magnetic Resonance*, 189(1):121–129, November 2007.

[50] Soumyajit Mandal, Shin Utsuzawa, and Yi-Qiao Song. An extremely broadband low-frequency MR system. *Microporous and Mesoporous Materials*, 178:53–55, 2013.

[51] Kazuyuki Takeda. A highly integrated FPGA-based nuclear magnetic resonance spectrometer. *Review of scientific instruments*, 78(3), 2007.

[52] Marco Grisi, Gabriele Gualco, and Giovanni Boero. A broadband single-chip transceiver for multi-nuclear NMR probes. *Review of Scientific Instruments*, 86(4), 2015.

[53] Megan A Macnaughtan, Ting Hou, Jun Xu, and Daniel Raftery. High-throughput nuclear magnetic resonance analysis using a multiple coil flow probe. *Analytical chemistry*, 75(19):5116–5123, 2003.

[54] Ka-Meng Lei, Pui-In Mak, Man-Kay Law, and Rui P Martins. A μ NMR CMOS Transceiver Using a Butterfly-Coil Input for Integration With a Digital Microfluidic Device Inside a Portable Magnet. *IEEE Journal of Solid-State Circuits*, 51(10):2274–2286, 2016.

[55] Burkhard Luy. Towards Portable High-Resolution NMR Spectroscopy. *Angewandte Chemie International Edition*, 50(2):354–356, 2011.

[56] Klaus Halbach. Design of permanent multipole magnets with oriented rare earth cobalt material. *Nuclear instruments and methods*, 169(1):1–10, 1980.

[57] Norihide Saho, Kazuya Matsuda, and Noriyo Nishijima. Palm-size miniature superconducting bulk magnet. *Cryogenics*, 52(11):604–608, 2012.

[58] Jaehyup Kim, Bruce Hammer, and Ramesh Harjani. A 5–300MHz CMOS transceiver for multi-nuclear NMR spectroscopy. In *Proceedings of the IEEE 2012 Custom Integrated Circuits Conference*, pages 1–4. IEEE, 2012.

[59] Kazuyuki Takeda. OPENCORE NMR: Open-source core modules for implementing an integrated FPGA-based NMR spectrometer. *Journal of Magnetic Resonance*, 192(2):218–229, 2008.

[60] Yiqiao Tang, David McCowan, and Yi-Qiao Song. A Miniaturized Spectrometer for NMR Relaxometry under Extreme Conditions. *Scientific Reports*, 9(1):11174, August 2019.

[61] Marco Grisi, Franck Vincent, Beatrice Volpe, Roberto Guidetti, Nicola Harris, Armin Beck, and Giovanni Boero. NMR spectroscopy of single sub-nL ova with inductive ultra-compact single-chip probes. *Scientific reports*, 7(1):44670, 2017.

[62] Masaya Kakuta, Dimuthu A Jayawickrama, Andrew M Wolters, Andreas Manz, and Jonathan V Sweedler. Micromixer-based time-resolved NMR: applications to ubiquitin protein conformation. *Analytical chemistry*, 75(4):956–960, 2003.

[63] Jacob Bart, Ard J ... Kolkman, et al. A microfluidic high-resolution NMR flow probe. *Journal of the American Chemical Society*, 131(14):5014–5015, 2009.

[64] Anna Jo Oosthoek-de Vries, Jacob Bart, Roald M ... Tiggelaar, and Arno P M Kentgens. Continuous flow 1H and 13C NMR spectroscopy in microfluidic stripline NMR chips. *Analytical chemistry*, 89(4):2296–2303, 2017.

[65] Frank C Schroeder and Matthew Gronquist. Extending the scope of NMR spectroscopy with microcoil probes. *Angewandte Chemie International Edition*, 45(43):7122–7131, 2006.

[66] Dean L Olson, Timothy L ... Peck, and Jonathan V Sweedler. High-resolution microcoil 1H-NMR for mass-limited, nanoliter-volume samples. *Science*, 270(5244):1967–1970, 1995.

[67] Robert Ch Meier, Jens Höfflin, Vlad Badilita, Ulrike Wallrabe, and Jan G. Korvink. Microfluidic Integration of Wirebonded Microcoils for On-Chip Applications in Nuclear Magnetic Resonance. *Journal of Micromechanics and Microengineering*, 24(4), 2014.

[68] P. Krivic, M. Weilguni, and G. Radosavljevic. Realization of Three-Dimensional Solenoidal Microcoils with Air Core in Low Temperature Co-Fired Ceramics Technology. *Proceedings of the International Spring Seminar on Electronics Technology*, pages 59–63, 2013.

[69] Ka-Meng Lei, Dongwan Ha, Yi-Qiao ... Song, and Donhee Ham. Portable NMR with Parallelism. *Analytical Chemistry*, 92(2):2112–2120, January 2020.

[70] Klaus Ehrmann, Nicolas Saillen, Franck Vincent, Matthieu Stettler, Martin Jordan, Florian Maria Wurm, Pierre-André Besse, and Radivoje Popovic. Microfabricated solenoids and Helmholtz coils for NMR spectroscopy of mammalian cells. *Lab on a Chip*, 7(3):373–380, 2007.

[71] T.L. Peck, R.L. Magin, J. Kruse, and M. Feng. NMR Microspectroscopy Using 100 Mm Planar RF Coils Fabricated on Gallium Arsenide Substrates. *IEEE Transactions on Biomedical Engineering*, 41(7):706–709, July 1994.

[72] Meriam Khelifa, Denis Mounier, and Nourdin Yaakoubi. Design of High Performance Scroll Microcoils for Nuclear Magnetic Resonance Spectroscopy of Nanoliter and Subnanoliter Samples. *Sensors*, 21(1):170, December 2020.

[73] Graeme Finch, Ali Yilmaz, and Marcel Utz. An optimised detector for in-situ high-resolution NMR in microfluidic devices. *Journal of Magnetic Resonance*, 262:73–80, 2016.

[74] Koen CH Tijssen, Jacob Bart, Roald M ... Tiggelaar, and P Jan M van Bentum. Spatially resolved spectroscopy using tapered stripline NMR. *Journal of Magnetic Resonance*, 263:136–146, 2016.

[75] Erik Odeblad. Micro-NMR in high permanent magnetic fields. Theoretical and experimental investigations with an application to the secretions from single glandular units in the human uterine cervix. *Acta obstetricia et gynecologica Scandinavica*, 45:1–188, 1966.

[76] Nian Wu, Timothy L Peck, Andrew G Webb, Richard L Magin, and Jonathan V Sweedler. 1H-NMR spectroscopy on the nanoliter scale for static and online measurements. *Analytical Chemistry*, 66(22):3849–3857, 1994.

[77] Akshata Barne, Swarangee Malhari, Tanvi Lakhani, and Ninad Mehendale. A Review on Types of NMR Micro-Coil Designs. *Available at SSRN 4116746*, 2022.

[78] Jianyong Lou, Haixia Ren, Xia Chao, Kesong Chen, Haodong Bai, and Zhengyue Wang. Recent Progress in the Preparation Technologies for Micro Metal Coils. *Micromachines*, 13(6):872, May 2022.

[79] R. Subramanian, M.M. Lam, and A.G. Webb. RF Microcoil Design for Practical NMR of Mass-Limited Samples. *Journal of Magnetic Resonance*, 133(1):227–231, July 1998.

[80] Nils Spengler, Jens Hoefflin, Ali Moazenzadeh, Dario Mager, Neil MacKinnon, Vlad Badilita, Ulrike Wallrabe, and Jan G Korvink. Heteronuclear micro-Helmholtz coil facilitates μm-range spatial and sub-Hz spectral resolution NMR of nL-volume samples on customisable microfluidic chips. *PloS One*, 11(1):e0146384, 2016.

[81] Xiaonan Li, Guoqiang Liu, Shiqiang Li, Hui Xia, and Yong Wang. Planar-coil-based micro-detection in nuclear magnetic resonance spectroscopy. In *2018 5th International Conference on Systems and Informatics (ICSAI)*, pages 895–899. IEEE, 2018.

[82] Yu Liyuan, Li Shushu, Niu Pingjuan, Shi Hao, Mao Run, and Cheng Zheng. Novel square spiral Coil for achieving uniform Distribution of magnetic Field. In *IOP Conference Series: Earth and Environmental Science*, volume 332, page 042005. IOP Publishing, 2019.

[83] Rithvik Reddy Adapap, Syed Sarfaraz Nawaz, and Dola Gobinda Padhan. Analytical study of magnetic flux density for circular spiral and square spiral coils. In *2021 International Conference on Sustainable Energy and Future Electric Transportation (SEFET)*, pages 1–6. IEEE, 2021.

[84] Hossein Davoodi, Nurdiana ... Nordin, and Vlad Badilita. Untuned broadband spiral microcoils achieve sensitive multi-nuclear NMR TX/RX from microfluidic samples. *Scientific reports*, 11(1):1–12, 2021.

[85] Raluca M Fratila, M Victoria Gomez, Stanislav Sỳkora, and Aldrik H Velders. Multinuclear nanoliter one-dimensional and two-dimensional NMR spectroscopy with a single non-resonant microcoil. *Nature Communications*, 5(1):3025, 2014.

[86] Nichlas Vous Christensen, Sissel Ellemose Liboriussen, Juan D Sanchez-Heredia, Esben Søvsø Szocska Hansen, Christoffer Laustsen, and Lotte Bonde Bertelsen. 30-Channel Microcoil System for High-Throughput Metabolic Flux Analysis Using Hyperpolarized 13C NMR Spectroscopy. *NMR in Biomedicine*, 38(12):e70174, 2025.

[87] P. J. M. Van Bentum, J. W. G. Janssen, A. P. M. Kentgens, J. Bart, and J. G E Gardeniers. Stripline probes for nuclear magnetic resonance. *Journal of Magnetic Resonance*, 189(1):104–113, 2007.

[88] Bart, J. and Janssen, J. W. G. and van Bentum, P. J. M. and Kentgens, A. P. M. and Gardeniers, Johannes GE. Optimization of stripline-based microfluidic chips for high-resolution NMR. *Journal of magnetic resonance*, 201(2):175–185, 2009.

[89] J Bart, A J Oosthoek-de Vries, K ... Tijssen, and A P M Kentgens. In-line NMR analysis using stripline based detectors. In *Proc. 14th Int. Conf. on Miniaturized Systems for Chemistry and Life Sciences*, pages 2086–8, 2010.

[90] S G J Van Meerten, Fleur van Zelst, Koen Tijssen, and Arno P M Kentgens. An Optimized NMR Stripline for Sensitive Supercritical Fluid Chromatography-Nuclear Magnetic Resonance of Microliter Sample Volumes. *Analytical chemistry*, 92(19):13010–13016, 2020.

[91] Koen C. H. Tijssen, Bram J. A. van Weerdenburg, Hainan Zhang, J. W. G. Janssen, Martin C. Feiters, P. Jan M. van Bentum, and Arno P. M. Kentgens. Monitoring Heterogeneously Catalyzed Hydrogenation Reactions at Elevated Pressures Using In-Line Flow NMR. *Analytical chemistry*, 91(20):12636–12643, 2019.

[92] Eric G. Sorte, Nathan A. Banek, Michael J. Wagner, Todd M. Alam, and Yu Ye J. Tong. In Situ Stripline Electrochemical NMR for Batteries. *ChemElectroChem*, 5(17):2336–2340, 2018.

[93] K. Yamauchi, J. W.G. Janssen, and A. P.M. Kentgens. Implementing Solenoid Microcoils for Wide-Line Solid-State NMR. *Journal of Magnetic Resonance*, 167(1):87–96, 2004.

[94] Chukun Gao, Pin-Hui Chen, Alexander Däpp, Michael A Urban, Ronny Gunzenhauser, Nicholas Alaniva, and Alexander B Barnes. Improving the sensitivity of MAS spheres using a 9.5 mm spherical shell with 219 μL sample volume spinning in a spherical solenoid coil. *Journal of Magnetic Resonance*, 343:107305, 2022.

[95] Dimitrios Sakellariou, G Le Goff, and J-F Jacquinot. High-resolution, high-sensitivity NMR of nanolitre anisotropic samples by coil spinning. *Nature*, 447(7145):694–697, 2007.

[96] Vlad Badilita, Birgit Fassbender, Kai Kratt, Alan Wong, Christian Bonhomme, Dimitris Sakellariou, Jan G. Korvink, and Ulrike Wallrabe. Microfabricated Inserts for Magic Angle Coil Spinning (MACS) Wireless NMR Spectroscopy. *PLOS ONE*, 7(8):1–8, 08 2012.

[97] Jacek W Hennel and Jacek Klinowski. Magic-angle spinning: a historical perspective. *New techniques in solid-state NMR*, pages 1–14, 2004.

[98] Hans Janssen, Andreas Brinkmann, Ernst RH Van Eck, P Jan M van Bentum, and Arno PM Kentgens. Microcoil high-resolution magic angle spinning NMR spectroscopy. *Journal of the American Chemical Society*, 128(27):8722–8723, 2006.

[99] APM Kentgens, J Bart, PJM Van Bentum, A Brinkmann, ERH Van Eck, Johannes GE Gardeniers, JWG Janssen, P Knijn, S Vasa, and MHW Verkuijlen. High-resolution liquid- and solid-state nuclear magnetic resonance of nanoliter sample volumes using microcoil detectors. *The Journal of chemical physics*, 128(5):052202, 2008.

[100] Edward W Hagaman, Jian Jiao, and Tony Moore. The generation of intense radiofrequency fields in μcoils. *Journal of Magnetic Resonance*, 193(1):150–152, 2008.

[101] Pinhui Chen, Brice J Albert, Chukun Gao, Nicholas Alaniva, Lauren E Price, Faith J Scott, Edward P Saliba, Erika L Sesti, Patrick T Judge, Edward W Fisher, et al. Magic angle spinning spheres. *Science advances*, 4(9):eaau1540, 2018.

[102] V Badilita, B Fassbender, O Gruschke, K Kratt, R Meier, D Sakellariou, JG Korvink, and U Wallrabe. Inductively coupled wirebonded microcoils for wireless on-chip NMR. In *2011 16th International Solid-State Sensors, Actuators and Microsystems Conference*, pages 2798–2800. IEEE, 2011.

[103] Shyam S Adhikari, Li Zhao, Thomas Dickmeis, Jan G Korvink, and Vlad Badilita. Inductively coupled magic angle spinning microresonators benchmarked for high-resolution single embryo metabolomic profiling. *Analyst*, 144(24):7192–7199, 2019.

[104] Yusuke Nishiyama, Yuki Endo, Takahiro Nemoto, Anne-Karine Bouzier-Sore, and Alan Wong. High-resolution NMR-based metabolic detection of microgram biopsies using a 1 mm HRμMAS probe. *Analyst*, 140(24):8097–8100, 2015.

[105] Nghia Tuan Duong, Masanori Yamato, Masayuki Nakano, Satoshi Kume, Yasuhisa Tamura, Yosky Kataoka, Alan Wong, and Yusuke Nishiyama. Capillary-inserted rotor design for HRμMAS NMR-based metabolomics on mass-limited neurospheres. *Molecules*, 22(8):1289, 2017.

[106] Sagar Wadhwa, Mazin Jouda, Yongbo Deng, Omar Nassar, Dario Mager, and Jan G Korvink. Topologically optimized magnetic lens for magnetic resonance applications. *Magnetic Resonance*, 1(2):225–236, 2020.

[107] Suleman Shakil, Mikhail Kudryavtsev, Tamara Bechtold, Andreas Greiner, and Jan G Korvink. Compact Modeling Techniques for Magnetic Resonance Detectors. *Micro and Nano Scale NMR: Technologies and Systems*, pages 21–56, 2018.

[108] Techit Tritrakarn, Masato Takahashi, and Tetsuji Okamura. Optimization of RF coil geometry for NMR/MRI applications using a genetic algorithm. *Journal of Magnetic Resonance*, 362:107685, 2024.

[109] Natachai Terawatsakul, Alireza Saberkari, Yuttapoom Puttisong, and Morgan Madec. Scaling Nuclear Magnetic Resonance with Integrated Planar Coil and Transceiver Front-End: Co-Design Considerations. *Electronics*, 14(2):398, 2025.

[110] Jan Korvink, Vlad Badilita, Dario Mager, Oliver Gruschke, Nils Spengler, Shyam Sundar Adhikari Parenky, Ulrike Wallrabe, and Markus Meissner. Innovative Coil Fabrication Techniques for Miniaturized Magnetic Resonance Detectors. *Micro and Nano Scale NMR: Technologies and Systems*, pages 109–141, 2018.

[111] Oliver Gruschke, Mazin Jouda, and Jan G Korvink. Microarrays and Microelectronics for Magnetic Resonance. *Micro and Nano Scale NMR: Technologies and Systems*, pages 59–73, 2018.

[112] Jessica I. Kelz, John E. Kelly, and Rachel W. Martin. 3D-printed Dissolvable Inserts for Efficient and Customizable Fabrication of NMR Transceiver Coils. *Journal of Magnetic Resonance*, 305:89–92, August 2019.

[113] Vincent Malba, Robert Maxwell, Leland B. Evans, Anthony F. Bernhardt, Monique Cosman, and Kin Yan. Laser-Lathe Lithography—a Novel Method for Manufacturing Nuclear Magnetic Resonance Microcoils. *Biomedical Microdevices*, 5(1):21–27, 2003.

[114] Jooncheol Kim, Minsoo Kim, Jung-Kwun Kim, Florian Herrault, and Mark G Allen. Anisotropic Nanolaminated CoNiFe Cores Integrated into Microinductors for High-Frequency Dc–Dc Power Conversion. *Journal of Physics D: Applied Physics*, 48(46):462001, November 2015.

[115] Cheol Woo Ha, Prem Prabhakaran, and Yong Son. 3D-printed Polymer/Metal Hybrid Microstructures with Ultraprecision for 3D Microcoils. *3D Printing and Additive Manufacturing*, 6(3):165–170, June 2019.

[116] Junyao Xie, Xueqiu You, Yuqing ... Huang, and Zhong Chen. 3D-printed Integrative Probeheads for Magnetic Resonance. *Nature Communications*, 11(1), December 2020.

[117] Hoa Thanh Le, Io Mizushima, Yasser Nour, Peter Torben Tang, Arnold Knott, Ziwei Ouyang, Flemming Jensen, and Anpan Han. Fabrication of 3D Air-Core MEMS Inductors for Very-High-Frequency Power Conversions. *Microsystems & Nanoengineering*, 4(1):17082, January 2018.

[118] Hakan Alaboz, Andras Kovacs, Daniel Johannes Förster, Lucas Werling, Jajnabalkya Guhathakurta, Julien Petit, Morgan Madec, Luc Hébrard, and Ulrich Mescheder. Fabrication and characterization of 3D micro-coils with hybrid manufacturing methods. *Journal of Manufacturing Processes*, 145:190–200, 2025.

[119] Hanne Vanduffel, Cesar Parra-Cabrera, Willy Gsell, Rodrigo Oliveira-Silva, Louca Goossens, Ronald Peeters, Uwe Himmelreich, Brecht Van Hooreweder, Dimitrios Sakellariou, Wim Vanduffel, and Rob Ameloot. Additive Manufacturing of Subject-Conformal Receive Coils for Magnetic Resonance Imaging. *Advanced Materials Technologies*, 7(12):2200647, December 2022.

[120] Luca Hirt, Alain Reiser, Ralph Spolenak, and Tomaso Zambelli. Additive Manufacturing of Metal Structures at the Micrometer Scale. *Advanced Materials*, 29(17):1604211, May 2017.

[121] Xi-Ning Wang, Xiao-Lin Zhao, Yong Zhou, Xu-Han Dai, and Bing-Chu Cai. Fabrication and Performance of a Novel Suspended RF Spiral Inductor. *IEEE Transactions on Electron Devices*, 51(5):814–816, May 2004.

[122] Ka-Meng Lei, Pui-In Mak, Man-Kay Law, and Rui P. Martins. A Palm-Size μNMR Relaxometer Using a Digital Microfluidic Device and a Semiconductor Transceiver for Chemical/Biological Diagnosis. *The Analyst*, 140(15):5129–5137, 2015.

[123] Jonas Handwerker, Marlon Pérez-Rodas, Michael Beyerlein, Franck Vincent, Armin Beck, Nicolas Freytag, Xin Yu, Rolf Pohmann, Jens Anders, and Klaus Scheffler. A CMOS NMR Needle for Probing Brain Physiology with High Spatial and Temporal Resolution. *Nature Methods*, 17(1):64–67, January 2020.

[124] Xin Yu, Wen Huang, Moyang Li, Thomas M. Comberiate, Songbin Gong, Jose E. Schutt-Aine, and Xiuling Li. Ultra-Small, High-Frequency and Substrate-Immune Microtube Inductors Transformed from 2D to 3D. *Scientific Reports*, 5(1):9661, April 2015.

[125] Vittorio Saggiomo and Aldrik H Velders. Simple 3D printed scaffold-removal method for the fabrication of intricate microfluidic devices. *Advanced Science*, 2(9):1500125, 2015.

[126] E Montinaro, M Grisi, MC Letizia, L Pethö, MAM Gijs, R Guidetti, J Michler, Jürgen Brugger, and Giovanni Boero. 3D printed microchannels for sub-nL NMR spectroscopy. *PloS One*, 13(5):e0192780, 2018.

[127] Zheng Long, Jamie Ruthford, and Stanley J. Opella. 3D Printed Sample Tubes for Solid-State NMR Experiments. *Journal of Magnetic Resonance*, 327:106957, June 2021.

[128] Hossein Davoodi, Mazin Jouda, Jan G Korvink, Neil MacKinnon, and Vlad Badilita. Broadband and multi-resonant sensors for NMR. *Progress in Nuclear Magnetic Resonance Spectroscopy*, 112:34–54, 2019.

[129] Mitchell Schnall. Probes tuned to multiple frequencies for in-vivo NMR. In *In-Vivo Magnetic Resonance Spectroscopy I: Probeheads and Radiofrequency Pulses Spectrum Analysis*, pages 33–63. Springer, 1992.

[130] Pei Tang, Wei-Jyun Chien, and Gerard S Harbison. Double-resonance circuit for nuclear magnetic resonance spectroscopy. *Solid State Nuclear Magnetic Resonance*, 2(6):343–348, 1993.

[131] M.D Schnall, C Barlow, V.Harihara Subramanian, and J.S Leigh. Wireless Implanted Magnetic Resonance Probes for in Vivo NMR. *Journal of Magnetic Resonance (1969)*, 68(1):161–167, 1986.

[132] Munehiro Inukai and Kazuyuki Takeda. Double-Resonance Magic Angle Coil Spinning. *Journal of Magnetic Resonance*, 202(2):274–278, 2010.

[133] S Kan, M Fan, and J Courtieu. A single-coil triple resonance probe for NMR experiments. *Review of Scientific Instruments*, 51(7):887–890, 1980.

[134] Sasidhar Tadanki, Raul D. Colon, Jay Moore, and Kevin W. Waddell. Double Tuning a Single Input Probe for Heteronuclear NMR Spectroscopy at Low Field. *Journal of Magnetic Resonance*, 223:64–67, 2012.

[135] JH Walton, JS De Ropp, MV Shutov, AG Goloshevsky, MJ McCarthy, RL Smith, and SD Collins. A micromachined double-tuned NMR microprobe. *Analytical Chemistry*, 75(19):5030–5036, 2003.

[136] Jens Anders and Aldrik H Velders. Microcoils for broadband multinuclei detection. *Micro and Nano Scale NMR: Technologies and Systems*, 30, 2018.

[137] M Victoria Gomez, Sander Baas, and Aldrik H Velders. Multinuclear 1D and 2D NMR with 19F-Photo-CIDNP hyperpolarization in a microfluidic chip with untuned microcoil. *Nature Communications*, 14(1):3885, 2023.

[138] Eric Scott, Joel Stettler, and Jeffrey A Reimer. Utility of a tuneless plug and play transmission line probe. *Journal of Magnetic Resonance*, 221:117–119, 2012.

[139] D Murphree, SB Cahn, D Rahmlow, and D DeMille. An easily constructed, tuning free, ultra-broadband probe for NMR. *Journal of Magnetic Resonance*, 188(1):160–167, 2007.

[140] Atsushi Kubo and Shinji Ichikawa. Ultra-broadband NMR probe: numerical and experimental study of transmission line NMR probe. *Journal of Magnetic Resonance*, 162(2):284–299, 2003.

[141] Nathan Evetts. Unmatched delay line NMR probes for magnetic resonance. *Journal of Magnetic Resonance*, 385:108032, 2026.

[142] Harold T Stokesb), Thomas A Case, David C Ailion, and CH Wang. NMR observations of molecular motions and Zeeman–quadrupole cross relaxation in 1, 2-difluorotetrachloroethanea. *The Journal of Chemical Physics*, 70(8):3563–3571, 1979.

[143] GD Webber and PC Riedi. Broad band NMR spectrometer for the study of hyperfine fields in ferromagnetic materials. *Journal of Physics E: Scientific Instruments*, 14(10):1159–1163, 1981.

[144] *A Design of 10-100 MHz Broadband NMR Transmission-line Probe*, June 2023.

[145] Hermann Scharfetter, Andreas Petrovic, Heidi Eggenhofer, and Rudolf Stollberger. A no-tune no-match wideband probe for nuclear quadrupole resonance spectroscopy in the VHF range. *Measurement Science and Technology*, 25(12):125501, 2014.

[146] Timothy Hopper, Soumyajit Mandal, David Cory, Martin Hürlimann, and Yi-Qiao Song. Low-frequency NMR with a non-resonant circuit. *Journal of Magnetic Resonance*, 210(1):69–74, 2011.

[147] Juncheng Xu, Shouquan Yao, Yiqiao Song, Jianqi Li, and Yu Jiang. A balanced T/R switch for wideband NMR front-end. *IEEE Transactions on Circuits and Systems II: Express Briefs*, 71(5):2834–2838, 2024.

[148] Georgios N Kalantzopoulos, Fredrik Lundvall, Stefano Checchia, Anna ... Lind, and Bjørnar Arstad. In Situ Flow MAS NMR Spectroscopy and Synchrotron PDF Analyses of the Local Response of the Brønsted Acidic Site in SAPO-34 during Hydration at Elevated Temperatures. *ChemPhysChem*, 19(4):519–528, 2018.

[149] Jan G Korvink, Neil MacKinnon, Vlad Badilita, and Mazin Jouda. "Small is beautiful" in NMR. *Journal of Magnetic Resonance*, 306:112–117, 2019.

[150] Yael Maguire, Isaac L Chuang, Shuguang Zhang, and Neil Gershenfeld. Ultra-small-sample molecular structure detection using microslot waveguide nuclear spin resonance. *Proceedings of the National Academy of Sciences*, 104(22):9198–9203, 2007.

[151] Hans Georg Krojanski, Jörg Lambert, Yilmaz ... Gerikalan, and Roland Hergenröder. Microslot NMR probe for metabolomics studies. *Analytical chemistry*, 80(22):8668–8672, 2008.

[152] Manvendra Sharma, G ... Janssen, and PJM van Bentum. Rapid-melt dynamic nuclear polarization. *Journal of Magnetic Resonance*, 258:40–48, 2015.

[153] S G J Van Meerten, K C H Tijssen, P J M van Bentum, and A P M Kentgens. B1 gradient coherence selection using a tapered stripline. *Journal of Magnetic Resonance*, 286:60–67, 2018.

[154] Pedro F Silva, Mazin Jouda, and Jan G Korvink. Geometrically-differential NMR in a stripline front-end. *Journal of Magnetic Resonance*, 310:106659, 2020.

[155] J Schoenmaker, KR Pirota, and JC Teixeira. Magnetic flux amplification by Lenz lenses. *Review of Scientific Instruments*, 84(8):085120, 2013.

[156] Thomas Meier, Nan Wang, Dario Mager, Jan G Korvink, Sylvain Petitgirard, and Leonid Dubrovinsky. Magnetic flux tailoring through Lenz lenses for ultrasmall samples: A new pathway to high-pressure nuclear magnetic resonance. *Science advances*, 3(12):eaao5242, 2017.

[157] Thomas Meier, Saiana Khandarkhaeva, Jeroen Jacobs, Natalia Dubrovinskaia, and Leonid Dubrovinsky. Improving resolution of solid state NMR in dense molecular hydrogen. *Applied Physics Letters*, 115(13):131903, 2019.

[158] Seungtaek Jeong, Jinwook Song, Seongsoo Lee, Seokwoo Hong, Boogyo Sim, Hongseok Kim, Subin Kim, and Joungho Kim. Design, simulation and measurement of flexible PCB coils for wearable device wireless power transfer. In *2018 IEEE Wireless Power Transfer Conference (WPTC)*, pages 1–4. IEEE, 2018.

[159] Daniel Corzo, Guillermo Tostado-Blázquez, and Derya Baran. Flexible electronics: status, challenges and opportunities. *Frontiers in Electronics*, 1:594003, 2020.

[160] Cheng Deng, Shuang Li, and Jie Tang. A review of flexible multilayer foil integration technology for passive components. *IEEE Transactions on Power Electronics*, 36(11):13025–13038, 2021.

[161] Seungtaek Jeong, Tae-Wook Kim, Seongsoo Lee, Boogyo Sim, Hyunwook Park, Kyungjune Son, Keeyoung Son, Seongguk Kim, Taein Shin, Young-Cheon Kim, et al. Analysis of repetitive bending on flexible wireless power transfer (WPT) PCB coils for flexible wearable devices. *IEEE Transactions on Components, Packaging and Manufacturing Technology*, 12(11):1748–1756, 2022.

[162] Roberta Frass-Kriegl, Lucia Isabel Navarro de Lara, Michael Pichler, Jürgen Sieg, Ewald Moser, Christian Windischberger, and Elmar Laistler. Flexible 23-channel coil array for high-resolution magnetic resonance imaging at 3 Tesla. *PloS one*, 13(11):e0206963, 2018.

[163] Jana M Vincent and Joseph V Rispoli. Conductive thread-based stretchable and flexible radiofrequency coils for magnetic resonance imaging. *IEEE Transactions on Biomedical Engineering*, 67(8):2187–2193, 2019.

[164] Joseph R Corea, Anita M Flynn, Balthazar Lechêne, Greig Scott, Galen D Reed, Peter J Shin, Michael Lustig, and Ana C Arias. Screen-printed flexible MRI receive coils. *Nature communications*, 7(1):10839, 2016.

[165] F Bonetto, E Anoardo, and M Polello. Saddle coils for uniform static magnetic field generation in NMR experiments. *Concepts in Magnetic Resonance Part B: Magnetic Resonance Engineering: An Educational Journal*, 29(1):9–19, 2006.

[166] Carlos Ernesto Garrido Salmon, Edson Luiz Géa Vidoto, Mateus José Martins, and Alberto Tannús. Optimization of saddle coils for magnetic resonance imaging. *Brazilian Journal of Physics*, 36:4–8, 2006.

[167] Manvendra Sharma and Marcel Utz. Modular transmission line probes for microfluidic nuclear magnetic resonance spectroscopy and imaging. *Journal of Magnetic Resonance*, 303:75–81, 2019.

[168] Marek Plata, Manvendra Sharma, Marcel Utz, and Jörn M. Werner. Fully Automated Characterization of Protein–Peptide Binding by Microfluidic 2D NMR. *Journal of the American Chemical Society*, 145(5):3204–3210, 2023.

[169] Tatiana Trantidou, Anna Regoutz, Xian N. Voon, David J. Payne, and Oscar Ces. A "Cleanroom-Free" and Scalable Manufacturing Technology for the Microfluidic Generation of Lipid-Stabilized Droplets and Cell-Sized Multisomes. *Sensors and Actuators B: Chemical*, 267:34–41, August 2018.

[170] Sylvia Ehrler. PCB base material qualifications: discrepancies between supplier recommendations, customer expectations and reality. *Circuit World*, 39(2):67–74, 2013.

[171] Tong Zhang, Xu Chen, José E Schutt-Ainé, and Andreas C Cangellaris. Statistical analysis of fiber weave effect over differential microstrips on printed circuit boards. In *2014 IEEE 18th Workshop on Signal and Power Integrity (SPI)*, pages 1–4. IEEE, 2014.

[172] Lambert Simonovich. Practical fiber weave effect modeling. *Technical Paper, Lamsim Enterprise Inc*, 20, 2011.

[173] V. Badilita, Robert Ch Meier, Nils Spengler, Ulrike Wallrabe, Marcel Utz, and Jan G Korvink. Microscale nuclear magnetic resonance: a tool for soft matter research. *Soft Matter*, 8(41):10583–10597, 2012.

[174] RRA Syms, MM Ahmad, IR Young, DJ Gilderdale, and DJ Collins. Microengineered needle micro-coils for magnetic resonance spectroscopy. *Journal of Micromechanics and Microengineering*, 16(12):2755, 2006.

[175] E Loskot, V Kondratiev, I Vendik, E Jakku, and S Leppavuori. Design of resonators and filters based on LTCC lumped components. In *2000 30th European Microwave Conference*, pages 1–4. IEEE, 2000.

[176] Torsten Thelemann, Heiko Thust, and Michael Hintz. Using LTCC for microsystems. *Microelectronics International*, 19(3):19–23, 2002.

[177] Goran J Radosavljevic, Ljiljana D Zivanov, Walter Smetana, Andrea M Maric, Michael Unger, and Laslo F Nad. A wireless embedded resonant pressure sensor fabricated in the standard LTCC technology. *IEEE Sensors Journal*, 9(12):1956–1962, 2009.

[178] Ji Zhou. Towards rational design of low-temperature co-fired ceramic (LTCC) materials. *Journal of Advanced Ceramics*, 1:89–99, 2012.

[179] Mailadil T Sebastian and Heli Jantunen. Low loss dielectric materials for LTCC applications: a review. *International Materials Reviews*, 53(2):57–90, 2008.

[180] Pero Krivic. Introduction of LTCC Technology in Fabrication of the Planar Microcoils for NMR Spectroscopy. *Advanced Materials Research*, 685:362–366, 2013.

[181] Ēriks Kupče, Ray Freeman, and Boban K John. Parallel acquisition of two-dimensional NMR spectra of several nuclear species. *Journal of the American Chemical Society*, 128(30):9606–9607, 2006.

[182] Ēriks Kupče. NMR with multiple receivers. *Modern NMR Methodology*, pages 71–96, 2013.

[183] Eulalia Serés Roig, Arthur W Magill, Guillaume Donati, Martin Meyerspeer, Lijing Xin, Ozlem Ipek, and Rolf Gruetter. A double-quadrature radiofrequency coil design for proton-decoupled carbon-13 magnetic resonance spectroscopy in humans at 7T. *Magnetic Resonance in Medicine*, 73(2):894–900, 2015.

[184] Stuart B. Adler, James N. Michaels, and Jeffrey A. Reimer. A compact, high temperature nuclear magnetic resonance probe for use in a narrow–bore superconducting magnet. *Review of Scientific Instruments*, 61(11):3368–3371, 1990.

[185] Markus Beck Erlach, Claudia E. Munte, Werner Kremer, Rainer Hartl, Dörte Rochelt, Dieter Niesner, and Hans Robert Kalbitzer. Ceramic cells for high pressure NMR spectroscopy of proteins. *Journal of magnetic resonance (San Diego, Calif. : 1997)*, 204(2):196–199, 2010.

[186] Harm Ridder, Christoph Sinn, Georg R. Pesch, Jan Ilsemann, Wolfgang Dreher, and Jorg Thöming. A large fixed bed reactor for MRI operando experiments at elevated temperature and pressure. *Review of Scientific Instruments*, 92(4):043711, 2021.

[187] LJ Golonka. Technology and applications of low temperature cofired ceramic (LTCC) based sensors and microsystems. *Bulletin of the Polish Academy of Sciences Technical Sciences*, pages 221–231, 2006.

[188] VIA Electronic GmbH, Thuringia, Germany. *LTCC system and LTCC design rules*, 11 2016.

[189] Stefan Leidich, Marco Braun, Thomas Gessner, and Thomas Riemer. Silicon cylinder spiral coil for nuclear magnetic resonance spectroscopy of nanoliter samples. *Concepts in Magnetic Resonance Part B: Magnetic Resonance Engineering: An Educational Journal*, 35(1):11–22, 2009.

[190] P Andris, J Weis, and I Frollo. Magnetic field of spiral-shaped coil. In *Proc. of the 7th Int. Conf. on Measurement, Bratislava, Institute of Measurement Science SAS*, pages 262–265, 2009.

[191] Piotr Lepucki, Adam P. Dioguardi, Daniil Karnaushenko, Oliver G. Schmidt, and Hans-Joachim Grafe. The Normalized Limit of Detection in NMR Spectroscopy. *Journal of Magnetic Resonance*, 332:107077, 2021.

[192] Alessandro Bagno, Federico Rastrelli, and Giacomo Saielli. Prediction of the 1H and 13C NMR spectra of α-D-glucose in water by DFT methods and MD simulations. *The Journal of Organic Chemistry*, 72(19):7373–7381, 2007.

[193] Elin Alexandersson and Gustav Nestor. Complete 1H and 13C NMR spectral assignment of D-glucofuranose. *Carbohydrate Research*, 511:108477, 2022.

[194] Qiang Yang, Shengfei Zhou, and Troy Runge. Magnetically separable base catalysts for isomerization of glucose to fructose. *Journal of Catalysis*, 330:474–484, 2015.

[195] Jonathan D Trumbull, Ian K Glasgow, David J Beebe, and Richard L Magin. Integrating microfabricated fluidic systems and NMR spectroscopy. *IEEE Transactions on Biomedical Engineering*, 47(1):3–7, 2000.

[196] Ēriks Kupče, Ray Freeman, and Boban K John. Parallel acquisition of two-dimensional NMR spectra of several nuclear species. *Journal of the American Chemical Society*, 128(30):9606–9607, 2006.

[197] Ēriks Kupče, Kaustubh R Mote, Andrew Webb, Perunthiruthy K Madhu, and Tim DW Claridge. Multiplexing experiments in NMR and multi-nuclear MRI. *Progress in Nuclear Magnetic Resonance Spectroscopy*, 124:1–56, 2021.

[198] Vaibhav Kumar Shukla, Gabriella T Heller, and D Flemming Hansen. Biomolecular NMR spectroscopy in the era of artificial intelligence. *Structure*, 31(11):1360–1374, 2023.

[199] VS Manu, Marco Tonelli, Bailey Bell, Alok K Sharma, Tim S Bugni, and Gianluigi Veglia. Detection of 15 N-labeled metabolites in microbial extracts using AI-designed broadband pulses for 1 H, 15 N heteronuclear NMR spectroscopy. *Analyst*, 150(9):1856–1861, 2025.

[200] VS Manu, Cristina Olivieri, and Gianluigi Veglia. AI-designed NMR spectroscopy RF pulses for fast acquisition at high and ultra-high magnetic fields. *Nature communications*, 14(1):4144, 2023.

[201] Moritz Becker, Soeren Lehmkuhl, Stefan Kesselheim, Jan G Korvink, and Mazin Jouda. Acquisitions with random shim values enhance AI-driven NMR shimming. *Journal of Magnetic Resonance*, 345:107323, 2022.

[202] D Flemming Hansen. Using deep neural networks to reconstruct non-uniformly sampled NMR spectra. *Journal of biomolecular NMR*, 73(10):577–585, 2019.

[203] Yutong Chen, Carola-Bibiane Schönlieb, Pietro Liò, Tim Leiner, Pier Luigi Dragotti, Ge Wang, Daniel Rueckert, David Firmin, and Guang Yang. AI-based reconstruction for fast MRI—a systematic review and meta-analysis. *Proceedings of the IEEE*, 110(2):224–245, 2022.

[204] Edward Bennett Rosa. *The self and mutual inductances of linear conductors*. US Department of Commerce and Labor, Bureau of Standards, 1908.

[205] Lei Dong, Li-Feng Wang, and Qing-An Huang. Implementation of multiparameter monitoring by an LC-type passive wireless sensor through specific winding stacked inductors. *IEEE Internet of Things Journal*, 2(2):168–174, 2014.

Publications

Journal Articles

[J1] **Jianyi Liang**, Hossein Davoodi, Sagar Wadhwa, Vlad Badilita, and Jan G. Korvink. Broadband stripline Lenz lens achieves 11× NMR signal enhancement, *Scientific Reports*, **2024**, 14(1), 1645.

[J2] **Jianyi Liang**, Hossein Davoodi, Khai Chau-Nguyen, Vlad Badilita, and Jan G. Korvink. Split spiral broadband double channel NMR detector facilitated by LTCC technology, *Scientific Reports*, **2025**, 15(1), 20162.

Conference contributions

[C1] **Jianyi Liang**, Hossein Davoodi, Vlad Badilita, and Jan G. Korvink. Stripline Lenz lens add-on with one order of magnitude signal enhancement. 43rd FGMR Annual Discussion Meeting, Karlsruhe, Germany, **2022**. Poster Presentation

[C2] **Jianyi Liang**, Hossein Davoodi, Vlad Badilita, and Jan G. Korvink. Stripline Lenz lens add-on with one order of magnitude signal enhancement. 64th Experimental Nuclear Magnetic Resonance Conference (ENC), California, USA, **2023**. Poster Presentation.

List of Figures

List of Tables

Appendix

A1 Material Properties

Table A1: *Material properties used for COMSOL simulations.*

Material	χ (ppm)	ϵ_r	σ (S/m)	**Source**
Gold	-34	1	4.1×10^{7}	COMSOL Library
Copper	-9.6	1	6.0×10^{7}	COMSOL Library
Water	-9.0	80	5.5×10^{-6}	COMSOL Library
Ordyl (SY300)	-8	3.5	1.0×10^{-12}	COMSOL Library
LTCC (DuPont 951)	-10	7.8	1.0×10^{-12}	COMSOL Library
Glass (D263)	-11	4.6	1.0×10^{-6}	SCHOTT
Air	0	1	0	COMSOL Library

A2 Electrical model of the S3L resonator

In this section, we present the full derivation and calculation of the equations shown in Sec. **Equivalent circuit for stripline Lenz lens** in Chap. 3. As shown in Fig. 3.2, we have the saddle coil and two identical Lenz lens loops modeled as RL circuits respectively. Mutual inductance exists between any two of the three coils. H and D are respectively the height and the diameter of the saddle coil, conventionally 20 mm and 10 mm for a wide range of NMR magnets. To best fit in the saddle coil with a maximum filling factor, we assume the side lengths of the Lenz lens loop to be $l \times m = 16mm \times 4mm$, the width of the middle stripline w to be 200 µm and the rest segments to be 6 times wider, i.e., 1200 µm based on typical stripline design rules [88], which increases the current density inside the central stripline by 6-fold. 20 µm is adopted for the track thickness t considering the skin depth effect at a working frequency of 500 MHz and the fabrication constraints.

Based on previous theoretical study of Lenz lens device[25], the voltage seen at the terminal of the "loaded" saddle coil v_x, i.e., when the S3L is inserted as shown in Fig. A1, is given by the difference between the voltage of the "unloaded" saddle coil, i.e., without the S3L, and the induced voltages due to the coupling between the saddle coil and the each of the loops of the S3L, alternatively loop α and loop β:

$$v_x = (R_s + j\omega L_s)i - v_\alpha - v_\beta, \tag{A1}$$

in which R_s and L_s are the resistance and inductance of the saddle coil, i is the current inside the saddle coil, ω is the working frequency.

By definition, the induced voltages depend on the mutual inductance between the saddle coil and loops α and β (Eq. A2). Due to the symmetry reasons, electrical parameters denoted with α and β have the same values, i.e., $v_\alpha = v_\beta$, and also $R(L)_\alpha = R(L)_\beta, M_{s\alpha} = M_{s\beta}, M_{\alpha\beta} = M_{\beta\alpha}$ and $i_\alpha = i_\beta$ appearing in following equations:

$$v_\alpha = v_\beta = j\omega M_{s\alpha} i_\alpha. \tag{A2}$$

$M_{s\alpha}$ represents the mutual inductance between the saddle coil and either Lenz lens loop, and i_α is the current in one Lenz lens loop. Thus, the impedance seen at the terminals of the "loaded" saddle coil is given by the ratio between the voltage at the terminals of and the current in the loaded saddle coil in Eq. A3: [25]

$$Z_x = \frac{v_x}{i_s} = R_s + j\omega L_s - 2j\omega M_{s\alpha}\frac{i_\alpha}{i_s}. \tag{A3}$$

Here, $v_{s\alpha}$ is the voltage induced in loop α by the saddle coil. This can be written as Eq. A4 taking into account also the mutual coupling between the two loops of the S3L:

$$v_{s\alpha} = i_\alpha(R_\alpha + j\omega L_\alpha) - v_{\alpha\beta}, \tag{A4}$$

where R_α and L_α are the resistance and inductance of one Lenz lens loop, and $v_{\alpha\beta}$ is the voltage induced in one loop α by the β. The induced voltages have also been expressed according to the definition as a function of mutual inductance in Eq. A5:

$$v_{s\alpha} = j\omega M_{s\alpha} i_s, v_{\alpha\beta} = j\omega M_{\alpha\beta} i_\alpha, \tag{A5}$$

where $M_{\alpha\beta}$ is the mutual inductance between two Lenz lens loops. With the current in loop α being expressed as Eq. A6 according to Eq. A4, we obtain the ratio of the two currents after some algebraic calculation as Eq. A7, which is one of the ratios used to calculate the SNR enhancement in Fig. 2 (c).

$$i_\alpha = \frac{v_{s\alpha} + v_{\alpha\beta}}{R_\alpha + jwL_\alpha} = \frac{j\omega(M_{s\alpha}i_s + M_{\alpha\beta}i_\alpha)}{R_\alpha + j\omega L_\alpha}, \tag{A6}$$

$$\frac{i_\alpha}{i_s} = \frac{j\omega M_{s\alpha}}{R_\alpha + j\omega(L_\alpha - M_{\alpha\beta})}. \tag{A7}$$

We replace these current ratios in the expression of impedance from Eq. A3, and Z_x now is described by Eq. A8:

$$Z_x = R_s + j\omega L_s + \frac{2\omega^2 M_{s\alpha}^2}{R_\alpha + j\omega(L_\alpha - M_{\alpha\beta})} \triangleq R_s + jwL_x. \tag{A8}$$

The real part can be isolated as in Eq. A9:

$$R_x = R_s + \frac{2\omega^2 M_{s\alpha}^2 R_\alpha}{R_\alpha^2 + \omega^2(L_\alpha - M_{\alpha\beta})^2}. \tag{A9}$$

We further express the ratio of the two resistances, where each value on the right-hand side of the equation is being calculated individually starting from the actual dimensions of the saddle coil and loop, respectively:

$$\frac{R_x}{R_s} = 1 + \frac{2\omega^2 M_{s\alpha}^2 R_\alpha}{R_s\,(R_\alpha^2 + \omega^2(L_\alpha - M_{\alpha\beta})^2)} \triangleq \gamma. \tag{A10}$$

This is the second ratio that makes up the SNR enhancement. According to the reference [165], the B_1-field at the geometric center of a saddle coil is given by Eq. A11, which is the sum total of the magnetic fields by four arcs and four strips. In addition, it can be seen as homogeneous considering the ultra small sample volume compared to the saddle coil space:

$$\begin{aligned} B_{1,s} &= 4(B_{1,arc} + B_{1,strip}) \\ &= \frac{\sqrt{3}\mu_0 D i_s H}{4\pi}\left(\frac{1}{(D^2/4 + H^2/4)^{3/2}} + \frac{1}{D^2/4(D^2/4 + H^2/4)^{1/2}}\right) \\ &= \frac{\sqrt{3}\mu_0 i_s H\left(D^2/2 + H^2/4\right)}{\pi D\left(D^2/4 + H^2/4\right)^{3/2}}, \end{aligned} \tag{A11}$$

in which $B_{1,arc}$ and $B_{1,strip}$ are field components from one arc and one strip in the saddle coil. μ_0 is the magnetic permeability in air, equal to $4\pi \times 10^{-7}$H/m.

As shown in Fig. 1 (b), the RF field in S3L, $B_{1,S3L}$, is confined by two parallel stripline segments and can be calculated according to Biot Savart Law from two current-carrying conductors. The local field strength at distance x from one stripline surface is calculated and further integrated between two striplines for the average field strength between two striplines:

$$\begin{aligned} B'_{1,S3L} &= \frac{i_\alpha \mu_0}{2\pi}\left(\frac{1}{x} + \frac{1}{h-x}\right), \\ B_{1,S3L} &= \frac{1}{h-2t}\int_t^{h-t} B'_{1,S3L}\mathrm{d}x \\ &= \frac{i_\alpha \mu_0}{2\pi(h-2t)}\ln\left(\frac{h-t}{t}\right), \end{aligned} \tag{A12}$$

in which t is the thickness of the track. The integration range starting from t is for the valid sample region and it avoids the calculation error by applying zero in logarithmic equation. A combination of Eq. A11 and Eq. A12 generates the ratio $\eta = B_{1,S3L}/B_{1,s}$, which is plotted in Fig. A1 (a).

Before proceeding the numerical result of R_s/R_x and i_α/i_s, we need to calculate the unknown parameters in the equations, i.e., R_s, R_α, L_α and $M_{s\alpha}$, $M_{\alpha\beta}$. The AC resistance and inductance of the Lenz lens loop, R_α and L_α can be determined by following empirical equations for the self-resistance and inductance of a rectangular strip conductor [204].

$$\begin{aligned} R_\alpha &= \frac{l}{2(a+t)\delta\sigma}, \\ L_\alpha &= 2l\left(\ln\frac{2l}{a+t} + 0.5 + 0.2235\frac{(a+t)}{l}\right), \end{aligned} \tag{A13}$$

where δ is the skin effect depth, σ is the conductivity. As the saddle coil is a standard NMR detector, the calculation of its impedance values are not discussed here. By applying dimension values above to the Eq. A13, R_s, R_α, L_α are respectively 0.546 Ω, 0.265 Ω and 35.5 nH at 500 MHz for proton measurement.

The parameters still missing are the mutual inductance between one single loop and the saddle coil $M_{s\alpha}$, and the mutual inductance between two loops $M_{\alpha\beta}$. The magnetic flux differential is proportional to the field strength differential and a constant area of the receiving loop as Eq. A14 [205].

$$\mathrm{d}\Phi_{s\alpha} = \mathrm{d}AB_s. \tag{A14}$$

The relationship between the magnetic flux received by a single Lenz lens loop and the mutual inductance is defined as Eq. A15

$$\frac{\mathrm{d}\Phi_{s\alpha}}{\mathrm{d}t} = \frac{\mathrm{d}i_s}{\mathrm{d}t}M_{s\alpha}. \tag{A15}$$

In the equations above, $\Phi_{s\alpha}$ is the saddle-generated magnetic flux onto the loop and A is the area of the secondary coil perpendicular to the magnetic flux. $A = l \times m \approx \frac{1}{2}DH$ when the Lenz lenses take up a maximal cross section area inside the saddle coil.

By combining Eq. A11, A14 and A15, we obtain the expression of $M_{s\alpha}$ and further exact values with the given dimensions of the saddle coil and the Lenz lens loops

$$M_{s\alpha} = \frac{B_{1,s}}{i_s}A = \frac{\sqrt{3}\mu_0 H^2\left(D^2/2 + H^2/4\right)}{\left(2\pi D^2/4 + H^2/4\right)^{3/2}} \approx 1.49 \times 10^{-8}. \tag{A16}$$

The magnetic flux from one loop onto the other is equal to the flux difference by two long-side strips in the loop carrying opposite-direction currents, denoted as Eq. A17, while two short-side strips are not affecting the coupling. The differential magnetic flux by an l long conductor from the loop can be calculated as Eq. A18b according to Biot Savart Law and is integrated in respective distance ranges for Φ_1 and Φ_2

$$\Phi_{\alpha\beta} = \Phi_1 - \Phi_2. \tag{A17}$$

The flux terms are described by

$$\mathrm{d}\Phi = \frac{\mu_0 i_\alpha}{2\pi r} l \mathrm{d}x, \tag{A18a}$$

$$\Phi_1 = \int_0^m \frac{\mu_0 i_\alpha l}{2\pi\sqrt{x^2+h^2}} x \mathrm{d}x, \tag{A18b}$$

$$\Phi_2 = \int_m^{2m} \frac{\mu_0 i_\alpha l}{2\pi\sqrt{x^2+h^2}} x \mathrm{d}x, \tag{A18c}$$

in which r is the distance from the loop to the strip. In a similar way as Eq. A14 and A15, $M_{\alpha\beta}$ can be calculated from Eq. A18 as following:

$$\begin{aligned} \frac{\mathrm{d}\Phi_{\alpha\beta}}{\mathrm{d}t} &= \frac{\mathrm{d}i_\alpha}{\mathrm{d}t} M_{\alpha\beta}, \\ M_{\alpha\beta} &= \frac{\mu_0 l}{4\pi}\left(2\ln(m^2+h^2) - \ln(h^2) - \ln(4m^2+h^2)\right). \end{aligned} \tag{A19}$$

Since two mutual inductances are clear now, we get back to the Eq. A7 and Eq. A10 and then, R_s/R_x over the change of h is shown in Fig. A1 (b). Now we combine two elements together and obtain the SNR enhancement at 500 MHz, as shown in Fig. 1 (b) in the main text. The results show that a dominant SNR enhancement comes from the RF field enhancement due to the inserted S3L chip. However, a higher resistance at the saddle coil, which in fact degrades the SNR slightly.

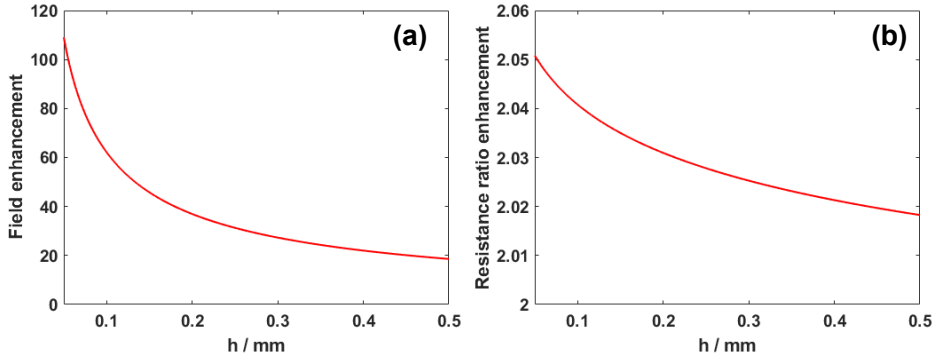

Figure A1: *Parameter change vs. vs. stripling spacing h. (a) B_1 magnification at unit current. (b) terminal resistance.*

A3 Matlab code for COMSOL processing

```
clear all;
clc

%   GUI: user's input
prompt = {'Frequency (MHz):', 'Power (W)', 'Spectral resolution (ppb)', 'sample length (um)','sample width (um)', 'sample height (um)'};
dlg_title = 'Input';
num_lines = 1;
defaultans = {'500', '1', '1', '200', '200', '1000'}; % assuming a 200*200*1000 um^3 sample space, at 500 MHz
ans = inputdlg(prompt,dlg_title,num_lines,defaultans);

LarmorFreq=str2num(ans{1})*1e6;
P=str2num(ans{2});
spec_resolution=str2num(ans{3})*1e-9;
d=str2num(ans{4})*1e-6;
d1=str2num(ans{5})*1e-6;
h=str2num(ans{6})*1e-6;
B00=11.74;
gamma=LarmorFreq/B00;

%   Nutation signal
t=[0:0.5e-6:500e-6];
nut_signal(:,1)=t';
NMRspectra=[-10:spec_resolution*1e6:10]';


%   Sampling datapoints
%   Origin of the coordinate is the center of the twin-stripline structure
stepsize=10e-6;
x00=stepsize:stepsize:d/2;
x0=[-fliplr(x00),0,x00];  % length
y00=stepsize:stepsize:d1/2;
y0=[-fliplr(y00),0,y00];  % width
z00=stepsize:stepsize:h/2;
z0=[-fliplr(z00),0,z00]; % height

[x,y,z]=meshgrid(x0,y0,z0);
```

```
xyz= sqrt(x(:).^2+y(:).^2)<d/2;
% adjustment for a cuboid
% xyz= sqrt(x(:).^2+y(:).^2)<d/2; applied for a cylinder sample
% real sample then xyz returns with 1

sample0=[x(:),y(:),z(:)];
% a random point within the sample region, which is still a box
sample1=[xyz, sample0];
sample2=sortrows(sample1,1);
sample3=sample2(length(xyz)-sum(xyz)+1:length(xyz),:);
sample=(sample3(:,2:4))';

%   GUI: Read B1 simulation file and import data
[file] = uigetfile({'.mph'},'Select a simulation file for B1');
model_B1=mphopen(file);

for i=1
    % check the model and the axes for each different projects
  B1 = mphinterp(model_B1,'abs(sqrt((emw.Bx)^2+(emw.By)^2))','coord
     ',sample, 'dataset','dset2', 'outersolnum',i)';
  impedance = mphglobal(model_B1,'emw.Zport_1', 'dataset','dset2',
     'outersolnum',I);
%   Read the field and impedance data at the frequency of interest,
    e.g. 500 MHz
  B1150(:,i)=B1(:,1);
  B1500(:,i)=B1(:,1);
  imp150(:,i)=impedance(1);
  imp500(:,i)=impedance(1);

%   B1 field simulations performed for 1A current applied to the
   coil
B1=B1500(:,I);  % data at 500 MHz
impedance=imp500(:,i);
I= sqrt(P/real(impedance));

%   Nuttion curve
theta=B1*t*I*gamma;
nut_sig=B1'*sin(2*pi*theta);
nut_signal(:,i+1)=nut_sig';
% Before, the first colume of nut_signal is already defined.
plot(nut_signal(:,1),nut_signal(:,i+1))
```

```
74
75 % Figures of merits
76 B1u(i)=mean(B1);       % Ave(B1) per unit applied current
77 F=10^(1/10);        % Amplifier noise figure defined by the
      hardware in the lab,    1 for 500MHz and 2 for others
78 V_FID=max(nut_signal(:,i+1));
79 Impreal(i) = real(impedance);
80 Impimag(i) = imag(impedance);
81 etta(i)=V_FID./sqrt(F*Impreal(i)); % Defined sensitivity
82
83 [iii,i90m]=max(nut_signal(:,i+1));
84 Tm(i)=t(i90m);                  % 90degree pulse length
85 exc_eff(i)=pi/2./Tm(i);           % Excitation efficiency
86
87 [iiii,i810m]=max(nut_signal(8*i90m:10*i90m,i+1));
88 % 810degree pulse length over a wide range with different I.
89 % Note: this scanning range should be adjusted considering the
      quality of the generated mutations
90
91 B1_hom(i)=iiii/iii;     % B1 homogeneity
92 %SS=max(nut_signal(:,2:3))./max(NMRspectra(:,2:3)); for spectral
      sharpness
93 end
94 n(1,:) = [1:i];
95 Output=[n', Impreal', B1u',  etta', Tm', exc_eff', B1_hom', Impimag
      '];%, SS'];
96
97 %  Export data
98 [FileName, PathName, FilterIndex] = uiputfile('*', 'Save data as:')
      ;
99 if ~ischar(FileName)
100     disp('User aborted the dialog! Data are NOT exported.');
101 else
102     exportfilename =strcat(FileName, '_NutSignal.txt');
103     File= fullfile(PathName, exportfilename);
104     dlmwrite(File,nut_signal,'delimiter', '\t', 'precision', 6)
105
106     exportfilename =strcat(FileName, '_FoM.txt');
107     File= fullfile(PathName, exportfilename);
108     dlmwrite(File ,Output,'delimiter', '\t', 'precision', 5) %
        figures of merit
```

```
109
110     disp(strcat('Data are exported as:', {' '}, FileName, '
            _NutSignal.txt and',{' '}, FileName, '_NMRSpectrum.txt. They
             can be found in:', {' '}, PathName));
111 end
112
113 %%% Following optional code for NMR spectrum simulation and
        plotting
114
115 %   GUI: Read B0 simulation file and import data
116 [file] = uigetfile({'.mph'},'Select a simulation file for B0');
117 model_B0=mphopen(file0);
118 B0 = 1/B00*round(1/spec_resolution*abs((mphinterp(model_B0,'mfnc.Bz
        ','coord',sample)')))*spec_resolution;    % normalised to B00
119
120 %   NMR spectrum
121 tau=nut_signal(find(nut_signal(:,i+1)==max(nut_signal(:,i+1))),1);
122 weight= B1.*sin(2*pi*B1*tau*I_inuse*gamma);                %
        amplitude of signal from each voxel at 90degree flip angel
123 subs=round(1/spec_resolution*(B0-min(B0))+1);  %generate bins for
        spectrum
124 bins=round(1/spec_resolution*(max(B0)-min(B0))+1);
125 histw = accumarray(subs,weight,[bins,1]);   % signal intensity
        considering B1 homogeneity as a function of B0
126 xx=(min(B0)+[1:bins]*spec_resolution)*1e6; %ppm
127 xx= xx-xx(find(histw==max(histw))); % adjust the chimacal shift
128
129 lowerband=[-10:spec_resolution*1e6:min(xx)];
130 upperband=[max(xx)+spec_resolution*1e6:spec_resolution*1e6:10+2*
        spec_resolution];
131 NMRspectrum=[lowerband, xx,  upperband; 0*lowerband, histw', 0*
        upperband]';
132 NMRspectra(:,i+1)=NMRspectrum(1:round(20/(spec_resolution*1e6)+1)
        ,2);
133
134 %   Plot data
135 subplot(2,1,1), plot(nut_signal(:,1),nut_signal(:,2))
136 hold on
137 subplot(2,1,2), plot(NMRspectra(:,1),NMRspectra(:,2))
138
139 %   Export data
```

```
exportfilename =strcat(FileName, '_NMRSpectra.txt');
File= fullfile(PathName, exportfilename);
dlmwrite(File,NMRspectra,'delimiter', '\t', 'precision', 6)
```

A4 Clean room fabrication process

This process flow is applied to the fabrication of broadband stripline Lenz lens detector in **Chapter 3**.

Table A2: *Clean room fabrication process flow.*

Nr.	Operation	Description
1	**Wafer surface cleaning**	• Rinsing in acetone → IPA → acetone → IPA → DI Water • N_2 blow-drying • Dehydration bake at 200 °C
2	**Seed layer deposition**	• Cr (20 nm) → Au (60 nm)
3	**Lithography**	
3.1	**Wafer surface cleaning**	• Rinsing in acetone → IPA → acetone → IPA → DI Water • N_2 blow-drying • Dehydration bake at 200 °C
3.2	**Spincoating**	• Spincoating SU-8 for (20 µm) • Soft bake at 95 °C for 15 min
3.3	**UV exposure**	• Intensity of 320 mJ cm^{-2} • Post exposure bake at 95 °C for 4 min
3.4	**Photoresist development**	• 10 min development in PGMEA • Rinsing in IPA for 5 min • Rinsing in DI water, N_2 blow-drying
4	**Electroplating of conductor**	
4.1	**O_2 plasma of the surface**	• Duration depends on the residual resist condition • Optional: dehydration bake at 30 °C for 24 h
4.2	**Electroplating**	• Au thickness: 15 µm to 20 µm • Rinsing in IPA → DI Water → N_2 blow-drying • Dehydration bake at 30 °C for 24 h
5	**Resist removal**	• 22 °C, 1200 W, 1 h in R3T
6	**Electroplating of conductor**	
6.1	**Etching of seed layers**	• Au etching • Cr etching
6.2	**Cleaning and plasma treatment**	• Rinsing in acetone → IPA → acetone → IPA → DI Water • N_2 blow-drying • Dehydration bake at 200 °C for 5 min
7	**Ordyl lamination**	• O_2 plasma • Lamination of Ordyl layers (SY390, 90 µm) level 2 speed at 85 °C (hot roll laminator) • Soft bake: 1 min, 85 °C, remove plastic film • This operation can be repeated for a multi-layer substrate. The plastic film on the top layer should not be removed.
8	**UV exposure**	• Wafer-mask alignment with mask aligner) Exposure to UV source at around 200 mJ cm^{-2} • Post exposure bake at 1 min at 85 °C • Remove last film before development
9	**Ordyl development**	• 20 min in Ordyl SY developer • Ultrasound bath for 5 min • Rinse in DI water → N_2 blow dry
10	**Bonding with glass wafer**	• Compressed bonding (Steps 8.1–

		8.2 should happen without interruption for good bonding) • Dehydration bake at 30 °C, 24 h
11	**Final machining of holes and dicing**	• Inlet and outlet drilling • CO_2 laser dicing • Optional: injection of glue into the chamber

A5 Technical drawings

A5.1 Layout for S3L chips

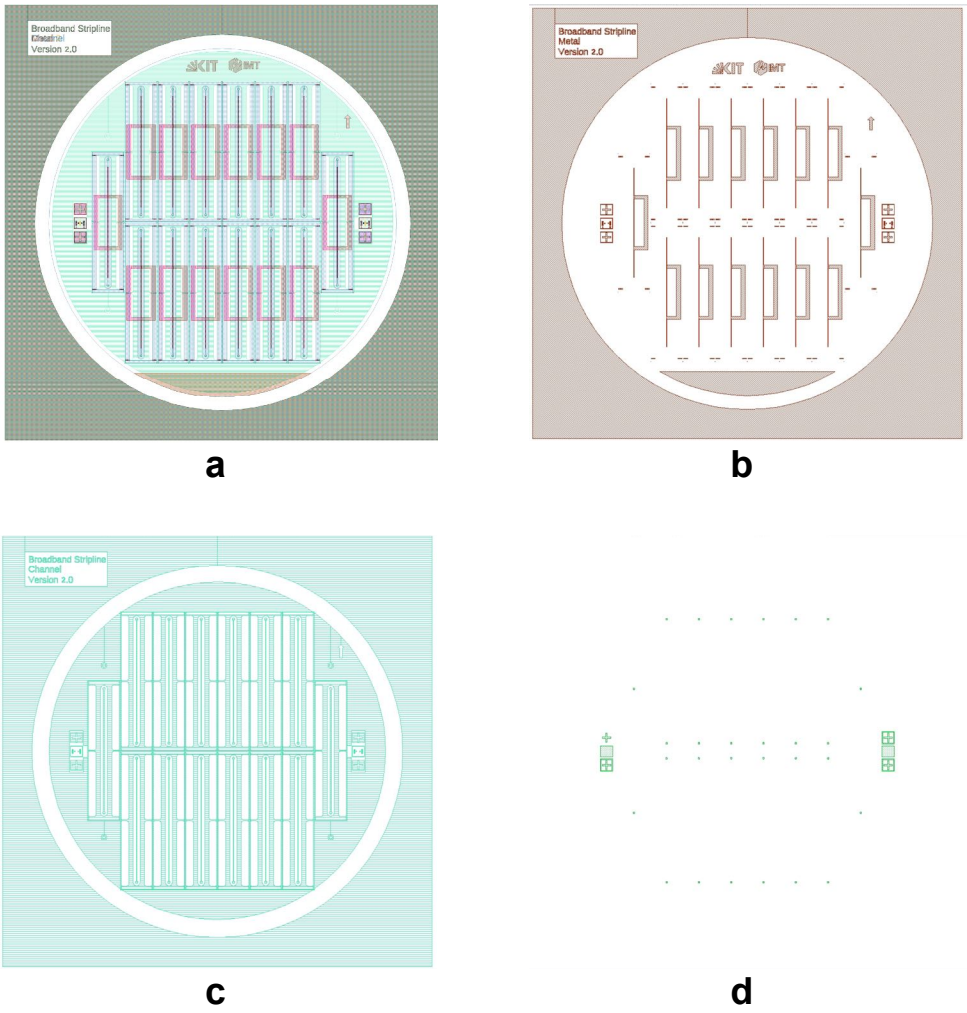

Figure A2: *Mask design of glass-based stripline chip layout for clean room fabrication. The glass wafer has a diameter of* 10 cm. *(a) Assembly of all masks in alignment, showing the final chip structures. The central round space is a 10-inch glass wafer. (b) Mask design of the gold conductor together with alignment marks. The disk segment at the bottom of the wafer is the pad connected to the source in conductor electroplating. (c) Mask design for photoresist lithography of channel walls and alignment marks. (d) Mask design for laser-cutting of inlets and outlets.*

A5.2 Supporters for the saddle coil and S3L

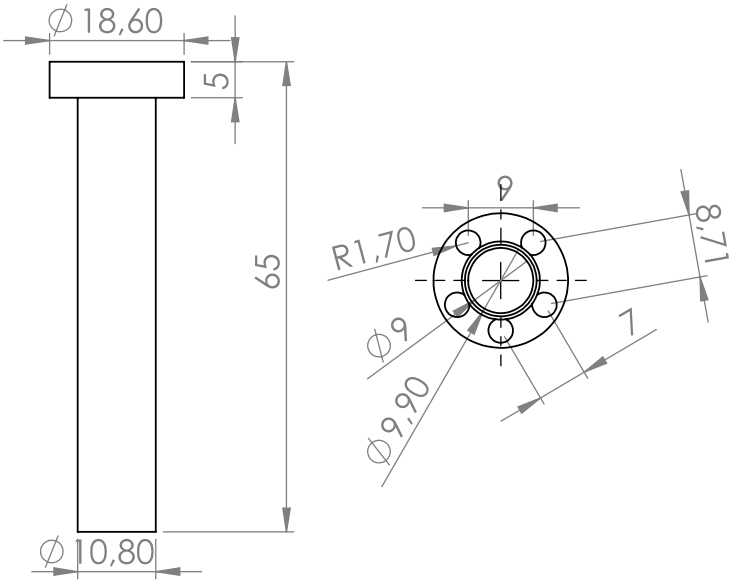

Figure A3: *3D-printed supporter design for the flexible PCB (*mm*).*

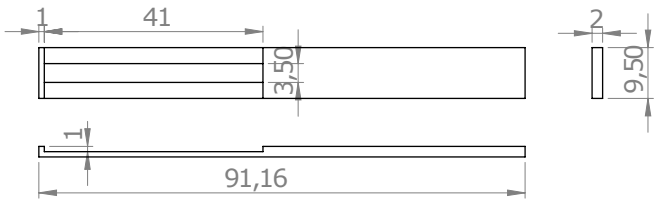

Figure A4: *Supporter design for the stripline Lenz lens chip (*mm*).*

A5.3 Layout for broadband spirals

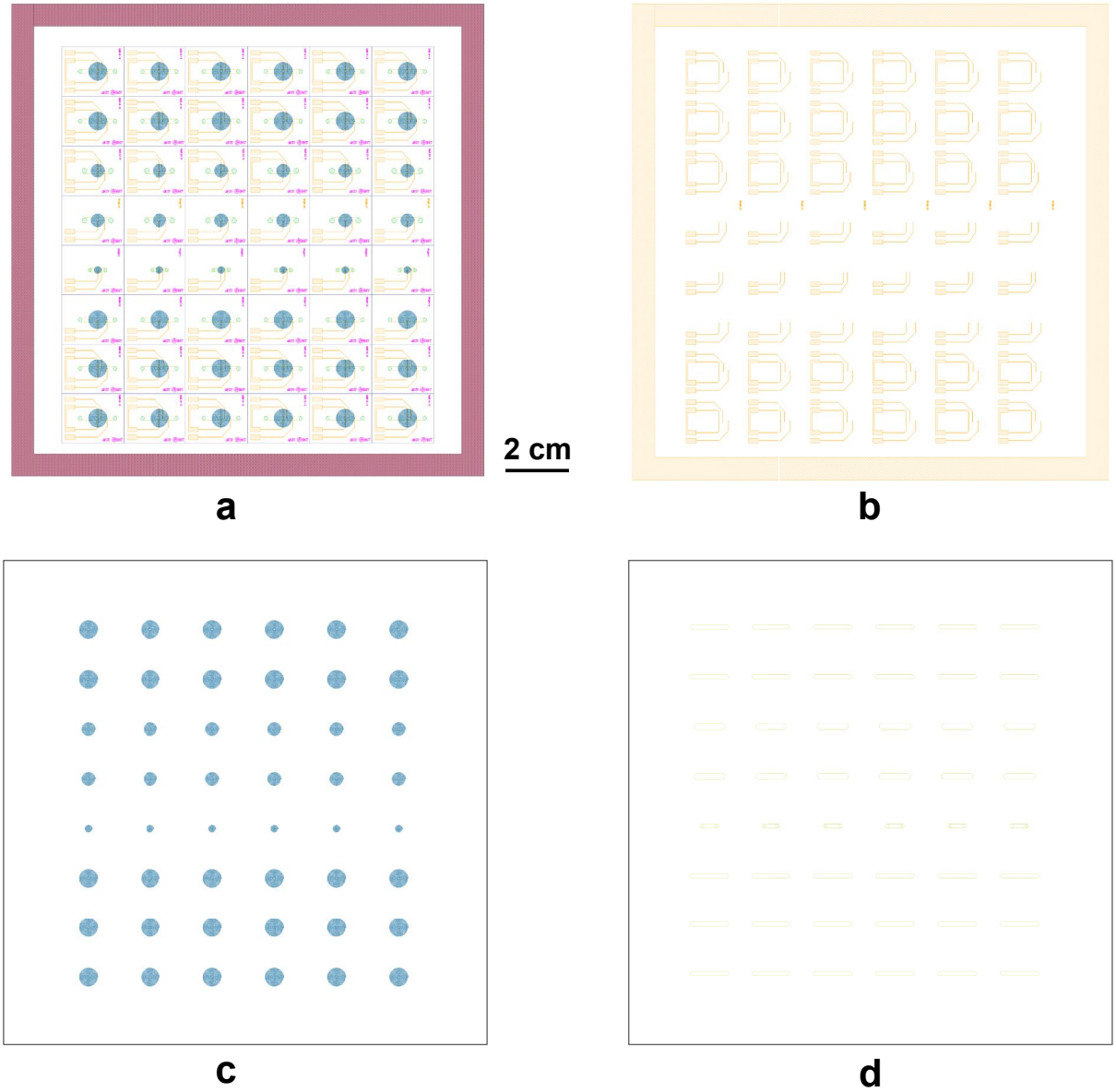

Figure A5: *Layout designs for LTCC fabrication of a batch of various broadband spiral chips. (a) Complete layout with all structures. (b) Conductor track layout on the top layer. (c) Embedded spiral layout on the second layer from the top. (d) Embedded fluidic channel layout on the third layer from the top.*

A5.4 Supporter for LTCC-based chip

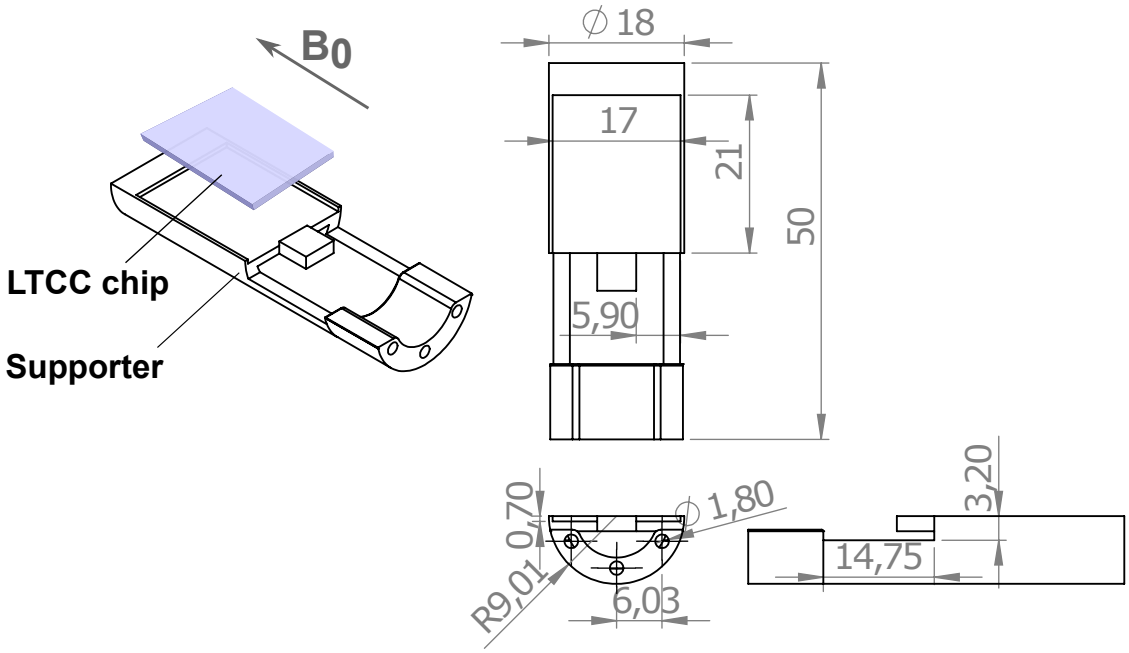

Figure A6: *Assembly of the chip model with SLA 3D printed supporter. The dimensional parameters are shown in 3 views in* mm.